Title Recent Advances in Organic and Organic-Inorganic Hybrid Materials for Piezoelectric Mechanical Energy Harvesting

Thangavel Vijayakanth,* David J. Liptrot,* Ehud Gazit,* Ramamoorthy Boomishankar,* and Chris R. Bowen*

Dr. Thangavel Vijayakanth*
Department of Chemistry and Centre for Energy Science, Indian Institute of Science Education and Research, Pune, Dr. Homi Bhabha Road, Pune – 411008, India.
The Shmunis School of Biomedicine and Cancer Research, George S. Wise Faculty of Life Sciences, Tel Aviv University, 6997801 Tel Aviv, Israel.
E-mail: vijayakantht@mail.tau.ac.il
Dr. David J. Liptrot*
Department of Chemistry, University of Bath
Claverton Down, Bath BA2 7AY (UK)
E-mail: d.j.liptrot@bath.ac.uk
Prof. Ehud Gazit*
The Shmunis School of Biomedicine and Cancer Research, George S. Wise Faculty of Life Sciences, Tel Aviv University, 6997801 Tel Aviv, Israel.
Department of Materials Science and Engineering, Tel Aviv University, 6997801 Tel Aviv, Israel.
E-mail: ehudg@post.tau.ac.il
Prof. Ramamoorthy Boomishankar*
Department of Chemistry and Centre for Energy Science, Indian Institute of Science Education and Research, Pune, Dr. Homi Bhabha Road, Pune – 411008, India.
E-mail: boomi@iiserpune.ac.in
Prof. Chris R. Bowen*
Department of Mechanical Engineering, University of Bath
Claverton Down, Bath BA2 7AY (UK)
E-mail: c.r.bowen@bath.ac.uk

Keywords: piezoelectricity, ferroelectricity, energy harvesting, organic composites, organic-inorganic hybrids, flexible electronics

Abstract

This article provides a comprehensive overview of piezo- and ferro-electric materials based on organic molecules and organic-inorganic hybrids for mechanical energy harvesting. Molecular (organic and organic-inorganic hybrid) piezo- and ferro-electric materials exhibit significant advantages over traditional materials due to their simple solution-phase synthesis, light-weight nature, thermal stability, mechanical flexibility, high Curie temperature and attractive piezo- and ferro-electric properties. However, the design and understanding of piezo- and ferro-

electricity in organic and organic-inorganic hybrid materials for piezoelectric energy harvesting applications is less well developed. We describe the fundamental characterization of piezo- and ferro-electricity for a range of recently reported organic and organic-inorganic hybrid materials. First, we outline the limits of traditional piezoelectric harvesting materials, followed by an overview of the piezo- and ferro-electric properties of organic and organic-inorganic hybrid materials, and their composites, for mechanical energy harvesting. We provide an extensive description of peptide-based and other biomolecular piezo- and ferro-electric materials as a bio-friendly alternative to current materials. Finally, we highlight current limitations and future perspectives in this emerging area of research. This perspective aims to guide chemists, materials scientists, and engineers in the design of practically useful organic and organic-inorganic hybrid piezo- and ferro-electric materials and composites for mechanical energy harvesting.

Contents:

1. Introduction

1.1 Common features of piezo-, pyro-, and ferro-electric materials

Dielectric materials, such as glass, mica, wood, rubber, ebonite, paper, air, and vacuum are electrically insulating or non-conducting materials; typically, the energy gap is greater than 3 eV. Nevertheless, dielectric materials become polarized when subjected to an external electric field.[1-3] The electric polarization occurs when the positive and negative charges in the material are displaced towards and opposite directions of an external electric field. In general, dielectric materials are classified into two main categories, namely *linear* and *non-linear* dielectrics. The

primary applications of non-linear dielectric materials are capacitors, transformers, resonators, transducers, semiconductor devices, noise filters, radio-frequency transmitters, power cables, gate dielectrics, and liquid crystal displays. [4-7] Piezoelectricity is the ability of a dielectric material to convert mechanical energy into electrical energy and vice versa. Interestingly, the piezoelectric properties of the material are highly diverse, and the electromechanical interaction characteristics are characterised by the *direct* and *converse* piezoelectric effect. The piezoelectric coefficient or charge constant (d_{ij}) is a measure of the generation of internal electric field per unit of applied mechanical stress (direct piezoelectric effect), or the mechanical strain per unit electric field (converse piezoelectric effect).[1,3] Manifestations of piezoelectric materials can be characterized by key piezoelectric (longitudinal and transverse), where magnitude of the induced piezoelectric coefficients are represented by the units pC N^{-1} (direct piezoelectric effect) and pm N^{-1} (converse piezoelectric effect), respectively. The direct piezoelectric effect was discovered in 1880 by Pierre and Jacques on a single crystal of Rochelle salt. [8,9] Moreover, a lack of mirror-plane or inversion symmetry is required to exhibit piezoelectric properties in crystalline materials. Among the 32 crystallographic classes, which include 230 space groups, 21 of them are non-centrosymmetric or piezoelectric (except 432), the remaining 11 belong to centrosymmetric or non-piezoelectric (inversion center) classes.[10] The 10 polar point groups [1 *(C_1)*, 2 *(C_2)*, m *(C_{1h})*, mm2 *(C_{2v})*, 4 *(C_4)*, 4mm *(C_{4v})*, 3 *(C_3)*, 3m *(C_{3v})*, 6 *(C_6)*, and 6mm *(C_{6v})*, with a unique polarization axis, whose spontaneous polarization varies with temperature, is exhibit *pyroelectricity* and generate charge in response to a temperature change.[11-13] If the intrinsic spontaneous polarization can be reversed or reoriented by an external electric field and produces a polarization reversal or hysteresis loop, the material exhibits *ferroelectricity*. Ferroelectric materials are a special type of dielectric material and a subgroup of both piezo- and pyro-electric materials. All ferroelectric materials display piezo- and pyro-electric behavior, but the converse is not ideally true; as outlined in Figure 1. The macroscopic polar arrangement of a ferroelectric material can be disturbed with a temperature

increase due to a phase transition. For example, in the vicinity, and below, the structural phase transition temperature (the Curie temperature, T_C), the non-linear dielectric material turns from a high symmetry disordered state (paraelectric) to a low symmetry order state (ferroelectric). These structural phase changes can alter a variety of physical characteristics such as crystal structure symmetry, thermal stability, and electrical and mechanical properties. The unique multi-dimensional properties of piezo- and ferro-electric materials have been studied and utilized in a variety of electroactive component systems; these include capacitors, sensors, micro-robotics, field-effect transistors (*FET*), micro- and nano-electromechanical systems (*MEMS* and *NEMS*), ferroelectric random access memory (*FeRAM*), photovoltaics, energy storage and conversion devices, electro-optical systems, and as vibrational energy harvesters.[14-15]

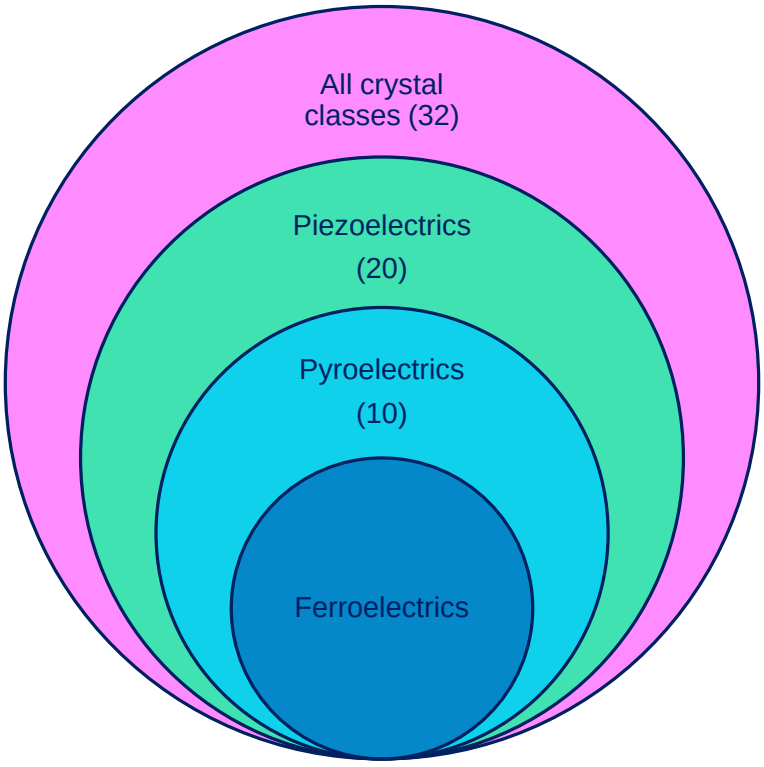

Figure 1. Relationship between dielectric, piezoelectric, pyroelectric, and ferroelectric materials.

1.2 Piezo-electric energy harvesters: the past, present and future

The need for energy harvesting technologies is increasing with the worldwide growth in population density, rapid technological progression, expanding automation and spreading

electronic networks. Currently, most of these demands are met by consuming non-renewable resources such as fossil fuels (coal, oil, petroleum, and natural gas), metal ores, and earth minerals.[16-18] In this regard, alternative sustainable and highly abundant energy sources such as solar, heat, wind, biomass, biofuel, tidal and mechanical energy have been explored to some extent.[19-27] For example, a number of diverse approaches that have been established to harvest simple and eco-friendly waste energy into usable electrical energy for optoelectronic applications.[28-32] The conversion of mechanical energy into electrical energy is of significant interest due to the simplicity of its generation from a variety of external sources such as pressure fluctuations, bending, folding, and stretching movements. This form of harvesting is generally utilized to drive low-power electronics, often in the μW to mW range, and serves as an autonomous power source for applications in wireless sensor networks.[22,33-35] In this regard, *supramolecular organic* and *organic-inorganic hybrid* piezo- and ferro-electric materials characterized by asymmetric crystallographic arrangement and intrinsic polarization have attracted significant attention.[36] These materials have also found significant commercial application in modern electronic sensors, capacitors, actuators, sonar, buzzers, transducers, thermoelectrics, photovoltaics, and piezoelectric energy harvesters.[37-40]

The first examples of piezo- and ferro-electric materials were *organic* hydrogen-bonded molecules such as Rochelle salt ($NaKC_4H_4O_6 \cdot 4H_2O$) and potassium dihydrogen phosphate (KH_2PO_4).[41,42] Subsequently, new families of non-hydrogen bonded perovskites have been discovered, based on *inorganic* ceramic oxides ($PbZrTiO_3$, $BaTiO_3$, $PbTiO_3$, $LiNbO_3$, $NaNbO_3$ and $KNbO_3$). Such inorganic ferroelectric materials have been investigated in detail due to their excellent piezo- and ferro-electric properties.[43-47] However, a number of inorganic ceramic oxide materials are derived from toxic lead-based systems, rare-earth or heavy metals. They are also brittle (low fracture toughness), possess high stiffness, high density, and require high processing temperatures for the solid-state sintering process. Therefore, the use of these materials in flexible energy harvesting and wearable electronic applications is restricted.[48,49] As

a result, it is desirable to formulate new materials that are lead and heavy metal-free, eco-friendly and can be formed at low processing temperatures to generate energy harvesters for low-power electronic applications. Among the range of commercially available polymers, polyvinylidene fluoride (PVDF) and its copolymers have attracted attention because of their high piezoelectric polarization.[50,51] However, the synthesis of the electroactive ferroelectric β-phase of PVDF remains a challenging task. For example, there is a need for external binders or a mechanical stretching process to produce the β-phase of PVDF, which increases processing complexity.[52,53] As an alternative approach, composites based on small-molecule-based organic and organic-inorganic hybrid compounds are suitable for such applications. These newly emerging ferroelectric materials are advantageous for piezoelectric sensing and energy harvesting due to their facile synthesis, low processing temperatures, high thermal stability, light-weight nature, mechanical flexibility, high piezoelectric coefficient (a measure of the charge produced per unit force), and high Curie temperature, as outlined in Figures. 2 and 3.[54,55] However, to date, only a limited number of organic and organic-inorganic hybrid piezo- and ferro-electric materials have been explored for energy harvesting applications.[40,56-60] In this review, we first provide a comprehensive overview highlighting traditional piezoelectric materials, such as zinc oxide nanowires, inorganic ferroelectric ceramic oxides and PVDF. We outline their current limitations and explain why new materials are needed. Subsequently, emphasis is given to recent developments in harvesters based on organic and organic-inorganic hybrids materials and composite structures for piezoelectric energy harvesting applications, describing recent advancements and key examples. In particular, we focus on organic and organic-inorganic hybrid energy harvesters along with their polymer matrix composites that showcase their ease of processing, an eco-friendly nature, highly stable properties and low production and energy cost for piezoelectric energy harvesting applications. While excellent review papers on piezoelectric energy harvesting and biomolecular and halide perovskites materials exist[56-60], no comprehensive review to date has summarized recent advancements of

organic and organic-inorganic hybrid energy harvester and their polymer matrix composites for piezoelectric energy harvesting applications.

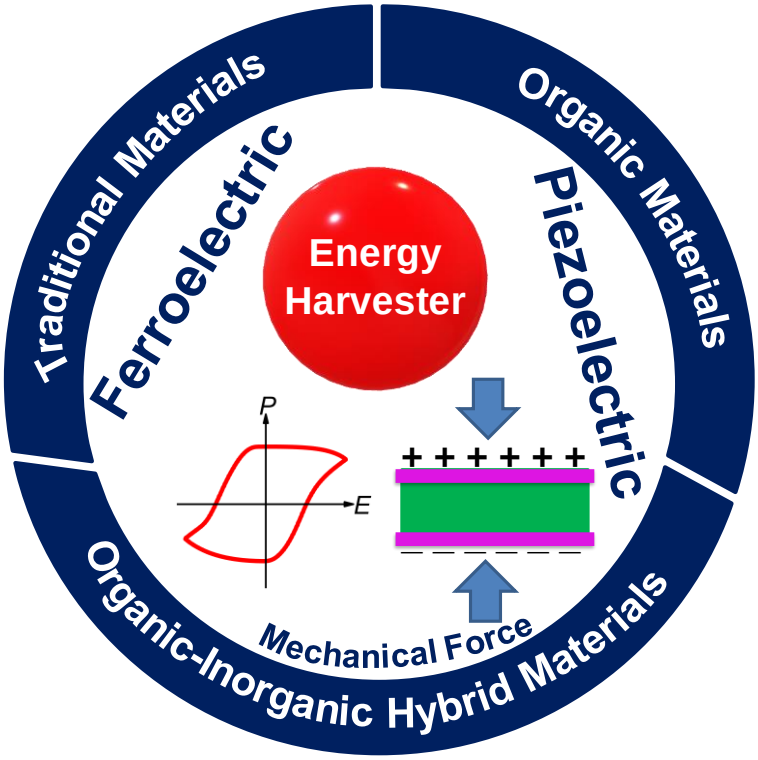

Figure 2. Schematic of piezo- and ferroelectric energy harvesters including traditional and newly emerging organic and organic-inorganic hybrid materials.

In this review, the key challenges associated with fabricating high-performance piezoelectric energy harvesters (PEHs) based on organic and organic-inorganic hybrid materials and composites are described and discussed. Finally, the review concludes with an outlook into the challenges and the future directions of these intriguing new materials. This review opens with a brief overview of traditional PEHs (Section 2), before summarising the state of the art in modern PEHs, subdivided into purely organic systems (Sections 3 and 4), and hybrid systems (Sections 5 and 6). Finally, we present with a summary and future perspectives (Section 7), and outline proposed areas for further development.

2. Traditional Piezoelectric Energy Harvesters

2.1 Piezo- and ferro-electric ceramics

Wang and coworkers in 2006 presented an exciting and pioneering development of a piezoelectric energy harvester by subjecting hexagonal zinc oxide (ZnO) nanowires to external forces.[61] The electromechanical response of vertically grown ZnO nanowires was examined using a bending mode of operation. The observed output voltage of 8 mV and low power of 0.5 pW was a result of a low level of piezoelectric polarization. In addition to the use of ZnO nanowires, several semiconducting materials have been explored for mechanical energy harvesting, such as aluminum nitride (AlN, ultra-wide gap semiconductor, band gap of ~ 6 eV, typically in the form of thin-films, or nanowires), gallium nitride (GaN), indium nitride (InN), zinc sulfide (ZnS), and cadmium sulfide (CdS).[48,62-64] Neglecting extrinsic contributions as a result of domain motion, the piezoelectric coefficient (d_{ij}) can be assumed to directly proportional to the remnant polarization of the material (e.g. $d_{33} = 2Q_{33}\varepsilon_{33}\varepsilon_0 P_r$), where ε_{33} is the dielectric constant, Q_{33} is electrostrictive coefficient, and P_r is the remnant polarization).[65,66] As a result, it is anticipated that the use of materials of similar Q_{33} with a high level of piezo- and ferro-electric polarization can improve the performance of piezoelectric energy harvesting devices. Recently, the output performance of PEH devices based on inorganic ceramic oxides ($PbZrTiO_3$, $BaTiO_3$, $PbTiO_3$, $ZnSnO_3$, $LiNbO_3$ and $NaNbO_3$) has been significantly improved from nanowatts to milliwatts due to their improved piezoelectric polarization. While seveal of these ceramic materials show substantial energy harvesting abilities, they are brittle, high density and require a high processing temperature. Most importantly, the presence of hazardous bio-incompatible toxic metal ions limits their use in wearable electronics and medical applications.[57,67,68] As a result, research has been accelerated in the preparation of alternative low-density materials that are free of heavy metals for such portable applications.[69,70]

2.2 Piezo- and ferro-electric polymers

In general, organic piezoelectric polymer materials are a subclass of organic metal-free piezoelectric materials. The commonly studied organic traditional piezoelectric polymers include poly(vinylidene fluoride) (PVDF), its copolymer poly(vinylidene fluoride-*co*-

trifluoroethylene) (PVDF-TrFE) or poly(vinylidene fluoride-co-hexafluropropylene) (P(VDF-HFP). Most of these piezoelectric polymers can be classified into two main types, *semi-crystalline* (the majority of piezoelectric polymers) and *amorphous* polymers. Semi-crystalline piezoelectric polymers exhibit a polar crystalline phase, while the amorphous polymers do not. However, semi-crystalline PVDF-based polymers exhibit multiple phases (α, β, γ, δ, and ε phases) and obtaining the most polar crystalline β-phase is challenging and there is a need for a new generation of room temperature piezoelectric materials for energy harvesting applications.[71,72] In addition, the nucleation of the polar β-phase requires mechanical deformation, long processing times, high-temperature annealing, high-voltage poling (typically above 50 MV m^{-1}) and the use of external additives. The primary difference between traditional piezoelectric polymers and organic piezoelectric materials (typically, acid-base adducts, organic salts, amino acids and peptides) is the ease in achieving a polar ferroelectric and piezoelectric phases. Organic piezoelectric materials (excluding piezopolymers) possess a number advantages, which include a facile synthesis, structural diversity, intrinsic dipole moment, dipolar orientation, improved biodegradability, high piezoelectric voltage and electrostrictive coefficients, which leads to improved electromechanical behaviour (refer the sections 3 and 4). Another structural difference between traditional piezoelectric polymers and organic piezoelectric materials is related to the molecular dipole moment. For example, in PVDF, the molecular dipole moment is created between the (CH_2–CF_2) groups. In contrast, in organic piezoelectric compounds, the polar arrangement can be generated between a variety of hydrogen bond donors (C···H, N···H, O···H) and hydrogen bond acceptors (F, Cl, Br, I, BF_4, ClO_4, IO_4, PF_6, and COO^-. Due to the diverse structural characteristics, organic piezo- and ferro-electric materials are of considerable importance for future sensing and harvesting applications (refer the sections 3 and 4). For additional details regarding conventional piezoelectric energy harvesters, which include ZnO, AlN, InN, ZnS, CdS, inorganic ceramic oxides, PVDF and its copolymers, the reader is referred to a number of excellent overviews.[73,74]

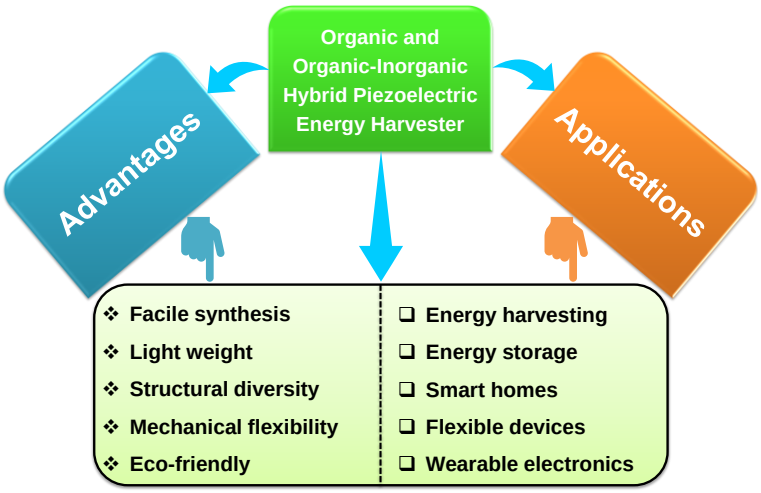

Figure 3. Advantages and applications of organic and organic-inorganic hybrid piezoelectric energy harvesters.

3. Organic Piezoelectric Energy Harvesters

3.1 Acid-base adducts

The multi-functional behavior of organic piezo- and ferro-electric materials impacts on a wide variety of fields, including chemistry, physics, biology and materials science.[73-75] Organic piezoelectric materials are attractive due to their light-weight nature, mechanical flexibility, low-cost, eco-friendly nature and low fabrication temperature, which are essential for flexible-, printable- and sensor-electronic devices. This section highlights recent developments in small molecule-based organic piezo- and ferro-electric materials and their use in mechanical energy harvesting applications. Recently, Bowen and coworkers demonstrated the piezoelectric energy harvesting application of a trimethylamine borane (TMAB) material formed via mechanical pressing.[76] They judiciously manipulated the non-polar character of a neopentane molecule by replacing a single C-C bond with a charge-separated N-B bond (Figure 4a). Single crystal X-ray diffraction analysis of TMAB showed a high-symmetry rhombohedral polar *R*3*m* space group, which is suitable for displaying ferroelectric properties. Figure 4a-c shows the design principle, molecular structure and packing diagram of the TMAB molecule along the crystallographic 'c' axis. The head-to-tail interactions between the Me_3N and BH_3 groups link the adjacent molecules along their polar axis with a B-N bond distance of 1.6174(58)Å. This Lewis acid-base type adduct shows piezoelectric and pyroelectric sensing/harvesting potential

via mechanical pressing and subjecting to temperature oscillations. The flexible TMAB device, after poling, exhibited an open-circuit voltage and short-circuit current of ~ 10.85 V and ~ 0.42 μA, respectively, when subjected to a mechanical pressure by a human finger (Figure 4d and e). Further work is required to understand the ferroelectric properties of the material. Nevertheless, this is the first instance where a simple amine-borane-based flexible substrate displays multi-functional energy harvesting properties. In the future, this type of unique design strategy can allow the fabrication of numerous devices enabled based on organic piezoelectric materials for multi-functional flexible electronics applications.

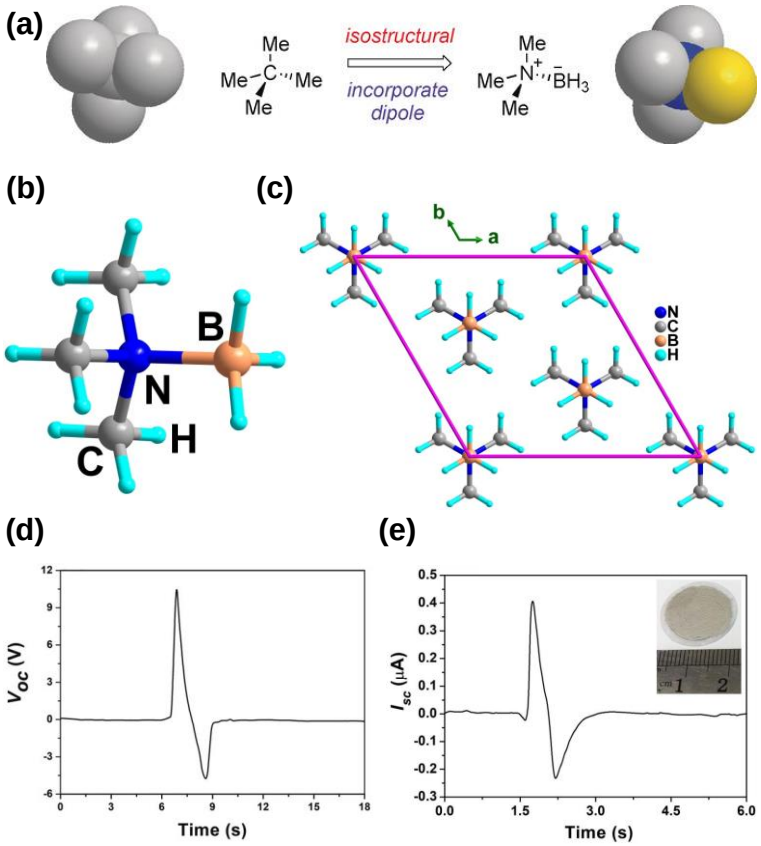

Figure 4. (a) Design principle of TMAB. (b) and (c) Schematic of molecular structure and packing diagram of TMAB along the crystallographic 'c' axis. Piezoelectric energy harvesting performance (d) Output voltage and (e) Output current of TMAB device. Reproduced with permission from ref. 76. Copyright © 2020 WILEY-VCH Verlag GmbH & Co. KGaA, Weinheim.

3.2 Amino-acids and peptides

While many materials can be utilized for piezoelectric energy harvesting applications, a number lack biocompatibility that limits their utility in wearable electronics, including ZnO, AlN, InN, ZnS, CdS and ceramic metal oxides. As a result, bioinspired organic piezoelectric materials have emerged as promising mechanically responsive candidates for wearable electronic applications. Naturally occuring piezo- and ferro-electric materials exhibit a range of potential advantages such as biocompatibility, biosafety, biodegradability, functional molecular recognition and robust mechanical properties.[56,77,78]

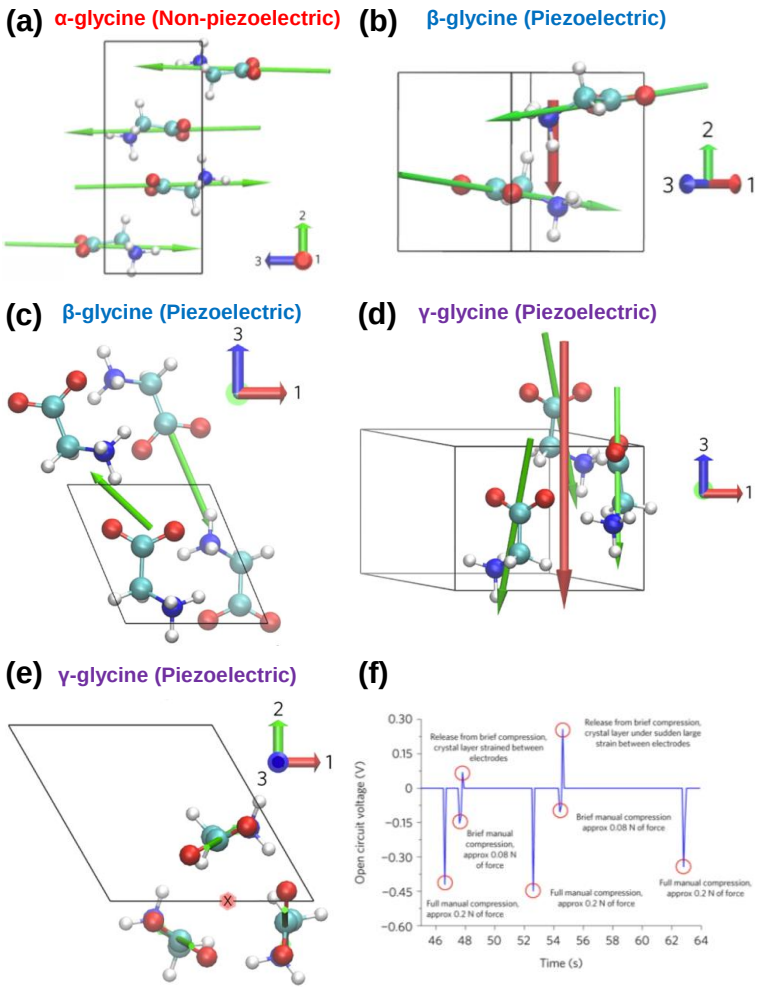

Figure 5. (a) Calculated molecular dipoles (green arrows) of α-glycine indicate the centrosymmetric structure resulting in non-piezoelectric properties. (b) Sum of molecular dipoles orientation (red arrow) of β-glycine along the 2-axis contributes to the longitudinal 22 piezoelectric coefficients. (c) View of molecular dipoles contributing to the experimentally achieved high shear piezoelectricity in β-glycine. (d) Sum of the molecular dipoles of γ-glycine (red arrow) to spontaneous polarization along the 3-axis relates to the longitudinal 33 piezoelectric

coefficients. (e) A 'top-down' view of the γ-glycine unit-cell diagram along the [001] crystallographic direction. (f) Open-circuit voltage response of a layer of γ-glycine seed crystals based piezoelectric energy harvesting device. Reproduced with permission from ref. 83. Copyright © 2018 Springer Nature.

A large number of environmentally friendly bioorganic materials have shown piezoelectric properties and can potentially be utilized for electromechanical energy harvesting applications; these include materials such as bone, wood, silk, cellulose, chitin, elastin, clamshell, amino acids, peptides, chitosan, alginate, fibrillar collagen, and viruses.[79,80] Among these materials, supramolecular self-assembled amino acids and peptides are of interest since they exhibit high piezoelectric polarization due to their permanent dipole moment. Interestingly, all amino acids, apart from glycine (specifically the α-form), exhibit polar crystal structures and have potential for use as a piezoelectric energy harvester. In general, glycine exhibits three different polymorphic phases (α, β, and γ) under ambient conditions. While the α-phase of glycine is centrosymmetric, its other two forms show non-centrosymmetric crystal structures.[81,82]

Thompson and coworkers studied the piezoelectric behavior of the β- and γ- phases of glycine through both computational and experimental methods (Figure 5a-f).[83] Interestingly, the β-form showed the highest piezoelectric shear coefficient with a $d_{16} \sim 200$ pm V^{-1}, which is comparable in magnitude to inorganic ceramic oxides and larger than many organic bio-piezoelectric materials. However, the β-phase of glycine is unstable at ambient conditions and can spontaneously change into the α- or γ-phase. A glycine PEH device was fabricated by placing γ-glycine seed crystals between two copper electrodes with an active area of 324 mm^2, which produced a maximum open-circuit voltage of 0.45 V upon applying a manual load of ~ 0.17 N (Figure 5f).

In 2019, Gazit and coworkers demonstrated the presence of ordered supramolecular self-assembled interactions in several aromatic amino acids such as L-phenylalanine (L-Phe), L-tyrosine (L-Tyr) and 3,4-dihydroxyphenylalanine (L-DOPA) (Figure 6).[84] A single-crystal X-ray diffraction analysis of L-Tyr indicated that the material has a non-centrosymmetric structure,

with attractive arrays of tightly packed hydrogen-bonded assemblies. This molecular recognition of L-Tyr crystals formed via the formation of distinct face-to-face hydrogen bond dimers results in a number of advantages which include unusual water solubility, high thermal stability (~ 581 K), robust mechanical properties, and stable power generation. Furthermore, a PEH device was fabricated by embedding the L-Tyr crystals onto a polydimethylsiloxane (PDMS) protective layer sandwiched between two Ag-coated electrodes, which were connected to a low noise voltage amplifier (Figure 6b). By applying a compressive force of 31 N, an open-circuit voltage of 0.5 V and short-circuit current of 35 nA were obtained for this device (Figure 6c).

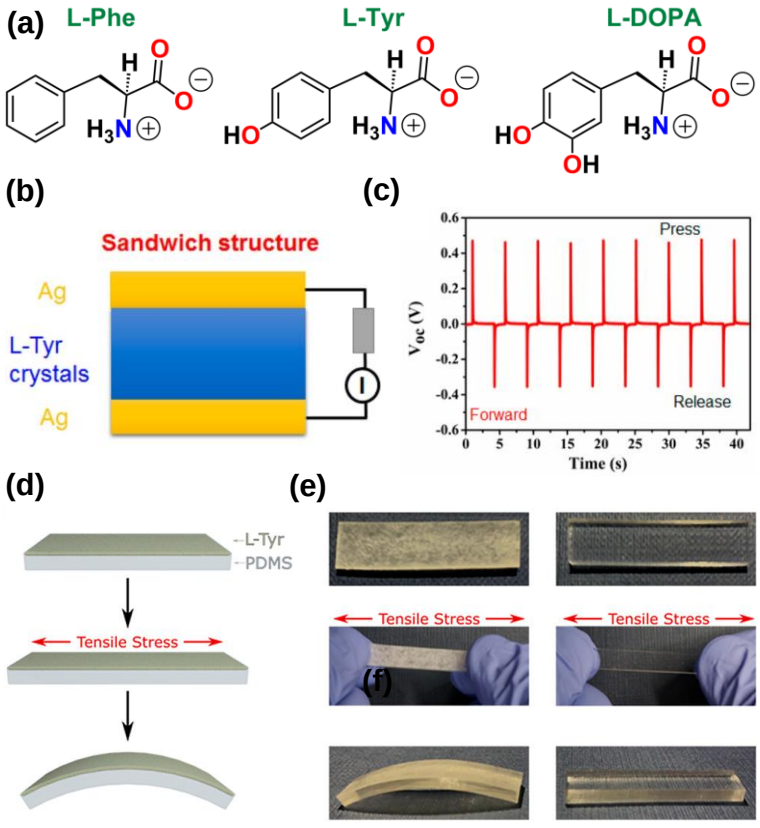

Figure 6. (a) Molecular structure of L-Phe, L-Tyr and L-DOPA. (b) Schematic of an L-Tyr crystal-based nanogenerator and energy conversion process by pressing and releasing force movements. (c) Open-circuit voltage of the L-Tyr-based nanogenerator device. (d) Representation of the mechano-responsive bending composite composed of L-Tyr and PDMS. (e) Bending response of the composite L-Tyr-PDMS (left) and pure PDMS (right). Reproduced with permission from ref. 84. Copyright © 2019 American Chemical Society.

State-of-the-art or stimuli-responsive materials, including those sensitive to temperature, pH, solvent, light, mechanical force, electric fields and magnetic fields have gained significant interest due to their potential applications in stretchable and wearable bio-integrated devices, tissue engineering, drug delivery and soft robotics.[85] In this regard, the L-Tyr-based composite material on a PDMS polymer also exihibited mechano-responsiveness, namely a response to an applied mechanical force. Composite films were obtained by coating a rigid, thin film of L-Tyr crystals on the surface of a PDMS polymer (Figure 6d). Surprisingly, the composite film exhibited an improved mechano-responsive bending behavior when subjected to a tensile-stress test compared to a pure PDMS film under the same mechanical conditions (Figure 6e). The difference in mechano-responsive behaviour can be associated with the contrast in mechanical properties of L-Tyr crystals on the PDMS substrate, compared to the neat (pure) PDMS film. These findings should stimulate the use of amino acid-based piezoelectric materials for wearable bio-integrated and stretchable electronic device applications.

In 2020, the same research group demonstrated the molecular stacking mode interactions between rigid aromatic 4,4'-bipyridine (4,4'-Bpy) and a non-aromatic amino acid derivative of N-acetyl-L-alanine (AcA), see Figure 7e.[86] Transitions between the three known types of molecular stacking modes are known, namely, H-aggregation (face-to-face stacking), J-aggregation (staggered stacking) and X-aggregation (crossed stacking), were observed in the hybrid system (Figure 7b and c). Due to the difficulties in studying each stacking mode in single molecules, *hybrid system*s were selected to study their physico-chemical properties. The stacking modes of these hybrid systems improve a number of structural aspects such as enhanced chirality, red-shift emission, thermal resistance and mechanical properties. In addition, the non-centrosymmetric nature of all three crystals leads to an intrinsic polarization potential for piezo- and ferro-electric properties. The piezoelectric properties of these salts were analyzed by density functional theory studies. The observed piezoelectric coefficient (d_{max}) and piezoelectric voltage constant (g_{max}, a measure of electric field per unit stress) values for 4,4'-

Bpy, AcA and 4,4'-Bpy/AcA were 20.9, 9.5 and 14.9 pC N^{-1}, and 1.15, 0.48, and 0.67 V m N^{-1}, respectively. These values indicate the potential of these materials for piezoelectric energy harvesting applications. Nanogenerator devices were fabricated by placing the crystals of 4,4'-Bpy and 4,4'-Bpy/AcA crystals between two conducting Ag-coated silicon substrates, which served as the upper and lower electrodes. For an applied compressive load of 56 N, the maximum observed output voltage for both the 4,4'-Bpy and 4,4'-Bpy/AcA devices reached up to 0.65 and 0.35 V, respectively (Figure 7d and e).

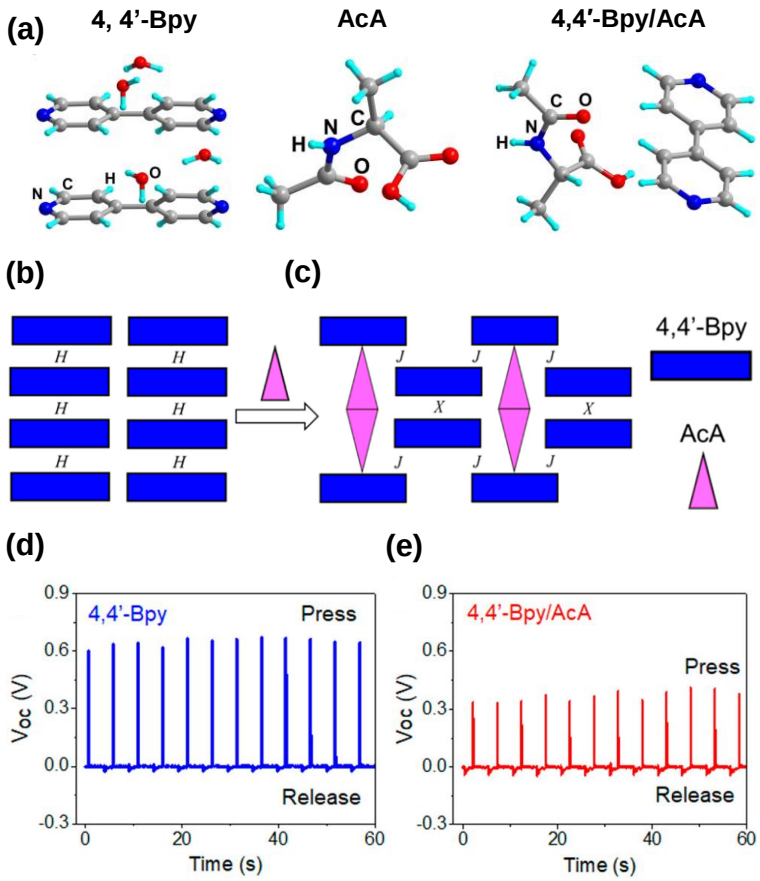

Figure 7. (a) Asymmetric unit of 4,4′-Bpy, AcA and 4-4'-BPy/AcA crystals. (b) and (c) Arrangement transition from H- to J- and X-type aggregation. (d) and (e) Output voltage of 4,4'-BPy and 4,4'-BPy/AcA nanogenerator by applying a force of 56 N. Reproduced with permission from ref. 86. Copyright © 2020 American Chemical Society.

Ultrashort peptides are one of the most promising and well-studied classes of bio-piezoelectric materials. The most prominent example is the simple aromatic dipeptide is diphenylalanine NH_2-Phe-Phe-COOH (FF), which is comprised of two phenylalanine molecules. FF forms a

number of self-assembled and hydrogen-bonded structures ranging from nanowires, nanospheres, nanocrystals, and nanotubes.[87,88] In 2010, FF nanotubes were studied for the first time for their piezoelectric properties,[87] where the FF supramolecular assembly exhibits a well-ordered and crystal structure comprising a hexamer in a non-centrosymmetric space group ($P6_1$) that can exhibit piezoelectric behavior (Figure 7a).

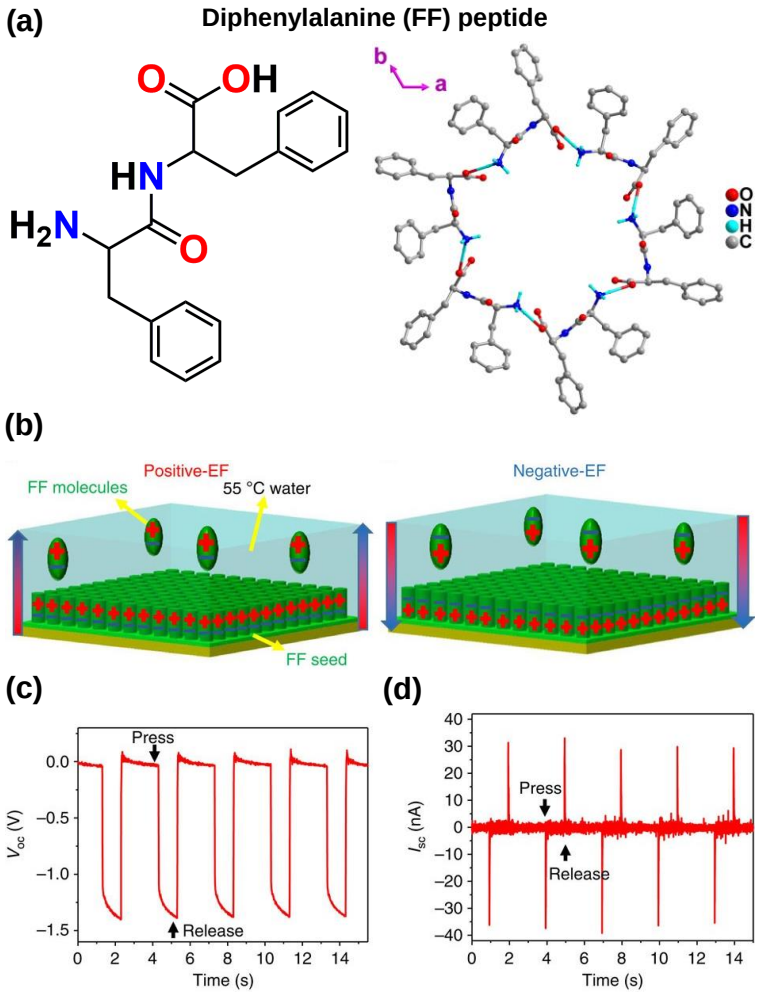

Figure 8. (a) Molecular structure of diphenylalanine (FF) peptide (left) and the view of the formation of molecular rings by six FF molecules (right). (b) Representation of the vertical growth of FF peptide microrod arrays with controlled polarization by applying an external electric field. (c) Output open-circuit voltage (V_{oc}) and (d) short-circuit current (I_{sc}) from an FF-microrod-based power generator under an applied force F = 60 N. Reproduced with permission from ref. 89. Copyright © 2016 Springer, Nature.

Furthermore, the piezoelectric energy harvesting performance of FF was examined using piezoresponse force microscopy (PFM), which demonstrated a very high shear piezoelectric coefficient of d_{15} ~ 60 pm V^{-1} for a nanotube assembly 200 nm in diameter. Subsequently,

several FF based piezoelectric energy harvesting materials have been developed that displayed strong piezoelectric properties compared to conventional piezoelectric materials.[56,86-88] However, the formation of uniformly orientated nanotubes over a large area of a substrate for large scale device manufacture is still challenging.

In 2016, Yang and coworkers developed a method to align an array of controlled FF microrods and achieved polarization by applying an external electric field during the peptide self-assembly process (Figure 8b).[89] Firstly, an amorphous and transparent FF film was prepared over an Au-coated silicon substrate by dissolving FF in 1,1,1,3,3,3-hexafluoro-2-propanol (HFP). Then, the FF film was deliberately crystallized into vertical microrod domains by subjecting the materials to high-speed humid air for 60 s. The polarization directions in the FF nanostructures were controlled by varying the direction of the applied electric field. Using this process, a high piezoelectric coefficient of $d_{33} \sim 17.9$ pm V^{-1} was obtained for the self-assembled FF microrods. Furthermore, PEH device structures were fabricated by sandwiching an array of FF microrods between the upper and lower electrodes that were connected to an external load force instrument. The piezoelectric FF microrod device produced a maximum open-circuit voltage of 1.4 V and the short-circuit current of 39.2 nA, with an applied compressive force of 60 N (Figure 8c and d).

In 2018, Lee and coworkers synthesized horizontally aligned and unidirectionally polarized FF nanotubes via a meniscus-driven self-assembly process (Figure 9).[90] The self-assembled polar FF nanostructures were produced on a large scale by pulling the substrate vertically from the FF dissolved solution, see Figure 9a. As a result, the FF nanotubes exhibited a unidirectional polarization potential for piezoelectric energy harvesting applications. A PEH was fabricated using horizontally aligned FF nanotubes on an Au/Cr coated flexible polyethylene naphthalate (PEN) substrate (Figure 9b). The resulting piezoelectric device produced an output voltage, output current and power of 2.8 V, 37.4 nA, and 8.2 nW, respectively (Figure 9c). The potential

of the FF nanotube device was demonstrated by powering multiple liquid-crystal display (LCD) panels, which display “FF PEH” by simply finger-pressing the device (Figure 9d).

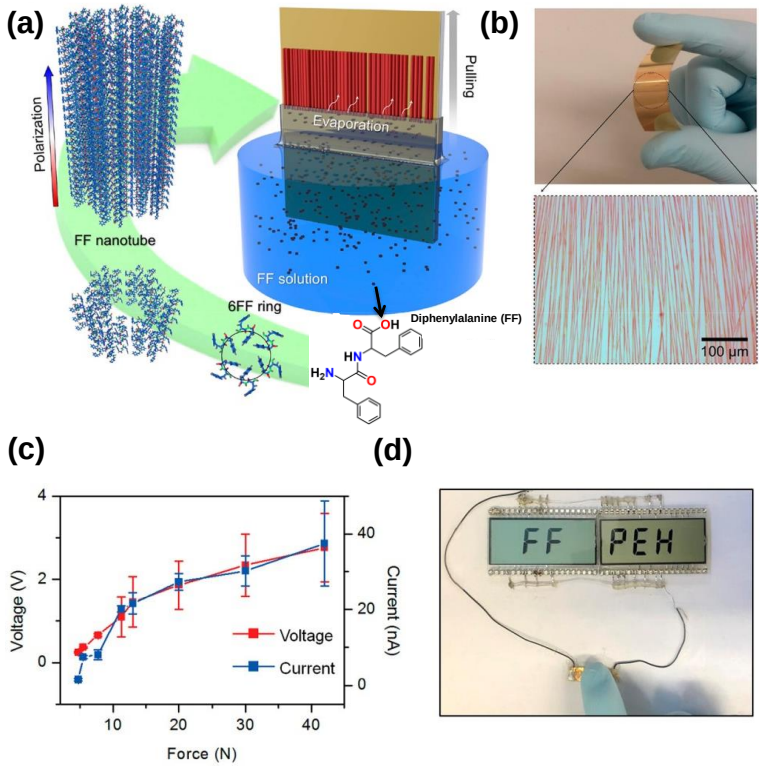

Figure 9. (a) Diagram of the synthesis of large-scale peptide nanotube arrays with unidirectional piezoelectric polarization through meniscus-driven self-assembly. (b) Photograph and optical microscopy image of the large-scale aligned peptide nanotubes on a flexible substrate. (c) Output voltage and output current of FF-nanotube-based PEH as a function of applied force. (d) View of the liquid crystal display (LCD) driven by finger pressing the PEH with a finger. Reproduced with permission from ref. 90. Copyright © 2018 American Chemical Society.

Gazit and coworkers developed a cyclo glycine-tryptophan (cyclo-GW) based dipeptide which forms a thermally stable (~ 643 K) and mechanically robust structure (elastic modulus up to ~ 24.0 GPa) due to its supramolecular β-sheet hydrogen-bonded and herringbone edge-to-face aromatic interactions (Figure 10).[91] Single crystals of the cyclo-GW dipeptide were synthesized by dissolving cyclo-GW powder in a 10% (v/v) methanol/water solvent, heating to 80 °C, whereupon needle-like crystals slowly appeared. Gradual cooling to room temperature yielded larger crystals after 30 days. Single crystal X-ray diffraction analysis of cyclo-GW revealed β-sheet hydrogen-bonding patterns along the 010 direction, with a donor (N-H)–acceptor (O-H) distance of hydrogen bonds N-H···O-H of 2.83 Å (Figure 10a). These hydrogen bonding

networks were further stabilized by interstitial herringbone-type packing as the indole units (circled by the green ellipses) formed close C···N contacts of ~ 3.4 Å.

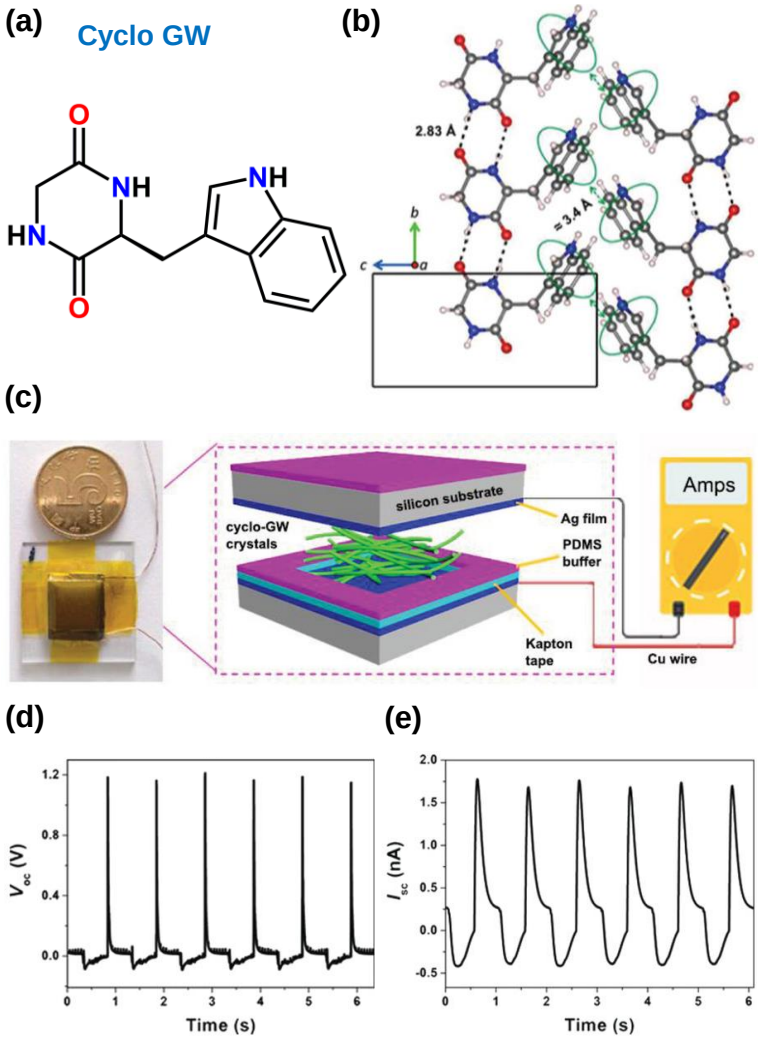

Figure 10. (a) Molecular structure of cyclo-GW. (b) Crystal packing diagram of cyclo-GW in the b-c planes. Dotted black lines indicate the hydrogen bonds and green ellipses designate the indole rings forming the herringbone-type aromatic interactions. Black rectangle marks the primitive unit cell. White, gray, blue and red spheres represent hydrogen, carbon, nitrogen, and oxygen atoms, respectively. (c) Schematic of the power generator based on cyclo-GW crystals. Inset on the left shows a photograph of the power generator. (d) and (e) Open circuit voltage and short-circuit current of cyclo-GW device. Reproduced with permission from ref. 91. Copyright © 2019 WILEY-VCH Verlag GmbH & Co. KGaA, Weinheim.

The noncentrosymmetric crystal structure (monoclinic $P2_1$) of cyclo-GW signifies its potential for piezoelectric properties. Thus, the peptide crystals were used to design a PEH by sandwiching cyclo-GW crystals between two Ag-coated silicon substrates. The whole PEH device was tightly packed with Kapton tape to protect and secure the electrical contacts and

minimise air gaps (Figure 10c). The cyclo-GW device produced an open-circuit voltage and short-circuit current of 1.2 V and 1.75 nA, respectively, under a periodic compressive force of 65 N (Figure 10d and e).

Recently, Gazit and coworkers reported on a biocompatible PEH based on tryptophan-based aromatic dipeptides (Figure 11).[92]

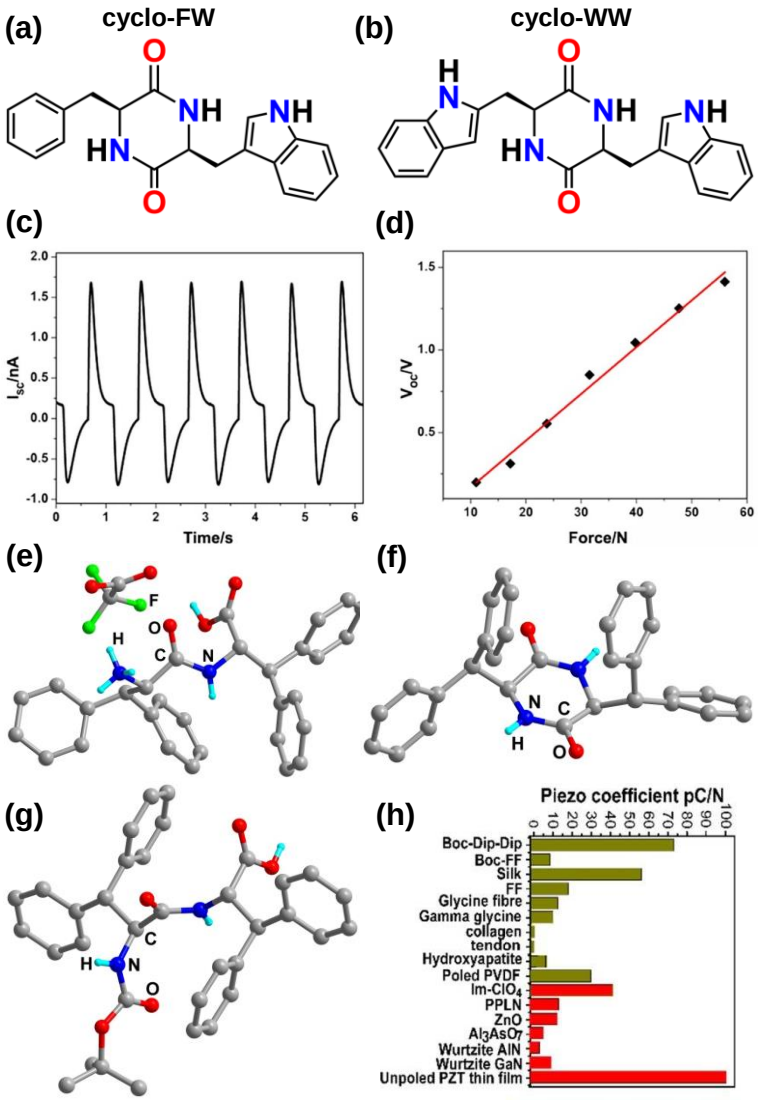

Figure 11. Chemical structures of (a) cyclo-FW and (b) cyclo-WW dipeptides. (c) Open circuit voltage of the cyclo-FW device. (d) Linear dependence of the V_{oc} on the applied mechanical forces. Asymmetric unit structure of (e) Dip-Dip, (f) cyclo-Dip-Dip and (g) Boc-Dip-Dip ultra-aromatic dipeptides. (h) Comparison of the piezoelectric coefficient of Boc-Dip-Dip and diverse organic and inorganic materials. Reproduced with permission from ref. 92. Copyright © 2019 Elsevier Ltd and ref. 93. Copyright © 2020 American Chemical Society.

These supramolecular self-assembled peptides display extensive and directional hydrogen-bonded structures, which show outstanding rigidity and strong thermal stability. Remarkably, they also exhibit unique semiconducting, mechanical and piezoelectric properties. The cyclo-phenylalanine–tryptophan (cyclo-FW) and cyclo-tryptophan–tryptophan (cyclo-WW) crystals were synthesized with a backbone of diketopiperazine rings (Figure 11a and b). This structure leads to fascinating hydrogen-bonded interactions between donor-acceptor moieties. Notably, cyclo-FW was shown to crystallize in the acentric orthorhombic $P2_12_12_1$ space group. A nanogenerator device was fabricated by placing cyclo-FW crystals between Ag-coated silicon substrates, which acted as an upper and lower electrode to exploit its piezoelectric properties for energy harvesting. Upon applying an external force of 56 N to the cyclo-FW device, the generated open-circuit voltage and short-circuit current reached a maximum values of 1.4 V and 1.75 nA, respectively (Figure 11c and d). The cyclo-FW device also exhibited a force-dependent output, with a linear trend with respect to output voltage and applied force (Figure 11d).

In addition to these reports, in 2020, Gazit and coworkers developed a strategy to manufacture short and phenyl-rich aromatic dipeptides based on the β,β-diphenyl-Ala-OH (Dip) unit, namely Dip-Dip, cyclo-Dip-Dip, and *tert*-butyloxycarbonyl (Boc)-Dip-Dip moieties (Figure 11e-g).[93] These aromatic rich dipeptides crystallized in an acentric space group and displayed strong mechanical and piezoelectric properties. Interestingly, Boc-Dip-Dip shows many advantageous features such as a small number of molecules per unit-cell, crystal dipole orientation, and high piezoelectric polarization compared to well-studied aromatic-rich dipeptides. To exploit its high piezoelectric coefficients (d_{33} ~ 73.1 pC N^{-1}), the authors fabricated a mechanical energy harvesting device that produced a maximum output voltage of 1 V and a current of 60 nA under an applied load of 40 N (Figure 11h). In addition, its piezoelectric voltage coefficient, which is a measure of the electric field generated per unit stress ($g_{33} = d_{33}/\varepsilon_{33}$), was computed to be 2−3

Vm N^{-1}, higher than many well-known perovskite inorganic ceramic oxides, PVDF and small-molecules based organic and organic-inorganic hybrid compounds.[54]

More recently, the same group demonstrated the molecular engineering of piezoelectricity in collagen-mimicking peptide assemblies.[94] The peptide-based piezoelectric generator was developed using a simple FF-derived peptides N-terminated by proline (Pro) or hydroxyproline (Hyp) moieties, namely Pro-Phe-Phe (P-F-F) and Hyp-Phe-Phe (Hyp-F-F). Figure 12 shows the molecular structure, calculated theoretical piezoelectric coefficient and piezoelectric energy harvesting generator of Pro-Phe-Phe and Hyp-Phe-Phe assemblies. Both Pro-Phe-Phe and Hyp-Phe-Phe tripeptides assemblies displayed helical-like sheet structures stabilized by the hydrophobic nature of Phe residues. These self-assembled tripeptide structures exhibited excellent mechanical strength and high piezoelectric response, which was maximized in the case Hyp-Phe-Phe, due to the robust H-bonding seen for the Hyp substituent (Figure 12b and c). Thus, as expected in the case of Hyp-Phe-Phe, the addition of a hydroxyl group increased the piezoelectric response by an order of magnitude (d_{16} and d_{35} = 27 pm V^{-1}), due to the elevated number of non-zero piezoelectric constants in each tensor and an increase in crystal polarizability under stress (Figure 12c).

Furthermore, to investigate the potential of the tripeptide assemblies for piezoelectric energy harvesting, a coin-size power generator was designed and fabricated by tightly placing Pro-Phe-Phe and Hyp-Phe-Phe films between two conducting Ag electrodes that were connected to a measuring instrument via copper wires. The entire device was firmly covered with Kapton tape to provide high-temperature resistance and protect against contamination by dust, and humidity (Figure 12d). The electromechanical responses of the Pro-Phe-Phe and Hyp-Phe-Phe devices were evaluated by compressing and releasing operations. A periodic mechanical load was applied to the power generator and the output performance in terms of both output voltage and output current is shown in Figure 12e and f. For Pro-Phe-Phe, under a mechanical force (F = 55 N), the open-circuit voltage and short-circuit current values were found to be 1.4 V and 52

nA, respectively. The Hyp-Phe-Phe power generator device displayed a short-circuit current of 39.3 nA when the mechanical force was only 23 N (half mechanical pressure applied to Pro-Phe-Phe), validating the observation of higher theoretical piezoelectric polarization.

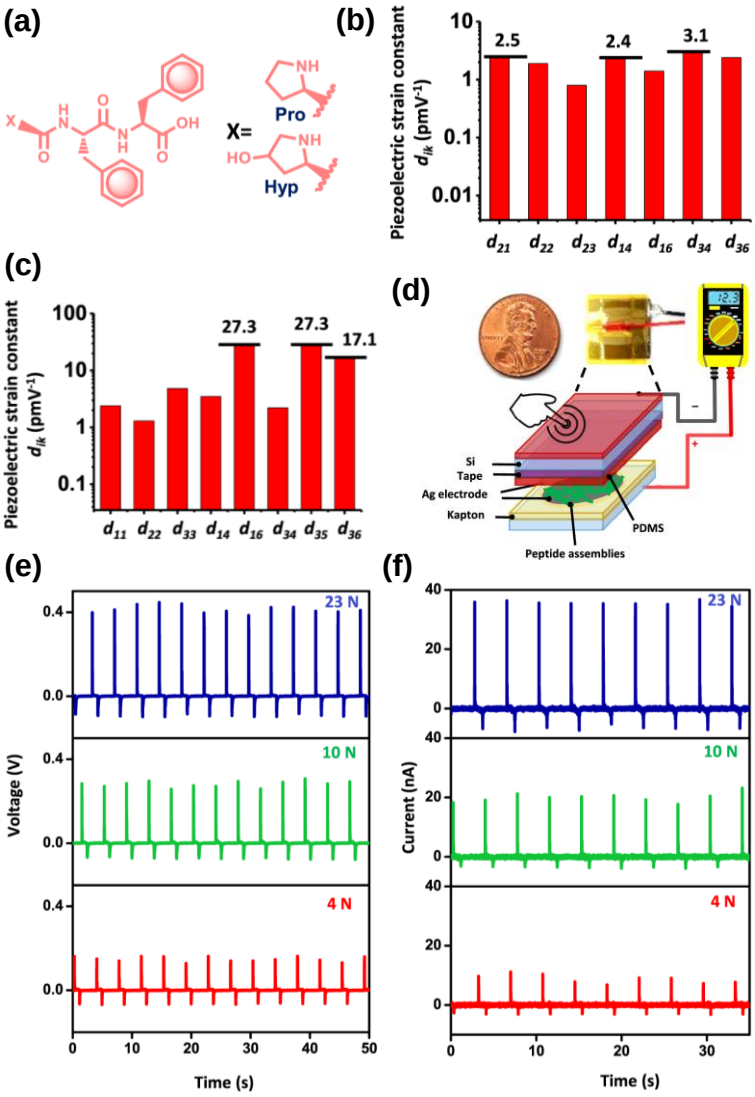

Figure 12. (a) Chemical structures of PFF and Hyp-FF tripeptides. (b) and (c) Calculated piezoelectric strain constants for PFF and Hyp-FF. Selected values are indicated above the respective columns. (d) Schematic of the coin-sized PEH measurement set-up fabricated with tripeptide assemblies as the active component. (e) and (f) Measured open-circuit voltage and short-circuit current of a HypFF-based device under a different applied mechanical forces, as indicated. Reproduced with permission from ref. 94. Copyright © 2021 Springer Nature.

Furthermore, the output voltage and short-circuit current linearly increased with the applied mechanical force (4 to 23 N), demonstrating the linear piezoelectric response of the Hyp-Phe-Phe peptide assemblies. These results demonstrate how simple hydroxylation of the side chain

can play an indispensable role in molecular engineering of piezoelectricity and peptide nanotechnology.

Table 1 provides a summary of the output voltage, current and power of organic energy harvesters in response to a mechanical input. As shown in Table 1, that a typical characteristic of piezoelectric materials and energy harvesters is their high voltage (typically 0.35 V to 10.85 V) and low current (1.75 nA to 0.42 μA).

Table 1. Summary of output performance of organic energy harvesters discussed in section **3.**

Material type	Voltage (Open circuit)	Current/current density	Power/power density	Application/Input	Area	Ref.
TMAB	10.85 V	0.42 μA	-	Finger press	-	76
γ-glycine	0.45 V	-	-	0.172 N	324 mm^2	83
L-Tyr crystal film	0.5 V	35 nA	-	31 N	0.6 x 0.6 cm^2	84
4,4'-Bpy crystal film	0.65 V	-	-	56 N	1.2 x 1.2 cm^2	86
4,4'-Bpy/AcA crystal film	0.35 V	-	-	56 N	1.2 x 1.2 cm^2	86
FF-microrod	1.4 V	39.2 nA	3.3 nW cm^{-2}	60 N	10 x 10 cm^2	89
FF-nanotube	2.8 V	37.4 nA	8.2 nW	42 N	-	90
Cyclo-GW	1.2 V	1.75 nA	-	65 N, 1 Hz	-	91
Cyclo-FW	1.4 V	1.75 nA	-	56 N	-	92
Boc-Dip-Dip	1 V	60 nA	-	40 N	-	93
PFF	1.24 V	52 nA	-	55 N	0.7 × 0.7 cm^2	94
Hyp-FF	0.45 V	39.3 nA	-	23 N	0.7 × 0.7 cm^2	94

4. Organic Piezoelectric Composite Energy Harvesters

4.1 Heteroleptic organo-amino phosphonium salts

Organic piezoelectric materials can also be used in *composite* form by embedding the piezoelectric materials in a polymer matrix. Polymer matrix composites offer numerous advantages such as low specific weight, high chemical resistance, high flexibility, high stability, ease of processing, good electrical and thermal insulation, ease of shaping and economical mass production. In addition, the inclusion of organic materials into a polymer matrix can tailor their mechanical properties, such as tensile strength, stiffness and toughness. Due to the significant advantages of polymer matrix composite material, they have found potential application in

sensors, flame retardants, optics, biotechnology and bio-medicine, aerospace engineering technologies and energy harvesting and storage systems.[35,95] Composites are also attractive if the piezoelectric material can only be fabricated in particulate or small crystal form and needs to be embedded within a matrix to create a functional device.

Recently, Boomishankar and coworkers demonstrated a piezoelectric energy harvester based on a binary phosphonium salt, diphenyl diisopropylamino phosphonium hexafluorophosphate (DPDP·PF_6), in the form of its PDMS polymer composites (Figure 13).[96] Interestingly, the DPDP·PF_6 salt crystallized in an acentric monoclinic *Cc* space group, an essential factor for the materials to exhibit piezo- and ferro-electric properties. Single-crystal X-ray diffraction analysis of DPDP·PF_6 salt showed the formation of a one-dimensional (1D)-hydrogen bonded network mediated by strong N-H···F interactions along the polar b-axis (Figure 13b). The ferroelectric polarization (*P*) versus electric field (*E*) measurements of DPDP·PF_6 exhibited a well saturated rectangular hysteresis loop, with a remnant polarization of $P_r \sim 6$ μC cm^{-2} at room temperature (Figure 13c). Furthermore, direct piezoelectric measurements on a single-crystal of this organic salt reveal a piezoelectric coefficient of $d_{33} \sim 8$ pC N^{-1} by applying a mechanical force of 0.20 N at a frequency of 110 Hz. Due to its appreciable piezo- and ferro-electric properties, the application of DPDP·PF_6 in a piezoelectric energy harvesting device was examined. Composite films of 3, 5, 7, 10 and 20 weight percentage (wt %) of DPDP·PF_6 were prepared using a PDMS polymer and tested at an operating frequency of 10 Hz and a mechanical force of 15 N. The output performance of the composite device was shown to increase with the fraction of the active material, from 3 wt % to 10 wt %. At higher weight fractions the output decreased, which can be due to the reduction in the dipole moment and long-range order interactions in the composite materials. The observed output device performance was supported by X-ray 3D-microtomography analysis, which suggests the particle agglomeration is higher for the 20 wt % DPDP·PF_6/PDMS than the 10 wt % DPDP·PF_6/PDMS composite film (Figure 13d and e). Among the range of composites

examined, the 10 wt % DPDP·PF_6/PDMS composite device yielded an output voltage of 8.5 V and a power density of 1.74 μW cm^{-3}, respectively (Figure 13f). These results show the practical energy harvesting abilities of a simple organic binary phosphonium salt.

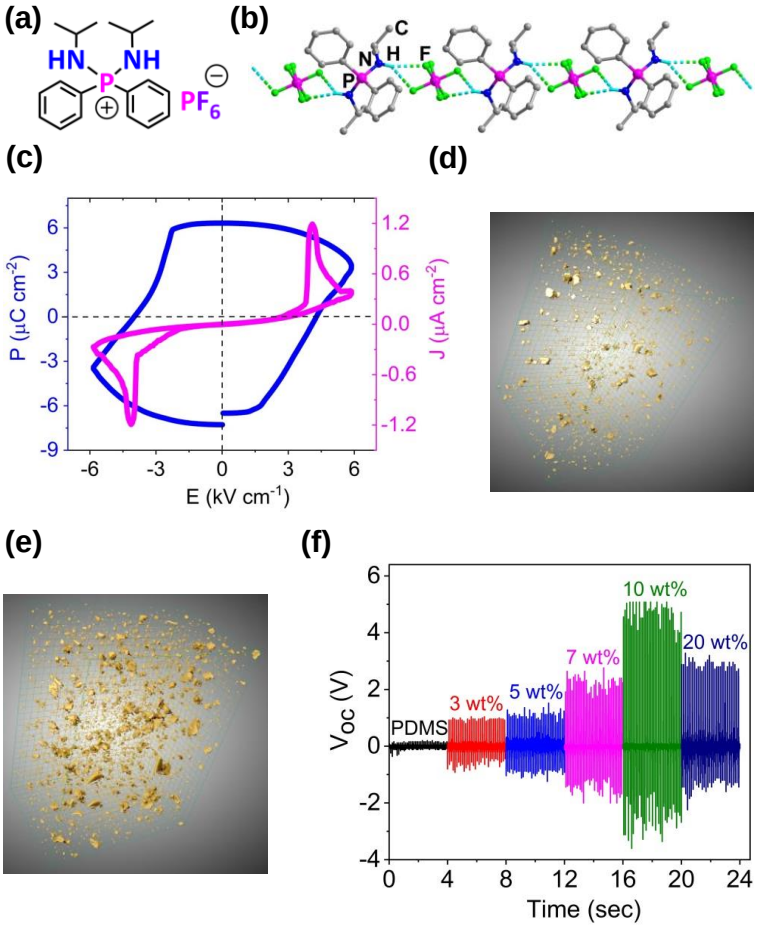

Figure 13. (a) and (b) Chemical structure and 1D-hydrogen bonded molecular assembly of DPDP·PF_6 salt mediated by N-H···F bonds. (c) Ferroelectric hysteresis loop and the corresponding leakage current density plot. (d) and (e) 3D-tomography images of 10 and 20 wt % DPDP·PF_6/PDMS film. (f) Piezoelectric energy harvesting performance of all the wt % DPDP·PF_6/PDMS composites along with a neat PDMS device. Reproduced with permission from ref. 96. Copyright © 2018 WILEY-VCH Verlag GmbH & Co. KGaA, Weinheim.

In addition, the same research group studied the remarkable influence in molecular symmetry and ferroelectric polarization using a family of amino phosphonium salts. This series included triphenyl isopropylaminophosphonium (TPAP), diphenyl diisopropylaminophosphonium (DPDP), phenyl triisopropylaminophosphonium (PTAP), and tetraisopropylaminophosphonium (TIAP) cations stabilized by tetrahedral BF_4^-, ClO_4^- and IO_4^-

anions (Figure 14).[97] These tetrahedral anions have been shown to lower the symmetry of most of these binary salts with respect to the octahedral PF_6^- anion, and are suitable for achieving a ferroelectric response. However, the salts based on the DPDP cation with all the anions (PF_6^-, BF_4^-, ClO_4^- and IO_4^-) studied in this series crystallized in the monoclinic non-centrosymmetric space group (*Cc*) signifying the vital role played by this phosphonium cation in directing the structure. Ferroelectric measurements on single-crystals of these organic salts indicated a high remnant polarization that ranged from $P_r \sim 21.12$ μC cm^{-2} to 35.36 μC cm^{-2}. The variation in the ferroelectric polarization was attributed to the formation of different donor and acceptor interactions between phosphonium cations and the tetrahedral anions.

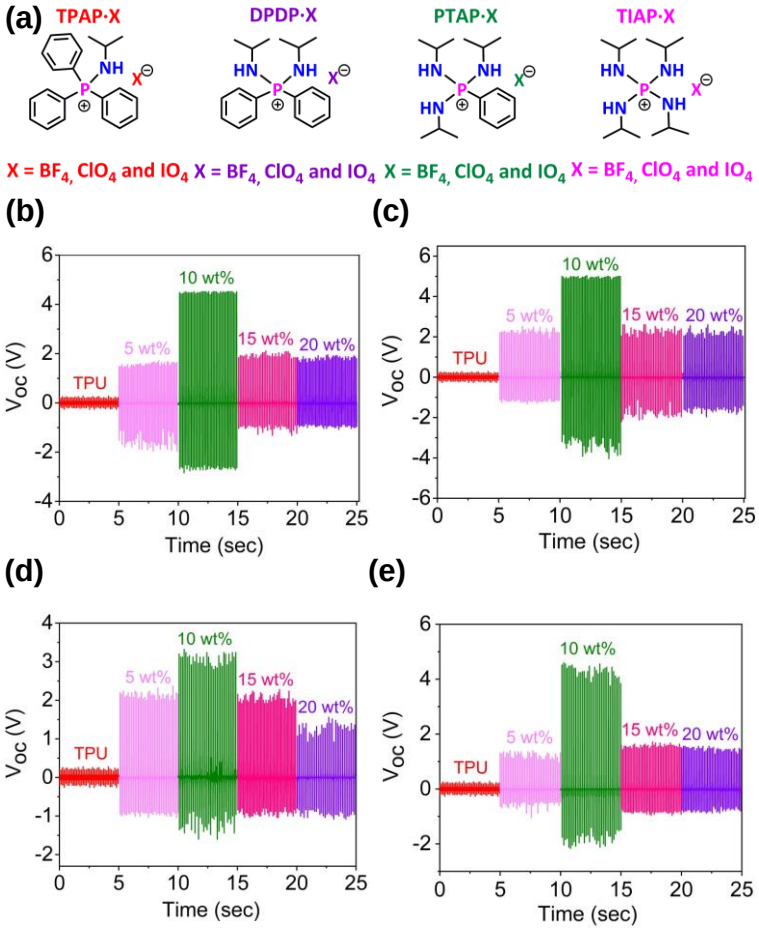

Figure 14. (a) Schematic of the chemical structures of organo-amino phosphonium salts supported by tetrahedral anions. Piezoelectric energy harvesting performance of (b) TPAP·BF_4/TPU, (c) DPDP·BF_4/TPU, (d) TIAP·BF_4/TPU and (e) DPDP·PF_6/TPU composite devices. Reproduced with permission from ref. 97. Copyright © 2019 American Chemical Society.

In addition, all-organic composite films of TPAP·BF_4, DPDP·BF_4, TIAP·BF_4, and DPDP·PF_6 salts were fabricated using a non-piezoelectric thermoplastic polyurethane (TPU) matrix. The flexible polymer composite devices showed excellent piezoelectric energy harvesting performance (Figure 14b-e). In all cases, the best device performance was observed for composites based on a 10 wt % addition, which indicates the existence of effective interactions between the organic piezoelectric salts and the polymer matrix. Peak output voltage and current density values of 8.95 V and 0.23 μA cm^{-2} were recorded for the 10 wt % of DPDP·BF_4/TPU composite device with a compressive force of 22 N and an operating frequency of 8 Hz (Figure 14c).

4.2 Organo-ammonium salts

Inspired by the earlier reports on heteroleptic organophosphonium salt-based piezoelectric energy harvesters, a two-component ammonium salt, containing a bulky $[Bn(4\text{-}BrBn)NMe_2]^+$ (Bn = benzyl and 4-Br = 4-bromo) cation and tetrahedral BF_4^- anion was recently developed by Boomishankar and co-workers for mechanical energy harvesting. The compound $[Bn(4\text{-}BrBn)NMe_2]\cdot BF_4$ (**2**) was obtained from the corresponding bromide salt $[Bn(4\text{-}BrBn)NMe_2]\cdot Br$ (**1**) (Figure 15).[98] Single-crystal X-ray diffraction analysis showed the presence of a polar orthorhombic *Pna2₁* space group with the asymmetric unit of a $[Bn(4\text{-}Br\text{-}Bn)NMe_2]^+$ cation and a BF_4^- ion (Figure 15a). Furthermore, ferroelectric hysteresis loop measurements of Compund **2** exhibited a remnant polarization of $P_r \sim 14.4$ μC cm^{-2} at room temperature at an operating frequency of 0.01 Hz. In addition, the current density (J) vs. the electric field (E) indicates two opposite peaks at the coercive switching field, which indicates two stable states of opposite polarity (Figure 15b). The high P_r value of Compound **2** can be related to its stable charge-separated structure between the $[Bn(4\text{-}BrBn)NMe_2]^+$ cation and the BF_4^- anion through the creation of non-classical C-H···F and C-H···Br interactions. Flexible TPU composites with 5, 10, 15 and 20 wt % of Compound **2** were prepared and investigated for mechanical energy harvesting applications. The 15 wt % **2**-TPU composite showed a maximum peak-to-peak

output voltage of 20 V compared to neat TPU (200 mV), thereby indicated that the observed output voltage characteristics are noticeably improved due to the embedded ferroelectric crystallites in the TPU matrix (Figure 15d). The composite films were stretchable up to 50% strain and the stress observed at 50% strain for the pure (filler-free) TPU and 5, 10, 15 and 20 wt% TPU devices was found to be 3.58, 3.88, 4.21, 3.94 and 3.65 MPa, respectively. In comparison with pure TPU, the Compound **2**-TPU composite films were found to exhibit higher stress values, indicating the effective reinforcement of the stiff ferroelectric particles in the TPU matrix that supports the stabilization of the structural and interfacial interactions between the particles of the organic ammonium salt and TPU matrix (Figure 15c).

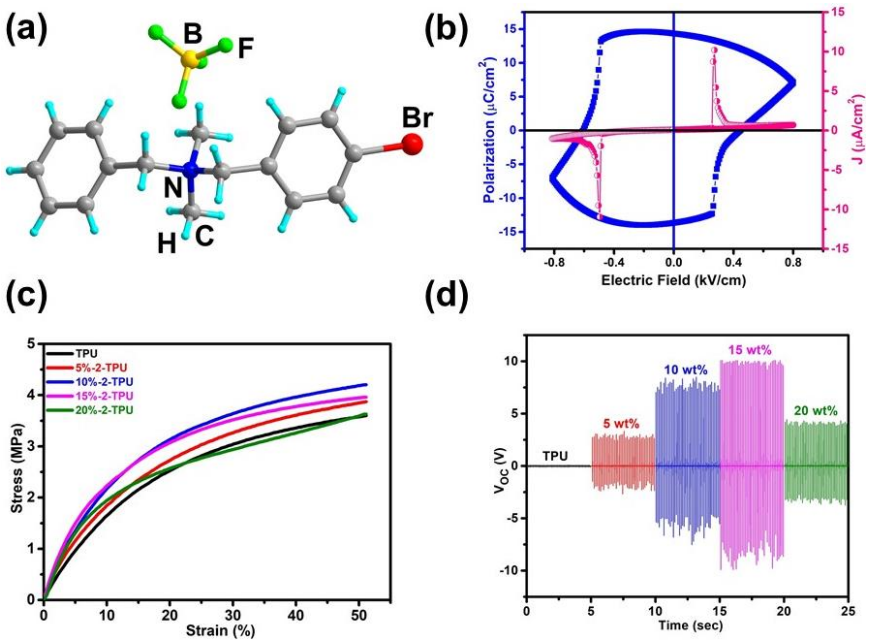

Figure 15. (a) Asymmetric unit of **2**. (b) Polarization – electric field (*P-E)* hysteresis loop and the corresponding leakage current density plots. (b) Stress vs. Strain profile of neat TPU and all the Compound **2**-TPU composite devices. (d) Output voltages of Compound **2**-TPU devices under a force of 14.15 N. Reproduced with permission from ref. 98. Copyright © 2021 WILEY-VCH Verlag GmbH & Co. KGaA, Weinheim.

4.3 Composites of 3-nitroaniline

In 2020, Belsley and coworkers demonstrated the use of an electrospinning technique to fabricate composites based on acentric 3-nitroaniline (3NA, $C_6H_6N_2O_2$) crystals embedded in a poly-ε-caprolactone (PCL) polymer (Figure 16).[99] The nanofibres of the 3NA@PCL composite

exhibited a strong optical second harmonic generation (SHG) response and piezoelectric energy harvesting properties. Figure 16a shows its chemical structure and Figure 16b shows a schematic of the formed dipoles (indicated by arrows) which are aligned parallel to the crystallographic (400) plane resulting in a preferential orientation within the PCL polymer, thereby giving rise to piezoelectric properties. By applying a periodic mechanical load of 3 N to the nanocomposite, they produced an output voltage and power density of 7 V and 122 nW cm^{-2}, respectively (Figure 16c and d). The obtained power density was sufficient to power an LCD, indicating the practical utility of nonlinear organic crystals for flexible nanogenerator devices.

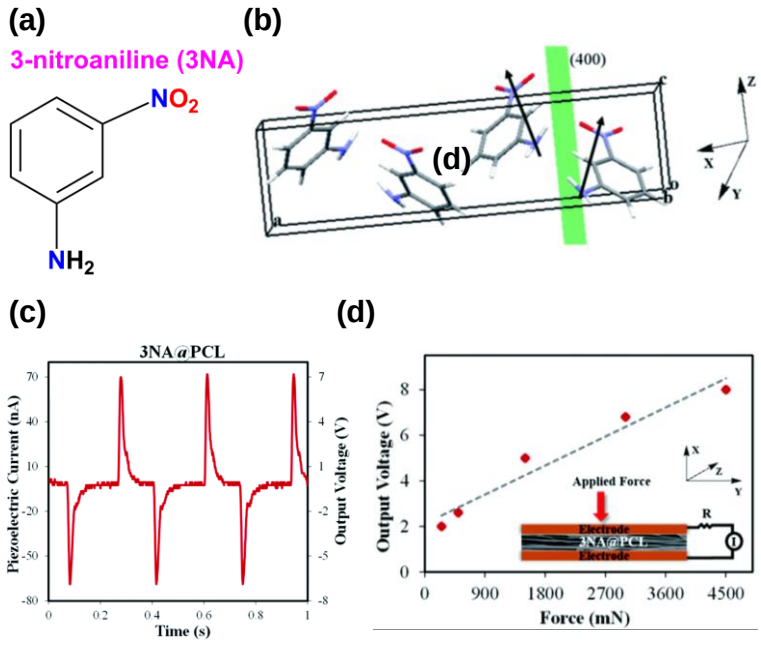

Figure 16. (a) Chemical structure of 3NA. (b) Schematic of unit-cell diagram of 3NA [the molecular dipoles are indicated by arrows parallel to (400) plane]. Piezoelectric energy harvesting performance (c) output current and output voltage of a 3NA@PCL device. (d) Force-dependent output voltage curve. Inset: schematic representation of piezoelectric setup of a 3NA@PCL electrospun nanofiber mat. Reproduced with permission from ref. 99. Copyright © 2020 The Royal Society of Chemistry.

4.4 Peptide composites

In 2019, Belsley and coworkers reported on biocompatible PEHs that were based on the Boc-FF dipeptide (Figure 17).[100] Composite films of Boc-FF were fabricated in the form of

nanotubes using commercially available polymers, in particular PCL, polymethylmethacrylate (PMMA) and poly-L-lactic acid (PLLA). These hybrid nanostructured fibres were formed on a large-scale using an electrospinning technique and composite devices were constructed using aluminium foil as an electrode with an active area of 4×10^{-4} m^2 and a thickness of 0.60 mm. Figure 17b-d shows the piezoelectric energy harvesting performance of Boc-Phe-Phe nanotubes embedded in PLLA, PCL and PMMA, respectively. The maximum open-circuit voltage (30 V), current (300 nA) and power density (2.3 μW cm^{-2}) values were achieved for the Boc-FF_PLLA (Boc-Phe-Phe_PLLA) device with an applied load of 1.5 N and a load resistance of 100 MΩ (Figure 17b). The high piezoelectric response of the Boc-Phe-Phe_PLLA device can be related to the formation of a strong dipeptide nanotube organization within the polymer fibres, which can enhance the piezoelectric coefficient of the composite device.

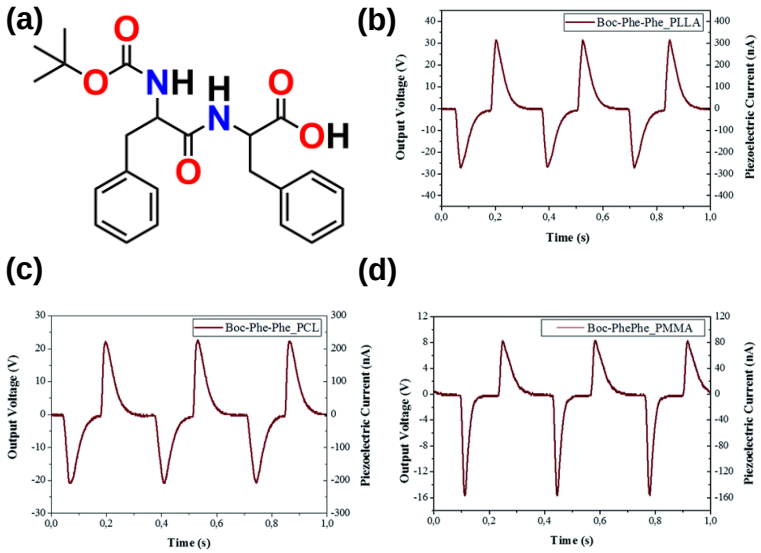

Figure 17. (a) Chemical structure of the Boc-FF dipeptide. Piezoelectric energy harvesting performance of output voltage and current of electrospun fiber arrays of Boc-FF (Boc-Phe-Phe) nanotubes embedded in (b) PLLA, (c) PCL, and (d) PMMA polymer. Reproduced with permission from ref. 100. Copyright © 2019 The Royal Society of Chemistry.

Table 2 provides a summary of the output voltage, current and power of organic composite energy harvesters in response to mechanical inputs. As shown in Table 2, the voltage ranges from 4.75 V to 30 V and the current from 70 nA to 0.89 μA. The voltage and currents values

are typically higher than the values obtained for the materials in bulk/film form presented in Table 1. This can be due to a variety of reasons. First, the ability to form a composite can enable larger and thicker energy harvesters to be produced; for example in simple compression the open circuit voltage is proportional to device thickness, since

$$V_{open} = \frac{d_{33}}{\varepsilon_{33}^{T}\varepsilon_0}.\sigma.t. \qquad \text{(equation 1)}$$

where t is thickness, ε_{33}^{T} is relative permittivity at constant stress, ε_0 is permittivity of free space and σ is stress. Second, the formation of a composite in a low-permittivity polymer matrix can also increase the voltage in response to an applied stress due to a reduction in permittivity, see Equation 1. Finally, the formation of a flexible composite can enable the energy harvester to be subjected to a higher level of strain, or larger degrees of bending, compared to the more brittle bulk materials or thin films.

Table 2. Summary of output performance of organic composite energy harvesters discussed in section **4.**

Composite type	Voltage (Open circuit)	Current/current density	Power/power density	Application/Input	Area	Ref.
DPDP·PF_6/PDMS	8.5 V	0.28 μA cm^{-2}	1.74 μW cm^{-3}	15 N, 10 Hz	1.3 x 3 cm^2	96
DPDP·PF_6/TPU	6.73 V	0.47 μA	2.83 μW cm^{-3}	22 N, 8 Hz	1.3 x 3 cm^2	97
DPDP·BF_4/TPU	8.95 V	0.89 μA	10.16 μW cm^{-3}	22 N, 8 Hz	1.3 x 3 cm^2	97
TPAP·BF_4/TPU	7.37 V	0.61 μA	4.77 μW cm^{-3}	22 N, 8 Hz	1.3 x 3 cm^2	97
TIAP·BF_4/TPU	4.75 V	0.41 μA	2.16 μW cm^{-3}	22 N, 8 Hz	1.3 x 3 cm^2	97
[Bn(4-BrBn)NMe_2]·BF_4	20 V	4 μA	21.1 μW cm^{-2}	14.15 N, 9 Hz	1750 mm^2	98
3NA@PCL	7 V	70 nA	122 nW cm^{-2}	3 N, 3 Hz	4 cm^2	99
Boc-FF_PLLA	30 V	300 nA	2.3 μW cm^{-2}	1.5 N, 3 Hz	4.0 cm^2	100
Boc-FF_PCL	22 V	-	-	1.5 N, 3 Hz	4.0 cm^2	100
Boc-FF_PMMA	8 V	-	-	1.5 N, 3 Hz	4.0 cm^2	100

5. Organic-Inorganic Hybrid Piezoelectric Energy Harvesters

5.1 Lead halide based perovskites

While organic systems are of interest, their potential to produce *hybrid* organic-inorganic systems and a variety of composites creates new opportunities to design materials for energy harvesting applications. Organic-inorganic hybrid systems are an exciting class of materials in

the field of energy and next-generation electronics.[101-104] Studies on these hybrids have recently demonstrated several advantages, including easy solution-based processing, strong optical absorption, high charge mobility, superconductivity, photoconductivity, electrical and ionic conductivity, electroluminescent behavior, tunable bandgap, high photo-conversion efficiency, and light-harvesting properties for solar device applications.[105-109] In addition to extensive utilization in photovoltaic and other optoelectronic applications, they have recently emerged as potential piezo- and ferro-electric materials for energy harvesting.[40,110,111] Moreover, the unique individual contribution of the organic and organic-inorganic counterparts in a single-phase crystalline structure can provide opportunities to tune their physical and chemical properties for specific applications. This section is therefore dedicated to an overview of organic-inorganic hybrid piezo- and ferro-electric materials for electromechanical energy harvesting applications. Organic-inorganic hybrid perovskite structures have a general formula of ABX_3, where A is an organic cation, B is a divalent metal cation and X is a halide anion. The motivation for using perovskite organic-inorganic hybrid materials is to exploit their excellent piezo- and ferro-electric properties. The majority of conventional perovskite materials are inorganic ceramic oxides (typically lead zirconate titanate, PZT, and barium titanate, $BaTiO_3$). Despite their exceptional performance, these materials require high-processing temperature, high-voltage poling, and exhibit low mechanical flexibility and contain potentially toxic elements. In contrast, hybrid perovskites and perovskites serve as an attractive alternate to alleviate several of these issues. Ordering of the organic cations results in a long-range order, which leads to their ferro- and piezo-electric properties, making them attractive for piezoelectric energy harvesting application.

In 2015, Bisquert and coworkers demonstrated light-enhanced ferro-electric polarization switching in methylammonium lead halide ($MAPbI_3$) thin films.[112] Later, Kim and coworkers reported the first organic-inorganic hybrid piezoelectric nanogenerator based on a 500 nm thick film of $MAPbI_3$ (Figure 18).[113]

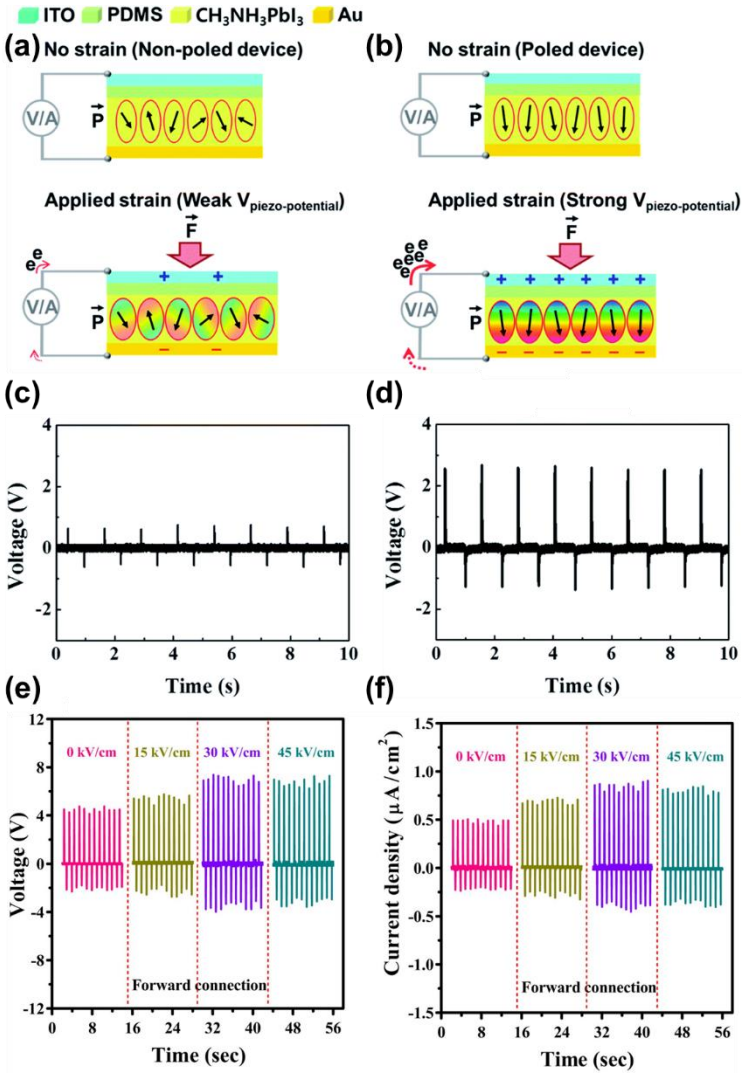

Figure 18. (a) and (b) Schematic of $MAPbI_3$ piezoelectric generators under non-poled and poled conditions. (c) and (d) Open circuit voltage of $MAPbI_3$ piezoelectric generators measured in a forward connection of under non-poled and poled devices at the electric field of 80 kV cm^{-1}. Reproduced with permission from ref. 113. Copyright © 2016 The Royal Society of Chemistry. (e) Output voltage and (f) current density of poled $MAPb_{1-x}Fe_xI_3$ (x = 0.07) PEHs measured under various applied poling fields. Reproduced with permission from ref. 114. Copyright © 2018 Elsevier Ltd.

The $MAPbI_3$ material was fabricated between two substrates which were composed of a polyethylene terephthalate (PET) and indium tin oxide (ITO) layer that was combined with a $MAPbI_3$/Au/Ti/PET layer, using PDMS as an adhesive layer. The overall structure is outlined in Figure 18a and b. The PDMS layer acts as a barrier for charge carriers, which limits current leakage from one electrode to the other through the active perovskite ferroelectric $MAPbI_3$ layer. The piezoelectric energy harvesting performance of the as-fabricated and non-poled $MAPbI_3$

device resulted in output voltage and current density values of 1 V and 50 nA cm^{-2}, respectively, after periodic application of a mechanical load of 0.5 MPa (Figure 18c). The devices were then poled under a high electric field (80 kV cm^{-1}) and subsequently generated a higher peak output voltage of 2.7 V and a current density of 140 nA cm^{-2}, respectively (Figure 18d). The increase in piezo-potential was attributed to the dominance of a higher degree of oriented dipoles in the poled $MAPbI_3$ devices compared to the non-poled samples.

Yoon and coworkers have achieved a controlled enhancement of piezoelectric output performance in $MAPbI_3$ perovskite thin films by the partial replacement of Pb^{2+} with Fe^{2+} ions.[114] This influenced the structural morphology, crystallinity, phase transition, dielectric constant, and composite device output. In addition, the incorporation of Fe^{2+} increased the dielectric constant and piezoelectric polarization of the composite materials. A maximum output voltage of 7.29 V and a current density of 0.88 μA cm^{-2} was observed for the poled $MAPb_{1-x}Fe_xI_3$ (x = 0.07) device (Figure 18e and f).

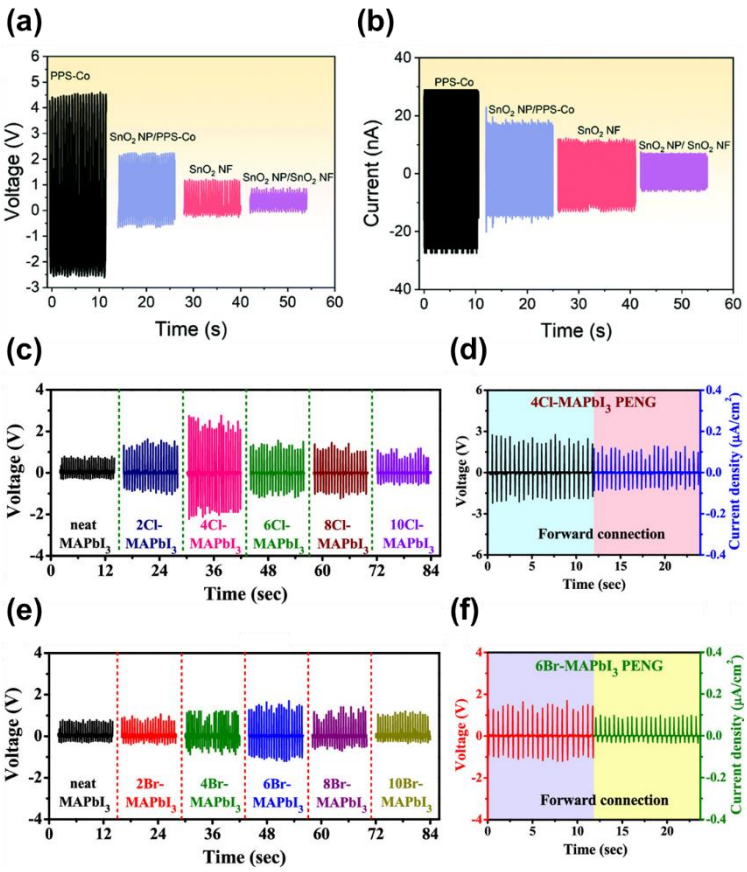

Figure 19. Piezoelectric energy harvesting performance of $MAPbI_3$, containing different underlayers. (a) output voltage, and (b) current. Reproduced with permission from ref. 115. Copyright © 2020 The Royal Society of Chemistry. (c-f) Comparison of the mechano-electrical output of devices containing the indicated wt % of mixed halide Cl or Br, $MAPbI_3$ piezoelectric devices. Reproduced with permission from ref. 116. Copyright © 2020 American Chemical Society.

Zhang and coworkers explored a $MAPbI_3$ perovskite-centered thin film as a stress-driven energy harvester that contained PVDF, polylactic acid (PLA) and tin dioxide (SnO_2) electrospun nanofibres (Figure 19).[115] The $MAPbI_3$ perovskite layer was deposited and infiltrated in SnO_2 nanofibres along with a PVDF/PLLA/SnO_2 (PPS–Co) net-like mesoporous composite scaffold; this acted to extend the substantial contact area and stability of the piezoelectric device. Furthermore, the piezoelectric electro-mechanical potential generated by the devices was measured while intermittently bending and relaxing the device. Figure 19a and b show the observed optimum output voltages of ~ 4.82 V, ~ 1.04 V and output currents of ~ 29.7 nA, ~ 10.32 nA for $MAPbI_3$-PPS-Co and $MAPbI_3$-SnO_2 nanofibre devices, respectively; the device area was 0.0625 cm^2.

Furthermore, the $MAPbI_3$-PPS-Co and $MAPbI_3$-SnO_2 nanofibre devices were decorated with a thin layer of SnO_2 nanoparticles (NPs), that were coated on a conductive flexible substrate (PET/ITO) to enhance the dielectric permittivity, improve underlayer anchorage on the substrate and reduce possible shunting effects due to leakage currents. The effect of the SnO_2 nanoparticle underlayers on the output signals of PPS–Co and SnO_2 nanofibre devices was evaluated, where the $MAPbI_3$-SnO_2 NP/PPS-Co and $MAPbI_3$-SnO_2 NP/SnO_2 nanofibre devices showed output voltages of ~ 2.29V, ~ 0.6 V and currents of ~ 16.79 nA, ~ 6.78 nA, respectively (Figure 19a and b). The SnO_2 NP/PPS–Co films showed slightly higher piezoelectric coefficient values (d_{33} ~ 123.93 pC N^{-1}) compared to those without SnO_2 NPs of PPS–Co (d_{33} ~ 118.85 pC N^{-1}), due to the presence of an ultrathin SnO_2 nanoparticle layer that slightly favored charge displacement and the resulting piezoelectric coefficient. This occurs since, $q = d_{33}F$, where q is

the charge displacement, d_{33} is the piezoelectric coefficient and F is the applied mechanical force.

Interestingly, Yoon and coworkers presented the exciting features of a mixed halide Cl or Br containing $MAPbI_3$ perovskite thin films for flexible nanogenerator applications (Figure 19c-f).[116] These mixed halide perovskite films were prepared with $MAPbI_3$ via a simple two-step spin-coating technique. Various concentrations of Cl- and Br-incorporated films were prepared and denoted as 2Cl-, 4Cl-, 6Cl-, 8Cl-, and 10Cl-$MAPbI_3$ and 2Br, 4Br-, 6Br-, 8Br-, and 10Br-$MAPbI_3$. Furthermore, the mechanical energy harvesting performance of $MAPbI_3$ and the mixed halide (Cl/Br) incorporated series of piezoelectric devices were studied by applying a load pressure of 0.5 MPa at a frequency of 2 Hz. The pure $MAPbI_3$ device exhibited an output voltage of ~ 0.78 V (Figure 19c and e). The highest output performance for the Cl/Br incorporated-$MAPbI_3$ devices was observed for the 4Cl-$MAPbI_3$ and 6Br-$MAPbI_3$ systems with an output voltage of ~ 2.75 V and ~ 1.62 V and current density of ~ 0.11 μA cm^{-2} and ~ 0.095 μA cm^{-2}, respectively, (Figure 19c-f). The enhancement of output device performance can be attributed to the higher piezo- and ferro-electric nature of the Cl/Br incorporated $MAPbI_3$ devices. In addition, alternative perovskite analogues such as $MASnI_3$ (~ 3.8 V) and $MASnBr_3$ (~ 1.56 V) have been explored for piezoelectric applications (See section 6.3). However, the overall piezoelectric energy harvesting performance of organic-inorganic energy harvester devices remain relatively low compared to those that use traditional and organic materials, limiting their use for commercial applications.

Recently, Xiong and coworkers reported on organometallic-based hybrid perovskite materials, [(ferrocenylmethyl)trimethylammonium]PbI_3 ((FMTMA)PbI_3), (FMTMA)$PbBr_2I$, and (FMTMA)$PbCl_2I$, which exhibit a relatively large piezoelectric response, that is coupled with a narrow bandgap (Figure 20).[117] Single-crystal X-ray diffraction analysis of these compounds indicated a similar hexagonal ABX_3-type perovskite structure, in which the infinite anionic linear chains are separated along the c-axis by the FMTMA cations (see the representative

example of (FMTMA)$PbCl_2I$ in Figure 20a). All compounds crystallized in the same polar non-centrosymmetric space group, *C*2, indicating potential for piezo- and ferro-electric properties. In addition, the absence of inversion symmetry was recognized by performing second harmonic generation measurements (SHG); see Figure 20b. The SHG intensity displayed a gradual increase on moving from (FMTMA)PbI_3 to (FMTMA)$PbBr_2I$ and to (FMTMA)$PbCl_2I$, suggesting that the change in the anionic framework leads to a structural distortion and a change in the dipole moment and polar nature of the molecular structure. Moreover, based on the crystal structures, the point charge model suggested the same increasing in polar character (from (FMTMA)PbI_3 to (FMTMA)$PbBr_2I$ and to (FMTMA)$PbCl_2I$) on calculating the spontaneous polarization, which increased from 0.005 to 0.354 and to 0.511 μC cm^{-2}, respectively.

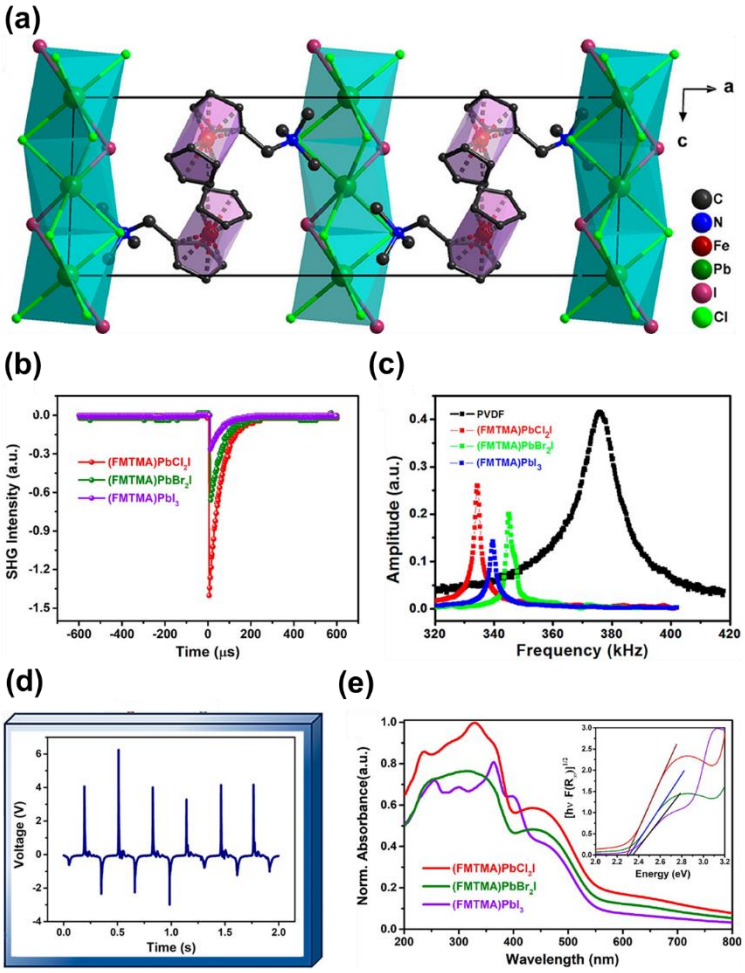

Figure 20. (a) Representations of (FMTMA)$PbCl_2I$, showing the hexagonal ABX_3-type perovskite crystal structure along the 'c' axis. (b) Comparison of the SHG intensity for (FMTMA)PbI_3, (FMTMA)$PbBr_2I$, and

(FMTMA)$PbCl_2I$. (c) PFM resonance peaks of PVDF, (FMTMA)$PbCl_2I$, (FMTMA)$PbBr_2I$, and (FMTMA)PbI_3. (d) Output voltage of piezoelectric (FMTMA)$PbCl_2I$ device. (e) UV−vis absorbance spectra of (FMTMA)PbI_3, (FMTMA)$PbBr_2I$, and (FMTMA)$PbCl_2I$. The inset shows the Tauc plot for determining the band gap. Reproduced with permission from ref. 117. Copyright © 2020 American Chemical Society.

Figure 20c shows a PFM analysis of the most substantial peak for PVDF, followed by (FMTMA)$PbCl_2I$, (FMTMA)$PbBr_2I$ and (FMTMA)PbI_3. Here, PVDF was used as a standard with a known $d_{33} \sim 33$ pC N^{-1}. The estimated d_{33} values for hybrid perovskite compounds varied from 20.6, 15.4, and 10.6 pC N^{-1}, for (FMTMA)$PbCl_2I$, (FMTMA)$PbBr_2I$, and (FMTMA)PbI_3, respectively, in agreement with the theoretically calculated values. Furthermore, the piezoelectric energy harvesting capability of a (FMTMA)$PbCl_2I$-based device was studied. The resultant output voltages reached 4 V by applying an applied mechanical force (Figure 20d). In addition to the piezoelectric nature, these hybrid perovskite compounds also exhibited semiconducting behavior (Figure 20e). The optical band gap was calculated from ultraviolet−visible (UV−vis) absorption spectra. From the Tauc plots (inset of Figure 20e), the calculated band gaps (*Eg*) were found to be 2.37, 2.32 and 2.28 eV for (FMTMA)PbI_3, (FMTMA)$PbBr_2I$, and for (FMTMA)$PbCl_2I$, respectively.

5.2 Transition metal-halides

Despite the challenges of designing and regulating multiaxial molecular ferroelectrics, they have attracted interest for piezoelectric harvesting applications due to their multiple equivalent polarization directions, tenability, and flexibility compared to the conventional inorganic systems. Recently, Xiong and coworkers developed a piezoelectric energy harvesting system based on multiaxial ferroelectrics, $[(CH_3)_3NCH_2X]FeBr_4$ ([TMXM]$FeBr_4$, X = F, Cl, Br, I) by precise molecular design (Figure 21).[118] By introducing a "*quasi-spherical theory*" (chemical design of cations in the compound), four multiaxial molecular ferroelectrics were designed, namely (TMFM)$FeBr_4$ (TMFM, trimethylfluoromethylammonium), (TMCM)$FeBr_4$ (TMCM, trimethylchloromethylammonium), (TMBM)$FeBr_4$ (TMBM,

trimethylbromomethylammonium), and (TMIM)$FeBr_4$ (TMIM, trimethyliodomethylammonium), which exhibit excellent piezo- and ferro-electric properties. The polar structures of these compounds were characterized by performing a ferroelectric polarization reversal experiment and the measured values ranged for ~ 3 to ~ 6 μC cm^{-2} (Figure 21a). Among these materials, (TMCM)$FeBr_4$ and (TMBM)$FeBr_4$ exhibited the larger ferroelectric polarization, which is related to a halogen-halogen interaction, the X···Br (X = F, Cl, Br, I) contacts in which Cl···Br and Br···Br show a stronger interaction than the respective F···Br and I···Br in (TMFM)$FeBr_4$ and (TMIM)$FeBr_4$. Furthermore, the piezoelectric harvesting performance of a (TMFM)$FeBr_4$ film, fabricated in a electrode-(TMFM)$FeBr_4$-electrode device configuration, was evaluated by subjecting the harvester to a mechanical force, (Figure 21c). The piezoelectric voltage produced was 2.2 V, demonstrating the effective electromechanical energy conversion capabilities of (TMFM)$FeBr_4$.

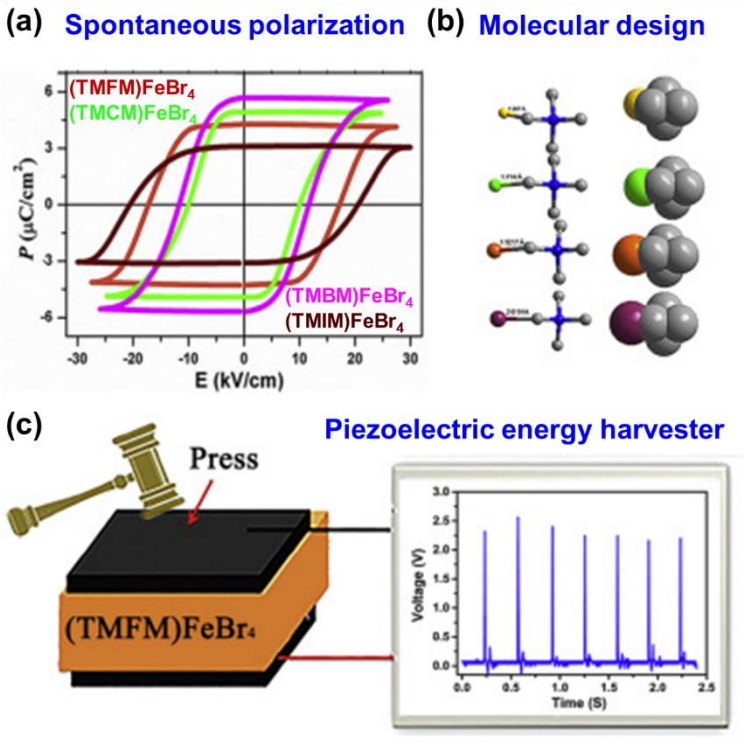

Figure 21. (a) *P-E* hysteresis loops of (TMFM)$FeBr_4$, (TMCM)$FeBr_4$, (TMBM)$FeBr_4$, and (TMIM)$FeBr_4$ measured at 323 K. (b) View of the molecular design strategies used to obtain polar structures. (c) Schematic diagram and the generated output voltages of PEH based on (TMFM)$FeBr_4$ film. Reproduced with permission from ref. 118. Copyright © 2020, Elsevier Ltd.

Recently, Ye and coworkers developed a one-dimensional perovskite-type organic−inorganic hybrid compound $[(CH_2)_3NH_2S]CdBr_3$, which exhibited piezo- and pyro-electric behavior (Figure 22).[119] The single-crystal X-ray diffraction analysis of $[(CH_2)_3NH_2S]CdBr_3$ revealed an orthorhombic polar space group of $Cmc2_1$ at both 213 K (low-temperature phase, LTP) and 293 K (room temperature phase, RTP), displaying a 1D hexagonal perovskite structure. The structure constituted an infinite array of face-sharing $[CdBr_6]$ octahedra along the polar c-axis and the organic thiazolidinium cations were situated between the chains (Figure 22a and b). The main difference between the RTP and LTP experiments was the orientational states of the thiazolidinium cations. Interestingly, it retained the same polar space group, indicating an isostructural phase change. The SHG response of the powder sample $[(CH_2)_3NH_2S]CdBr_3$ was measured in the heating and cooling cycle from 220 to 320 K, indicating the absence of a non-centrosymmetric to centrosymmetric phase transition.

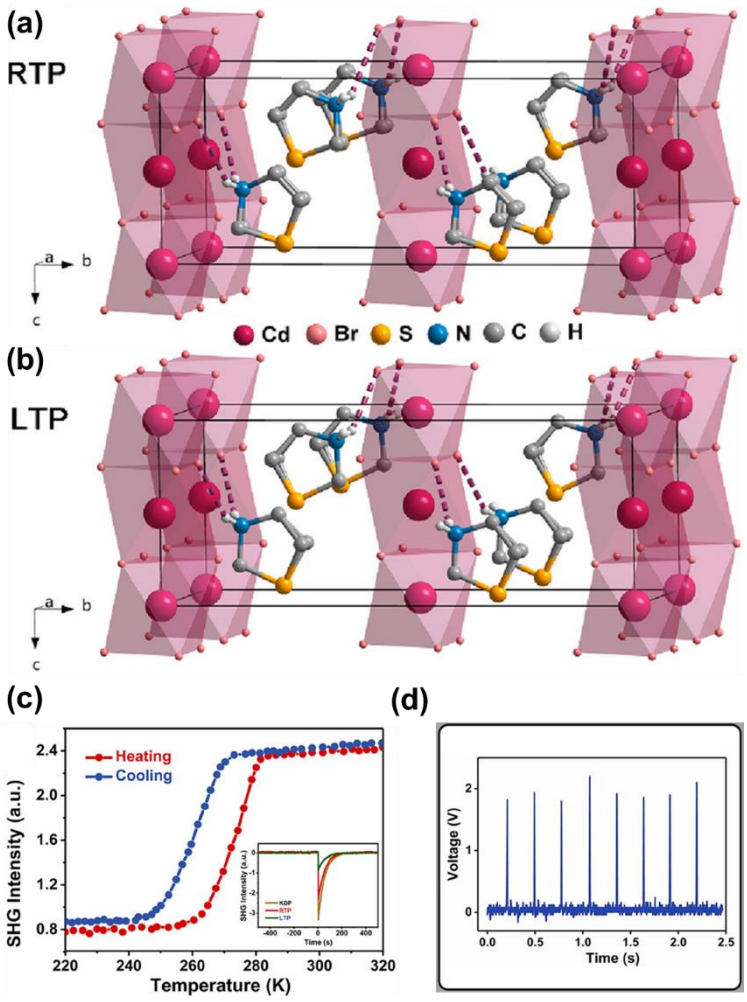

Figure 22. Representations of the crystal structures of $[(CH_2)_3NH_2S]CdBr_3$ at 293 K (a) and 213 K (b), revealing the main differences in the orientational states of the thiazolidinium cations. (c) Temperature-dependent SHG signal of $[(CH_2)_3NH_2S]CdBr_3$ (inset: the traces of SHG signals for potassium dihydrogen phosphate (KDP) and $[(CH_2)_3NH_2S]CdBr_3$). (d) Generated piezoelectric output voltages of a $[(CH_2)_3NH_2S]CdBr_3$-based device. Reproduced with permission from ref. 119. Copyright © 2020 American Chemical Society.

Figure 22c shows the high-intensity SHG signal for the RTP compared to the LTP and a KH_2PO_4 reference sample. During the cooling stage, the RTP transitioned to the LTP at approximately 284 K and consequently the SHG signal intensity gradually decreased and remaind stable. However, the RTP and LTP crystal structures were the same, with the dynamic motion of organic cation responsible for the weakening SHG response in the LTP. The larger size single-crystals of $[(CH_2)_3NH_2S]CdBr_3$ were used for direct piezoelectric coefficient measurements, inferring d_{33} values of ~ 15 pC N^{-1} along the [001] direction. Furthermore, a $[(CH_2)_3NH_2S]CdBr_3$ harvesting device was fabricated using conductive copper electrodes with a generated output voltage of approximately 2.0 V in the c-axis direction (Figure 22d).

5.3 Alkali metal-halides

Recently, Cho and coworkers developed a device based on cesium lead bromide ($CsPbBr_3$) for piezoelectric energy harvesting and sensing applications (Figure 23).[120] Thin films of $CsPbBr_3$ were fabricated over an ITO-coated soda lime silicate glass substrate via a spin-coating method, followed by a thermal annealing process at 70 ˚C for 5 min. PFM studies of the $CsPbBr_3$ thin film showed field-dependent piezoelectric poling behavior with typical butterfly loop curves (Figure 23b). The highest piezoelectric coefficient value of 40.3 pm V^{-1} was obtained for a maximal poling electric field of 24.9 kV cm^{-1}. The high degree to piezoelectricity can be attributed to the structural distortions of the $PbBr_6$ octahedra in $CsPbBr_3$. Furthermore, thin films of $CsPbBr_3$ passivated with PDMS layers were prepared for piezoelectric energy harvesting applications. Figure 23c and d show the electro-mechanical characteristics before and after a poling process applied to a thin film of $CsPbBr_3$ at different concentrations ranging

from 0.1 to 0.4 M. An output voltage of 11.7 V and output current of 147 nA were observed for an unpoled device of $CsPbBr_3$ at 1 Hz. In contrast, an improved output voltage (~ 16.4 V) and output current (~ 604 nA) were achieved after subjecting the film to an electric poling treatment at 24.9 kV cm^{-1}, indicating improved domain alignment of the $CsPbBr_3$ thin film in the poled devices (Figure 23e and f). Furthermore, the high performance of these devices was utilized for sensing signals, where thin-film $CsPbBr_3$-based devices were attached to a variety of human parts. By performing a range of biomechanical movements such as blinking, finger motion, coughing and yawning, the generated output currents were found to be ~ 0.6, ~ 2.8, ~ 4.8 and ~ 1.9 nA, respectively. These studies potential applications of the inorganic halide perovskite materials for effective energy harvesting and sensing of physiological motions.

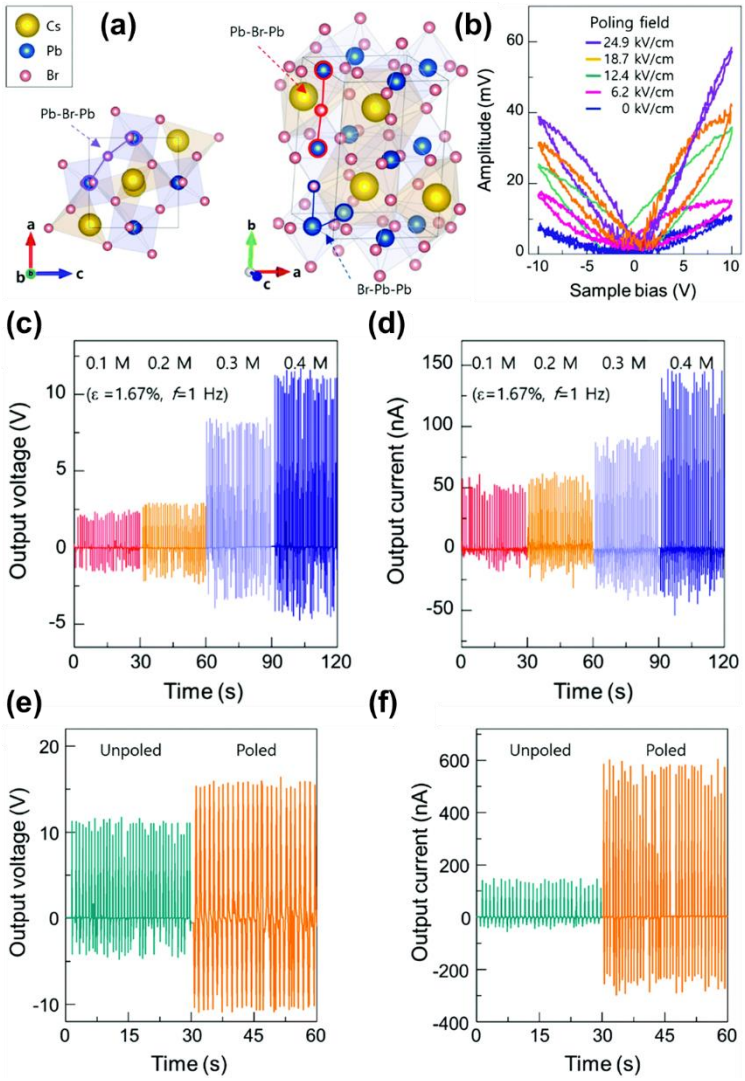

Figure 23. (a) Representations of lattice distortion with Pb-centered Br_6 cage rotations in $CsPbBr_3$ with different crystallographic axes [ac-plane (left) and along the b-axis (right)]. (b) Butterfly loops of perovskite $CsPbBr_3$ films under different poling conditions. (c) Open-circuit voltage and (d) short-circuit current of the $CsPbBr_3$ PEHs processed with different precursor solution concentrations ranging from 0.1 M to 0.4 M, measured under a repetitive bending strain of 1.67 % and the bending frequency of 1 Hz. (e) Output voltage and (f) output current of a $CsPbBr_3$-based device resulted from a poling electric field at 24.9 kV cm^{-1}. Reproduced with permission from ref. 120. Copyright © 2020 The Royal Society of Chemistry.

Table 3 provides a summary of the output voltage, current and power of organic-inorganic hybrid energy harvesters in response to a mechanical input, where the voltage ranges from 0.6 V to 16.4 V and current from 6.78 nA to 604 nA.

Table 3. Summary of output performance of organic-inorganic hybrid energy harvesters discussed in section **5.**

Material type	Voltage (Open circuit)	Current/current density	Power/power density	Application/Input	Area	Ref.
$MAPbI_3$ (non-poled)	1 V	50 nA cm^{-2}	-	0.5 MPa	1.0 x 1.0 cm^2	113
$MAPbI_3$ (poled)	2.7 V	140 nA cm^{-2}	-	0.5 MPa	1.0 x 1.0 cm^2	113
$MAPb_{1-x}Fe_xI_3$ (x = 0.07) (non-poled)	4.52 V	0.50 µA cm^{-2}	-	0.5 MPa, 1 Hz	1 x 1 cm^2	114
$MAPb_{1-x}Fe_xI_3$ (x = 0.07) (poled)	7.29 V	0.88 µA cm^{-2}	-	0.5 MPa, 1 Hz	1 x 1 cm^2	114
$MAPbI_3$-PPS-Co	4.82 V	29.7 nA	-	bending	0.0625 cm^2	115
$MAPbI_3$-SnO_2 NFs	1.04 V	10.32 nA	-	bending	0.0625 cm^2	115
$MAPbI_3$-SnO_2 NP/PPS-Co	2.29 V	16.79 nA	-	0.2 N	0.0625 cm^2	115
$MAPbI_3$-SnO_2 NP/SnO_2 NFs	0.6 V	6.78 nA	-	0.2 N	0.0625 cm^2	115
$MAPbI_3$ (non-poled)	0.78 V	-	-	0.5 MPa, 2 Hz	1 × 1 cm^2, 2 × 2 cm^2	116
$MAPbI_3$ (poled)	2.32 V	0.18 µA cm^{-2}	-	0.5 MPa, 2 Hz	1 × 1 cm^2, 2 × 2 cm^2	116
4Cl-$MAPbI_3$ (non-poled)	2.75 V	0.11 µA cm^{-2}	-	0.5 MPa, 2 Hz	1 × 1 cm^2, 2 × 2 cm^2	116
4Cl-$MAPbI_3$ (poled)	5.9 V	0.61 µA cm^{-2}	1.3 µW cm^{-2}	0.5 MPa, 2 Hz	1 × 1 cm^2, 2 × 2 cm^2	116
6Br-$MAPbI_3$ (non-poled)	1.62 V	0.095 µA cm^{-2}	-	0.5 MPa, 2 Hz	1 × 1 cm^2, 2 × 2 cm^2	116
6Br-$MAPbI_3$ (poled)	4.45 V	0.37 µA cm^{-2}	0.6 µW cm^{-2}	0.5 MPa, 2 Hz	1 × 1 cm^2, 2 × 2 cm^2	116
$(FMTMA)PbCl_2I$	4 V	-	-	-	-	117
$(TMFM)FeBr_4$	2.2 V	-	-	-	-	118
$[(CH_2)_3NH_2S]CdBr_3$	2 V	-	-	-	-	119
$CsPbBr_3$ (non-poled)	11.7 V	147 nA	-	Strain of 1.67%, 5 Hz	5 cm^2	120

$CsPbBr_3$ (poled)	16.4 V	604 nA	-	Strain of 1.67%, 5 Hz	5 cm^2	120
$MASnI_3$	3.8 V	0.35 μA cm^{-2}	-	0.5 MPa, 1 Hz	1 x 1 cm^2	137
$MASnBr_3$	1.56 V	0.58 μA cm^{-2}	-	0.5 MPa, 5 Hz	3 x 3 cm^2	138

6. Organic-Inorganic Hybrid Piezoelectric Composite Energy Harvesters

6.1 Lead halide based perovskite composites

In addition to organic-inorganic hybrids in bulk and thin film form, polymer matrix composite materials are studied for piezoelectric energy harvesting application. This can enable larger area, thicker and more compliant geometries to be formed, compared to thin film-based organic-inorganic hybrid energy harvesters. Composites are therefore more attractive for stretchable and flexible smart electronics applications.

Recently, Zheng and coworkers developed a high-performance and flexible PEH composed of formamidinium lead bromide ($FAPbBr_3$) nanoparticles embedded in a PDMS polymer (Figure 24).[121] Composite films were prepared via homogeneously mixing $FAPbBr_3$ nanoparticles with polymeric PDMS, followed by spin-coating onto an ITO–coated flexible PET substrate. A range of weight percentages of $FAPbBr_3$ nanoparticles (5, 20, 35 and 50 wt %) were embedded in PDMS and the best performing composite based on 35 wt % $FAPbBr_3$–PDMS exhibited the highest peak output voltage of 8.5 V, with a current density of 3.8 μA cm^{-2} (Figure 24a and b). Furthermore, the generated output voltages from the $FAPbBr_3$–PDMS device were employed to charge a 47 nF capacitor that was able to successively illuminate light-emitting diodes using a full-wave bridge four-diode rectifier circuit (Figure 24c and d).

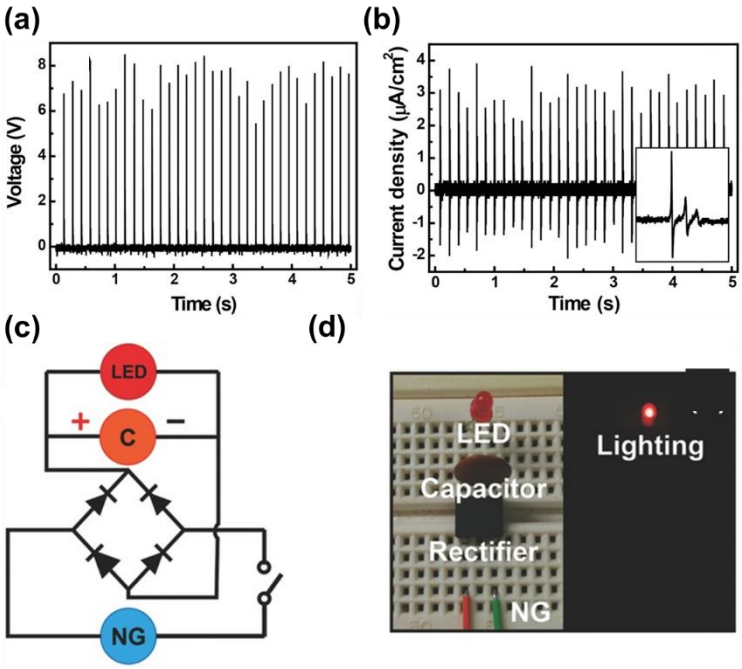

Figure 24. (a) Output voltage and (b) current density obtained for a $FAPbBr_3$-PDMS-based composite device. (c) and (d) Full-wave bridge four-diode rectifier circuit diagram and the photograph of charging a 47 nF capacitor to light a light-emitting diode (LED) under a periodical vertical compression of 0.5 MPa at a frequency of 7 Hz. Reproduced with permission from ref. 121. Copyright © 2016 WILEY-VCH Verlag GmbH & Co. KGaA, Weinheim.

In 2017, Zheng and coworkers fabricated a similar piezoelectric nanogenerator based on $FAPbBr_3$ NPs embedded in a piezoelectric PVDF polymer (Figure 25).[122] The composite film $FAPbBr_3$ NPs@PVDF film was prepared using a simple solution casting method by mixing $FAPbBr_3$ NPs into a homogenous solution containing PVDF polymer. The prepared composite films were placed between Au and Cr coated flexible PET electrodes for piezoelectric energy harvesting (Figure 25a).

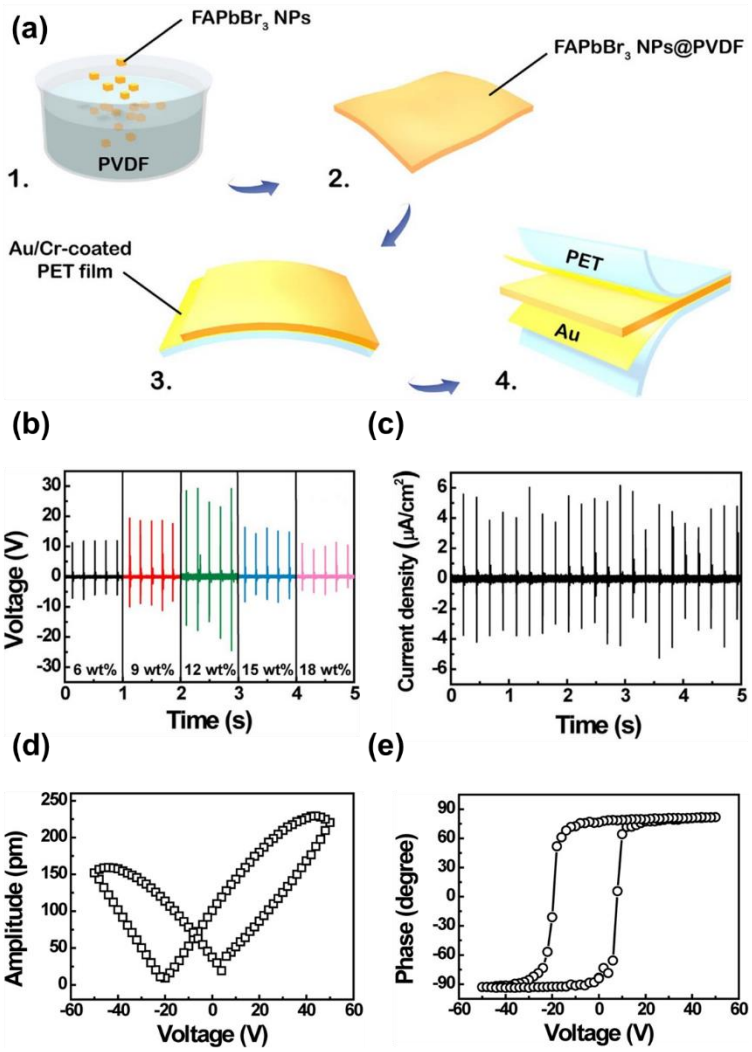

Figure 25. (a) Procedure for preparing composite films of $FAPbBr_3$ NPs@PVDF. (b) Output voltage and (c) current density of $FAPbBr_3$ NPs@PVDF nanogenerator under a selected area of 1.2 x 1.4 cm^2. (d) Piezo amplitude *vs* voltage curve and (e) phase *vs* voltage hysteresis loop of a 12 wt % $FAPbBr_3$ NPs @PVDF composite film. Reproduced with permission from ref. 122. Copyright © 2017 Elsevier Ltd.

The output device performance was studied based on various wt % of $FAPbBr_3$ NPs in PVDF polymer (6, 9, 12, 15 and 18 wt %). The output voltage of these devices was shown to increase with filler content from 6 to 12 wt % (10–25V) and to decrease from 15 to 18 wt % (15–10V), indicating a reduction in piezoelectric polarization of composite devices at higher loading levels (Figure 25b). A maximum output voltage of 30 V and current density of 6.2 μA cm^{-2} were observed for the optimal 12 wt % $FAPbBr_3$ NPs @PVDF poled device (Figure 25b and c). Furthermore, PFM measurements also validated the piezoelectric behavior of these composite films. Figure 25d and e reveals the PFM results of amplitude curve and phase hysteresis loop

for the concentration of 12 wt % $FAPbBr_3$ NPs@PVDF composite. The amplitude *vs.* voltage plot displayed a butterfly-shaped curve (classical strain-electric field behavior) (Figure 25d). The phase *vs.* voltage plot also formed a hysteresis loop (180° domain switching behavior), indicating the piezo- and ferro-electric properties of the 12 wt % $FAPbBr_3$ NPs @PVDF film (Figure 25e).

Interestingly, Ban and coworkers developed a hybrid mixed halide material $FAPbBr_2I$, for piezoelectric applications in combination with PVDF polymer (Figure 26).[123] The $FAPbBr_2I$-PVDF composites show a highly porous structure that can enlarge the bulk strain in the composite films, leading to an enhancement in device piezo-potential. The dipoles in the $FAPbBr_2I$-PVDF composites were aligned via an electrical poling process for 2–3 hours at an electric field of 50–120 V μm^{-1}. The final device was fabricated by placing composite films between two thin copper electrodes and applying a thermal lamination method to secure the device between flexible polyester substrates (Figure 26a). Figure 26b and c show the output performance for pure PVDF, porous PVDF (with ZnO nanoparticles) and a $FAPbBr_2I$–PVDF composite device. A high output voltage of 85 V (peak to peak) and output current (peak to peak) of 30 μA, were observed for the composite device with an active device area of 3.8 cm X 3.8 cm and at an applied frequency of 30 Hz (Figure 26b and c). The observed performance of the perovskite $FAPbBr_2I$–PVDF device was shown to be higher than pure or porous PVDF, revealing an enhancement in the strain-induced piezo-potential by the inclusion of $FAPbBr_2I$. Moreover, the $FAPbBr_2I$-PVDF device could harness energy from automobile vibrations and biomechanical movements, potentially indicating sustainable power source capabilities for self-powered internet of things applications.

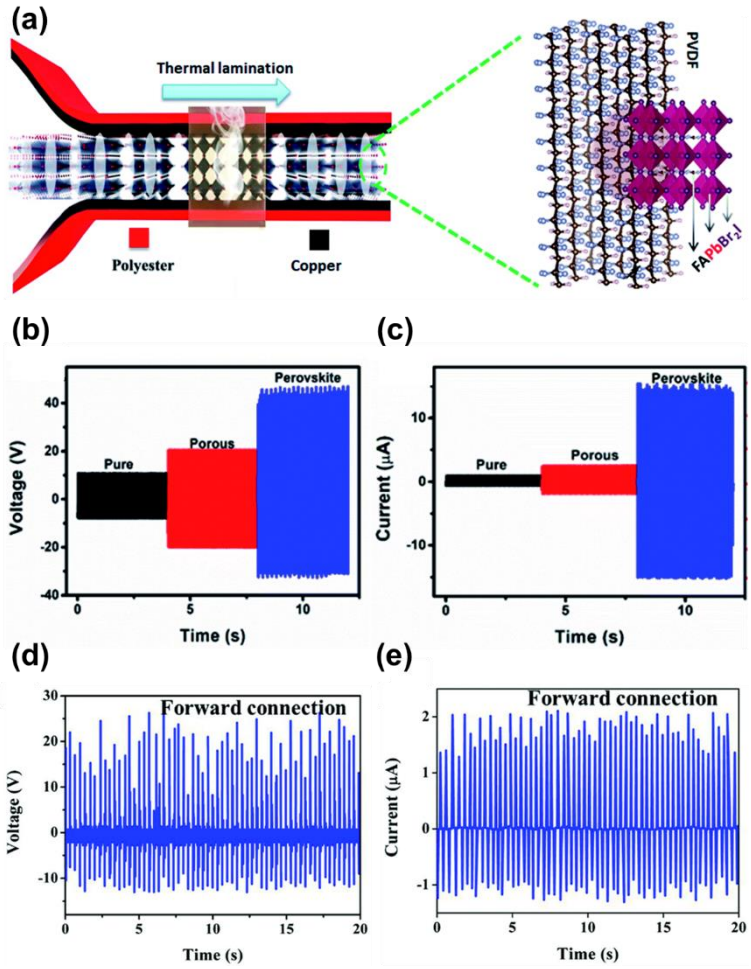

Figure 26. (a) Schematics of device architecture of a $FAPbBr_2I$@PVDF composite-based device. (b) Output voltage and (c) output current of devices composed of pure PVDF (black), porous PVDF with ZnO nanoparticles (red) and $FAPbBr_2I$@PVDF composites (blue). (d) Open circuit voltage and (e) short-circuit current of $FAPbBr_3$/PVDF composite device. Reproduced with permission from ref. 123 and 124. Copyright © 2020 The Royal Society of Chemistry.

An innovative aerogel-centered PEH device structure based on a $FAPbBr_3$/PVDF composite was reported by Khatua and coworkers in 2020 (Figure 26d and e).[124] Using a freeze-drying method, a uniform distribution of $FAPbBr_3$ nanoparticles was achieved in a $FAPbBr_3$/PVDF composite via *in situ* formation of $FAPbBr_3$ in the PVDF matrix. The unique fabrication method resulted in an interconnected porous $FAPbBr_3$/PVDF structure that enhanced the piezo- and ferro-electric properties of the composite devices. The self-poled aerogel film-based PEH produced an output voltage of ~ 26.2 V and power density of ~ 18.4 μA cm^{-2} by finger tapping and relaxation (Figure 26d and e). The device performance enhancement for $FAPbBr_3$/PVDF

aerogels was suggested to be due to a combination of the piezoelectric effect and interactions between the $FAPbBr_3$ particles and the γ-phase of the PVDF matrix. In addition, the $FAPbBr_3$/PVDF composite exhibited photodetector and photoactive piezoelectric energy harvesting capabilities, indicating the potential for multi-functional use of aerogel-based nanogenerators in the domain of energy harvesting and photodetector applications.

In addition, Sanyal and coworkers reported lattice defect induced piezoelectric polarization in $MAPbI_3$-PDMS composite devices, where crystal defects were monitored by a positron annihilation spectroscopy technique (Figure 27a).[125] A composite device based on 5 wt % $MAPbI_3$–PDMS showed a high piezoelectric output voltage above 100 V and a power density of 0.3 mW cm^{-3} during periodic impact by finger-tapping (Figure 27a).

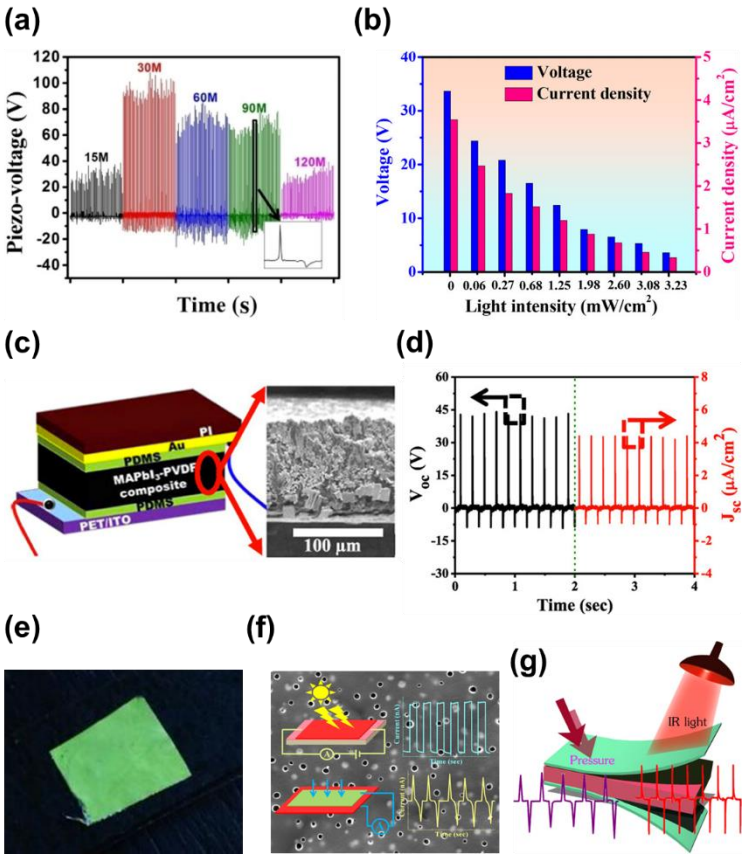

Figure 27. (a) Observed piezo-voltage of a $MAPbI_3$-based device (time-scale on the x-axis corresponds to 10 seconds). Reproduced with permission from ref. 125. Copyright © 2018 WILEY-VCH Verlag GmbH & Co. KGaA, Weinheim. (b) Comparison of piezoelectric peak output voltage and current density as a function of light intensity. Reproduced with permission from ref. 126. Copyright © 2020 American Chemical Society. (c)

Schematic of $MAPbI_3$-PVDF composite device; the cross-sectional scanning electron microscopy (SEM) image represents the thickness of the composite film. Reproduced with permission from ref. 127. Copyright © 2018 WILEY-VCH Verlag GmbH & Co. KGaA, Weinheim. (d) Output performance (V_{oc} and J_{sc}) of a $MAPbI_3$ nanogenerator. Schematic of perovskite methylammonium lead-halide-based hybrid devices. (e) $MAPbBr_3$-PVDF displaying piezoelectric energy harvesting and green-light emission. Reproduced with permission from ref. 128. Copyright © 2018 Elsevier Ltd. (f) $MAPbI_3$-PVDF applied for piezoelectric energy harvesting and photodetector application. Reproduced with permission from ref. 129. Copyright © 2018 American Chemical Society. (g) $MAPbI_3$-PVDF utilized for piezoelectric and pyroelectric energy harvesting application. Reproduced with permission from ref. 130. Copyright © 2019 American Chemical Society.

Yoon and coworkers described a light-driven piezo- and tribo-electricity in a $MAPbI_3$–PVDF composite device (Figure 27b).[126] The self-powered $MAPbI_3$–PVDF device was able to harvest mechanical energy and simultaneously operate as a light and pressure sensor, owing to the combined photoelectric, piezoelectric and triboelectric properties. The light-controlled PEH output device performance was measured using two electrodes by applying a load pressure of 300 kPa. The maximum peak voltage (~ 33.6 V) and current density (~ 3.54 μA cm^{-2}) observed under a light-off state gradually weakened with increasing light intensity from 0 to 3.23 mW cm^{-2} (Figure 27b). In addition, at a high light intensity of 3.23 mW cm^{-2}, the authors measured the output voltage (~ 3.6 V) and current density (~ 0.34 μA cm^{-2}). The large reduction (~ 90%) in output device performance during illumination could be rationalised by the formation of photogenerated charges that reduced the piezo-potential of the composite device.

Furthermore, Yoon and coworkers reported on a $MAPbI_3$–PVDF-based composite device, which exhibited a high dielectric and ferroelectric polarization. As a result, high piezo-voltage and current density of 45.6 V and 4.7 μA cm^{-2}, respectively, were observed for a composite film of 97.7 μm thickness (Figure 27c and d).[127] More recently, Mandal and coworkers have fabricated several organic-inorganic hybrid PEHs comprising $MAPbI_3$ and $MAPbBr_3$ NPs within a PVDF polymer. In addition to being employed in a piezoelectric energy harvester,

these materials exhibit attractive multi-fuctional properties in terms of green light emission, vibration sensitivity, photodetector and pyroelectric capabilities (Figure 27e-g).[128-130]

Developing high-performance piezoelectric particles for mechanical energy harvesters with a high intrinsic mechanical-electrical coupling is important for autonomous and self-powered sensors applications. Recently, Ban and coworkers developed organic-inorganic hybrid perovskite nanorods (NRs) of (4-aminotetrahydropyran)$_2$PbBr$_2$Cl$_2$ [(ATHP)$_2$PbBr$_2$Cl$_2$] that exhibits a large d_{31} of 64.2 pC N^{-1}, exceeding that of well-known PVDF polymer (d_{31}~ 21 pC N^{-1}) (Figure 28).[131] The piezoelectric [(ATHP)$_2$PbBr$_2$Cl$_2$] NRs were successfully synthesized at room temperature and the crystal structure reveal an intriguing Ruddlesden-Popper layered stacking where the organic cations (ATHP) were hydrogen bonded with the PbX_6 (X = Cl or Br) octahedra (Figure 28a). PFM analysis of the [(ATHP)$_2$PbBr$_2$Cl$_2$] shows an high d_{31}~ 64.2 pC/N, which is higher than a number of traditional perovskites and organic piezoelectric polymers (Figure 28c). The polarization (*P*) vs. voltage (*V*) hysteresis loop switching behavior and the current density (*J*)-voltage (*V*) curve can also be observed at room temperature. Solution drop-casting method was use to prepare the sample and the NRs film was cured between two ITO electrodes (the inset in Figure 28b). The observed saturated polarization (P_s) was 5.4 μC cm^{-2}, with two stable states with opposite polarization (J-V curve); see Figure 28b. Inspired by this, polymeric composites films of [(ATHP)$_2$PbBr$_2$Cl$_2$] were prepared with a combination with PDMS polymer. The composite films [(ATHP)$_2$PbBr$_2$Cl$_2$@PDMS] exhibit higher surface stress and improved flexibility, making it suitable for piezoelectric energy harvesting applications. The fabricated harvester produced a piezoelectric output voltage of 90 V and short-circuit current of 6.5 μA, with an applied compressive force of 4.2 N (4.66 kPa) (Figure 28d). Figure 28c, indicates the measured d_{33} of a neat PDMS device is close to zero, which indicates the non-piezoelectric nature of PDMS and the observed output characteristics are obtained exclusively from the addition of (ATHP)$_2$PbBr$_2$Cl$_2$ NRs. The d_{33} of the composite films increased linearly from 10 to 40 wt % of (ATHP)$_2$PbBr$_2$Cl$_2$ NRs and the observed values were found to be d_{33} ~19

to d_{33} ~ 56 pC/N. Furthermore, the increasing in g_{33} from 560 mV·m/N to a high value of 900 mV·m/N is consistent with the observed output peak to peak voltage from 30 to a maximum of 90 V (40 wt % $(ATHP)_2PbBr_2Cl_2$@PDMS). The higher d_{33} charge constant yields a maximum peak to the peak output current of 6.5 µA since current $I = d_{33}.[dF/dt]$.

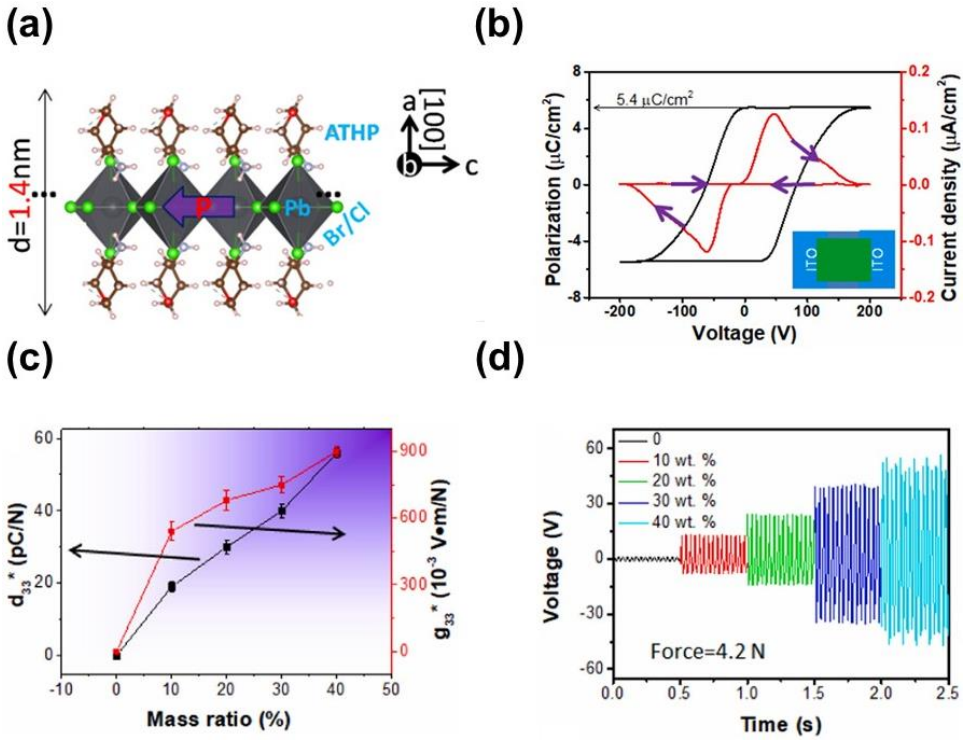

Figure 28. (a) Crystal structure view of $(ATHP)_2PbBr_2Cl_2$ showing Ruddlesden-Popper layered stacking in which the (ATHP) cations formed hydrogen-bonded interactions with PbX_6 (X = Cl or Br) octahedrons. (b) *P-E* hysteresis loop and current density measurements of $(ATHP)_2PbBr_2Cl_2$ (inset shows the fabricated NRs film sample with ITO electrodes). (c) Measured d_{33}* and g_{33}* for the composite film with different $(ATHP)_2PbBr_2Cl_2$ concentrations. (d) Output voltages of $(ATHP)_2PbBr_2Cl_2$@PDMS devices under the mechanical force of 4.2 N. Reproduced with permission from ref. 131. Copyright © 2021, Elsevier Ltd.

6.2 Alkali metal-halide composites

In addition, the output performance of these interesting PEH devices can potentially be improved. Due to the recent interest in alkali-metal halide perovskites, the piezoelectric energy harvesting properties of the all-inorganic AMX_3 materials (A = group 1 cation; M = Pb, Sn, and X = Cl, Br, I) were investigated. Unfortunately, the piezo- and ferro-electric properties of these materials are limited due to the difficulties in fabricating structurally stable samples. While the

piezo- and ferro-electric properties have been studied using theoretical approaches, experimentally demonstrated piezoelectric energy harvesting studies of this class of materials are currently limited.[132]

Chattopadhyay and coworkers reported an all-inorganic perovskite $CsPbBr_3$-based PVDF piezoelectric nanogenerator (PNG) (Figure 29).[133] A number of thin films with a range of wt % of $CsPbBr_3$ were prepared by embedding them within a PVDF polymer. These composites were designated as PNG 3, PNG 4, PNG 5, PNG 6 and PNG 7 where the numeric numbers represent the wt % of $CsPbBr_3$. In addition, the piezoelectric energy harvesting performance of the composite and neat PVDF unpoled devices (denoted as a RNG-reference nanogenerator) was evaluated. These studies led to a high open-circuit voltage, short-circuit current and output power values of 120 V, 35 μA, and 4.24 mW, respectively, in the composite containing 5 wt % $CsPbBr_3$–PVDF (PNG 5) resulting from simple mechanical movements of human body activities (Figure 29a and b). The best-performing PNG 5 showed an output that was dependent on the load resistance applied (10 kΩ to 10 MΩ) under a mechanical pressure load of 100 MPa (Figure 29c and d). The piezoelectric voltage increased with increasing load resistance and saturated at the highest level of load resistance. In contrast, the output current droped with an increasing amount of load resistance and followed the opposite trend as that of the output voltages. The maximum power output (P) occurs at an optimum of both high voltage (V) and current (I), since $P = VI$. This takes place when the impedance of the PEH and the electrical load (R_L) are matched, namely when $(1/R_L) = 2\pi f C_p$ where f is the frequency and C_p is the capacitance of the energy harvesting device. The high performance of the PNG 5 device was attributed to the high percentage of electroactive β-phase present in the PVDF due to the incorporation of the $CsPbBr_3$ filler. In addition to the electroactive behavior, the composites also exhibited photosensitivity under visible-light, indicating the potential of these devices in piezo-phototronic applications (Figure 29e and f).

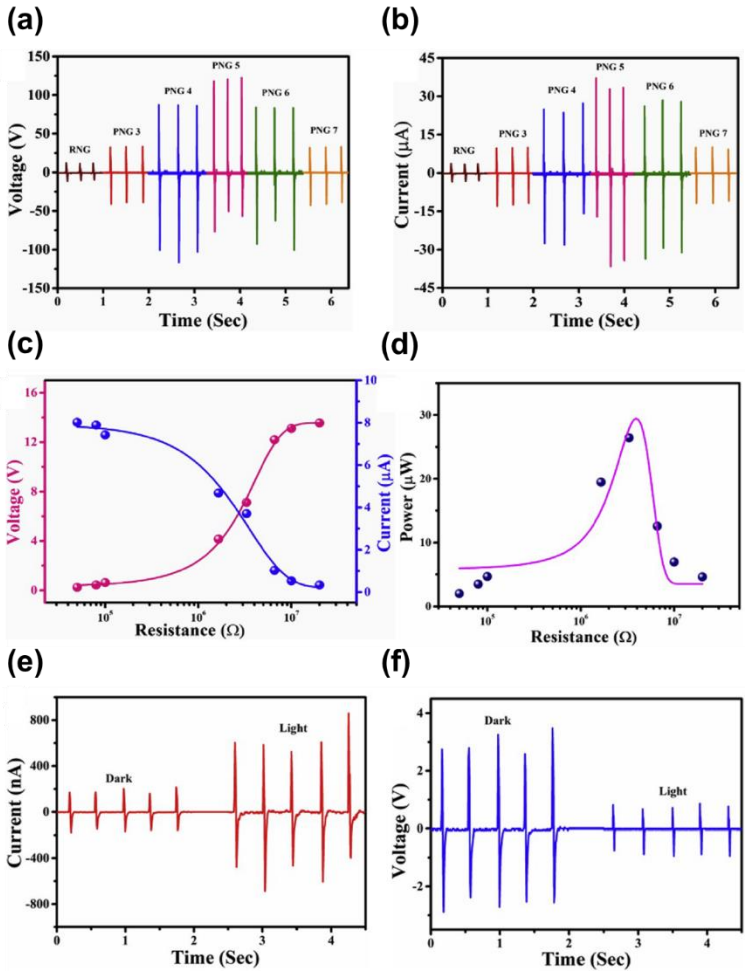

Figure 29. (a) Output voltage and (b) output current of all the $CsPbBr_3$–PVDF PNGs. (c) The output voltage, output current and (d) output power variation under various load resistance for PNG 5. (e) Calculated output current and (f) output voltage under dark and light conditions, with the same external applied stress. Reproduced with permission from ref. 133. Copyright © 2020, Elsevier Ltd.

Recently, Wang and coworkers reported a flexible piezoelectric nanogenerator comprising $CsPbBr_3$ quantum dots (QDs) doped with a poly(vinylidene fluoride−trifluoroethylene) P(VDF-TrFE) polymer (Figure 30).[134] Different concentrations of $CsPbBr_3$ QDs (0, 0.1, 0.2, 0.3, 0.4 and 0.5 wt.%) were used to prepare a range of wt.% of composite films with P(VDF-TrFE).

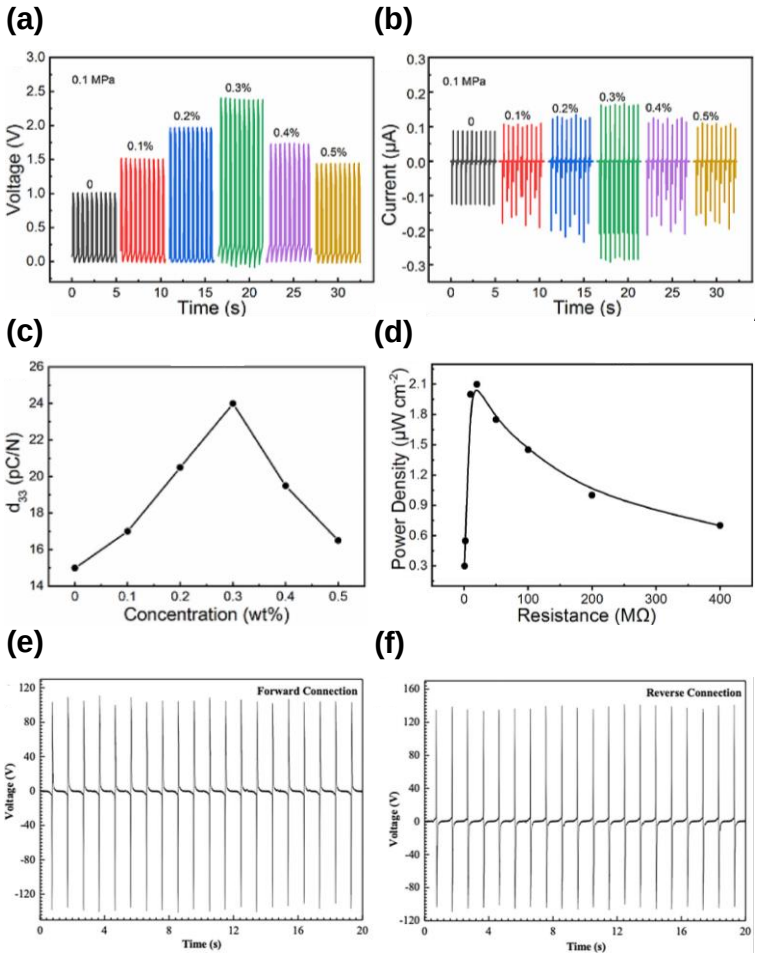

Figure 30. (a) Open-circuit voltage, (b) short-circuit current and (c) d_{33} coefficients of P(VDF-TrFE)/$CsPbBr_3$ composite nanogenerator. (d) Power density variation under a range of load resistance for the 0.3 wt % P(VDF-TrFE)/$CsPbBr_3$ composite nanogenerator. (e) and (f) Piezoelectric output voltage of the $CsPbBr_3$@PVDF composite device in the forward and reverse connections. Reproduced with permission from ref. 134. Copyright © 2021 American Chemical Society and ref. 135. Copyright © 2021 WILEY-VCH Verlag GmbH & Co. KGaA, Weinheim.

Figure 30a and b shows the open-circuit voltage and short-circuit current of the P(VDF-TrFE)/$CsPbBr_3$ devices containing different mass fractions of $CsPbBr_3$ QDs. The optimum observed open-circuit voltage was 2.4 V and short-circuit current was 0.17 μA for the composite with 0.3 wt % of $CsPbBr_3$ composite upon application of a pressure of 0.1 MPa (Figure 30a and b). The P(VDF-TrFE) doped with 0.3 wt % $CsPbBr_3$ QDs exhibited a higher open-circuit voltage (2.5×) and short-circuit current (2.2×) compared to pristine P(VDF-TrFE). In addition, $CsPbBr_3$ QDs exhibited a pressure-dependent open-circuit voltage behavior. The voltages were

shown to increase from 2.4 to 11.5 V when the applied pressures increased from 0.1 to 0.6 MPa. Furthermore, d_{33} measurements of all composite films revealed a maximum d_{33} ~ 24.5 pC N^{-1} for the 0.3 wt % P(VDF-TrFE)/$CsPbBr_3$ device (Figure 30c). The higher piezoelectric polarization of the 0.3 wt % P(VDF-TrFE)/$CsPbBr_3$ QDs relates to the enhancement of the beta phase and the smaller size (10 nm) of $CsPbBr_3$ QDs allowing to form more favorable ferroelectric domains. Figure 30d shows the power density dependence on th load resistance for the best performing 0.3 wt % P(VDF-TrFE)/$CsPbBr_3$ QDs device. The maximum power density attained was 2.1 μW cm^{-2} when the load resistance was 20 MΩ. This result demonstrates that the P(VDF-TrFE)/$CsPbBr_3$ QDs energy harvester is sensitive to the load resistance range due to the impedance mismatch between the piezoelectric source and resistive load. The same group reported a similar piezoelectric energy harvesting composite system composed of $CsPbBr_3$@PVDF, which exhibits a high open-circuit voltage of 103 V and a current density of 170 μA cm^{-2} (Figure 30e and f).[135] The difference in the voltage peak values between the forward and reverse connections indicates the difference in applied strain rate during application and removal of stress on the PEH device.

6.3 Tin halide composites

While lead-based organic-inorganic piezoelectric energy harvesters have been explored due to their excellent electromechanical response, the presence of toxic lead leads to environmental issues, which limit their use in medical and wearable electronic-skin applications. In contrast, lead-free perovskites, such as methylammonium tin iodide ($MASnI_3$), provide a range of advantages, such as reduced toxicity, decreased ecological damage, greater disposability and high piezoelectric coefficients (d_{33} ~ 100.9 pC N^{-1}).[58,136,137] Recently, Yoon and coworkers reported on flexible PEH devices based on pure $MASnI_3$ and composite $MASnI_3$–PVDF films (Figure 31a and b).[138] They synthesized stable perovskite $MASnI_3$ films under ambient conditions using a simple antisolvent-assisted collision technique. The $MASnI_3$–PVDF composite films were prepared by spraying $MASnI_3$ particles containing toluene solution over

the porous PVDF film. In addition, $MASnI_3$–PVDF films were annealed at 90 °C (2 h) and 130 °C for 2 h under ambient argon conditions to obtain the β-phase of PVDF. Moreover, the piezoelectric energy harvesting performance of the $MASnI_3$ films was enhanced by the incorporation of porous PVDF films. An output voltage of 3.8 V and 12 V and current density of 0.35 μA cm^{-2}, 4.0 μA cm^{-2} for the $MASnI_3$ and $MASnI_3$–PVDF poled devices, respectively, were observed (Figure 31a and b). The $MASnI_3$–PVDF hybrid device exhibited superior output performance compared to $MASnI_3$ films, indicating the enhancement in piezoelectric strain constant of the composite films.

In addition, Yoon and coworkers developed air-stable (over 120 days) and lead-free organo-ammonium-based tin bromide perovskites for piezoelectric energy harvesting (Figure 31c).[139] Composite films were prepared by mixing $MASnBr_3$ powders into a PDMS polymer in a toluene solution. The $MASnBr_3$−PDMS device was constructed using a flexible ITO-coated PET and Al-coated polyimide (PI) substrates (Figure 31c).

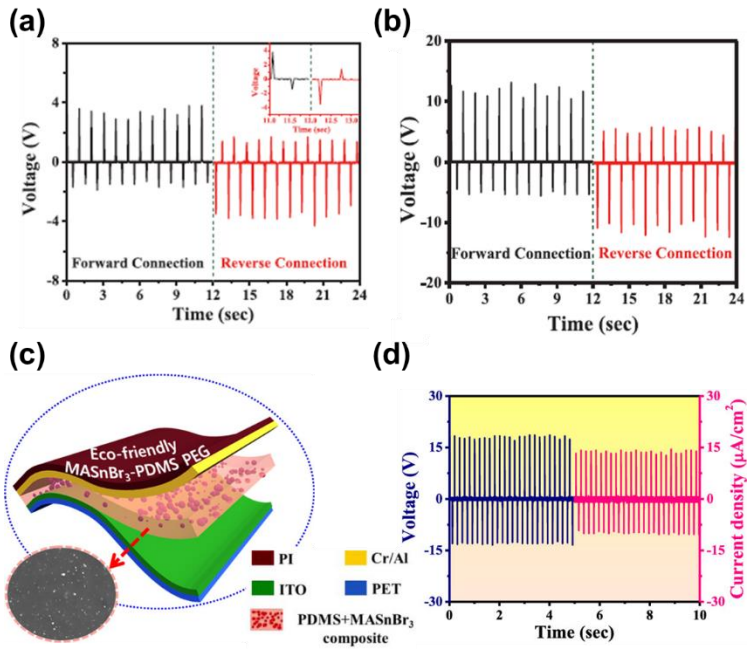

Figure 31. (a) and (b) Generated output voltage of poled-$MASnI_3$ and poled-PVDF-$MASnI_3$ PNGs with forward (black) and reverse (red) connections under an applied force of 0.5 MPa. (c) Schematic illustration of the $MASnBr_3$-PDMS nanogenerator with the enlarged cross-sectional scanning electron microscopy image of the 15 wt % $MASnBr_3$-PDMS device. (d) Measured output voltage and current density of the 15 wt % $MASnBr_3$-PDMS

device under a poling field of 55 kV cm^{-1}. Reproduced with permission from ref. 138. Copyright © 2019 Elsevier Ltd and ref. 139. Copyright © 2020 American Chemical Society.

The piezoelectric output of the non-poled 15 wt % $MASnBr_3$–PDMS device demonstrated an output voltage and current density of ~ 3.63 V and ~ 1.75 μA cm^{-2}, respectively. The observed performance was found to be higher than neat $MASnBr_3$ (~ 1.56 V), indicating the importance of interfacial polarization between polymer matrix and filler materials. The poled device showed improved output voltage and power density of ~ 18.8 V and ~ 74.52 μW cm^{-2}, respectively (Figure 31d). The enhanced performance of the $MASnBr_3$–PDMS device was related to the formation of interfacial polarization between the PDMS polymer and the $MASnBr_3$ particles. Interestingly, the poled 15 wt % $MASnBr_3$–PDMS device displayed excellent mechanical stability for more than 100 days and up to 10,000 cycles, indicating the long-term stability and durability of the $MASnBr_3$–PDMS device.

Most organic-inorganic hybrid piezoelectric materials contain the methylammonium (MA) cation, whereas formamidinium (FA) cation-based organic-inorganic hybrid energy harvesters are limited.[43] Replacing an organic MA cation with a larger FA cation leads to improved thermal and phase stability. In addition, the FA-based organic-inorganic compounds have several advantages, which include a larger ionic radius (r = 0.253 nm), long-term stability, reduced sensitivity to moisture and polar solvents, lower bandgap (~ 1.47 eV), broader absorption spectrum and improved energy harvesting performance.[105,140-142]

In 2019, Kabra and coworkers reported on a PEH based on FA tin iodide ($FASnI_3$) embedded within a PVDF polymer.[143] $FASnI_3$ and PVDF-based composite devices at a range of volume ratios (1:0, 0.2:0.8, 0.5:0.5, 0.8:0.2, 0:1) were fabricated and studied for piezoelectric energy harvesting applications. Measured at different frequencies of 5, 10, 15, 20, and 25 Hz, and the PEH device showed excellent output voltages of 7.28, 10.56, 19.6, 22.8, and 10.8 V (Figure 32a and b). The output voltages were shown to gradually increase with increasing frequency and reach the highest output voltage and power density of 23 V and 35.05 mW cm^{-2},

respectively, for a (50:50) wt % of $FASnI_3$:PVDF device (Figure 32a and b). Beyond 25 Hz, the PEH devices started to deform permanently, and the performance was reduced. In addition, the energy harvester based on 20 $FASnI_3$:80 PVDF and 0 $FASnI_3$:100 PVDF showed an output voltage of 12.2 V and 3.52 V, signifying that the optimum level loading of $FASnI_3$ particles is necessary for the best output device performance. Furthermore, the composite devices were utilized for a practical application of charging a capacitor and illuminating light emitting diodes (LEDs).

More recently, Ban and coworkers developed a vacancy-ordered organic-inorganic double perovskite structure of $TMCM_2SnCl_6$ (TMCM = trimethylchloromethylammonium), which displays a very high piezoelectric coefficient of $d_{33} \sim 137$ pC N^{-1} and a piezoelectric voltage coefficient $g_{33} \sim 980 \times 10^{-3}$ Vm N^{-1} (Figure 32c-f).[144] The hybrid compound $TMCM_2SnCl_6$ forms a large single crystal 1.8 cm in size. Polarisation–electric field (*P-E)* loop measurements of a thin film of $TMCM_2SnCl_6$ displayed a well-saturated hysteresis loop of ~ 8.7 μC cm^{-2}, along with low leakage current density behavior (Figure 32d). Furthermore, due to the high d_{33} and g_{33} coefficients, the $TMCM_2SnCl_6$ based composite films were fabricated with PDMS polymer for piezoelectric energy harvesting. The $TMCM_2SnCl_6$@PDMS device architecture showed force-dependent electromechanical responses with high output voltage and the current density values of 81 V and 2 μA, respectively, at an operating force of 4.9 N (Figure 32f).

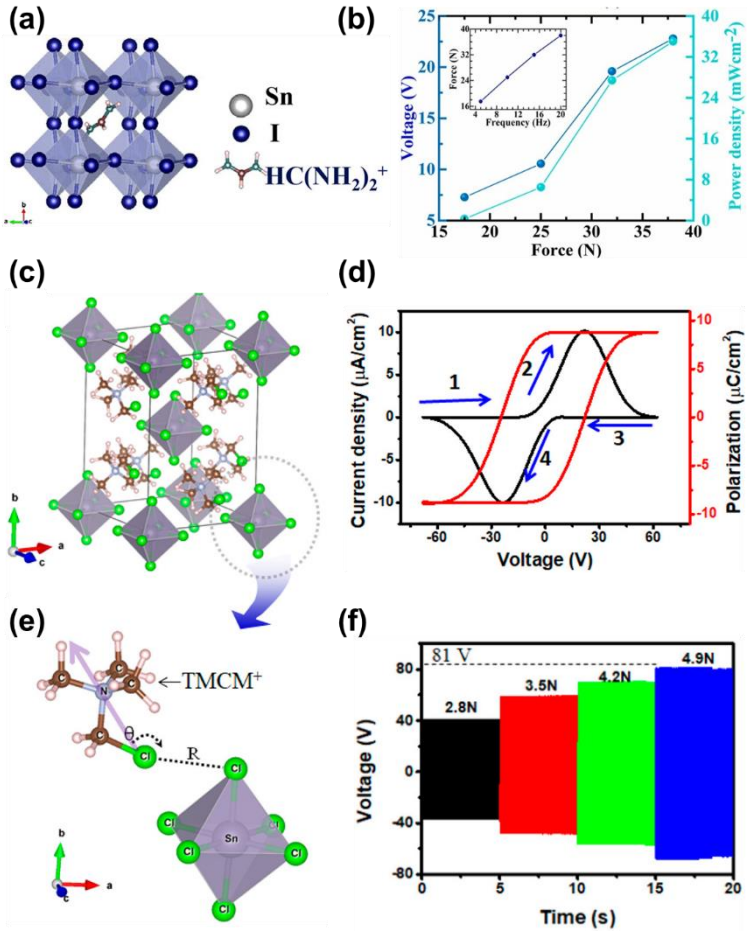

Figure 32. (a) Single-crystal X-ray diffraction structure of $FASnI_3$. (b) Piezoelectric energy harvesting of $FASnI_3$:PVDF showing output voltage and power density at different applied forces. The inset graph shows the change in force versus change in frequency from 5 to 20 Hz. (c) Single-crystal structure of vacancy ordered double perovskite $TMCM_2SnCl_6$. (d) Room temperature leakage current density *vs* voltage curve and polarization vs voltage hysteresis loop of thin-film $TMCM_2SnCl_6$. (e) Halogen bonded structure of $TMCM_2SnCl_6$. Dipole direction (see arrow) is shown from Cl to N in organic cation ($TMCM^+$). (f) Force-dependent piezoelectric output signals of $TMCM_2SnCl_6$@PDMS composite device. Reproduced with permission from ref. 143. Copyright © 2019 and ref. 144. Copyright © 2021, American Chemical Society.

6.4 Transition metal-halides and -pseudohalides and their composites

Recently, Boomishankar and coworkers developed a series of ammonium cation stabilized halogenometallates $[BnNMe_2R]_2CdBr_4$ (Bn = benzyl; R = Me, ^{n}Pr) which were shown to crystallize in acentric space groups compatible with piezo- and ferroelectric properties (Figure 33).[145] Structural investigation of these compounds showed the formation of discrete assemblies. *P-E* measurements on thin films revealed rectangular hysteresis loops with remnant polarization

values of P_r ~ 18.59 and P_r ~ 14.24 μC cm^{-2} for the compounds $[BnNMe_3]_2CdBr_4$ and $[BnNMe_2{}^nPr]_2CdBr_4$, respectively (Figure 33c and d). A range of wt % flexible composite films (1, 5, 10 and 20 wt %) were prepared with a PDMS polymer and subjected to piezoelectric energy harvesting evaluation at an applied frequency of 25 Hz and an applied force of 40 N. Maximum output voltages of 52.9 and 63.8 V and power density of 13.8 and 37.1 μW cm^{-2} were observed for the 5 wt % $[BnNMe_2Me]_2CdBr_4$–PDMS and 10 wt % $[BnNMe_2{}^nPr]_2CdBr_4$–PDMS composites, respectively (Figure 33e and f).

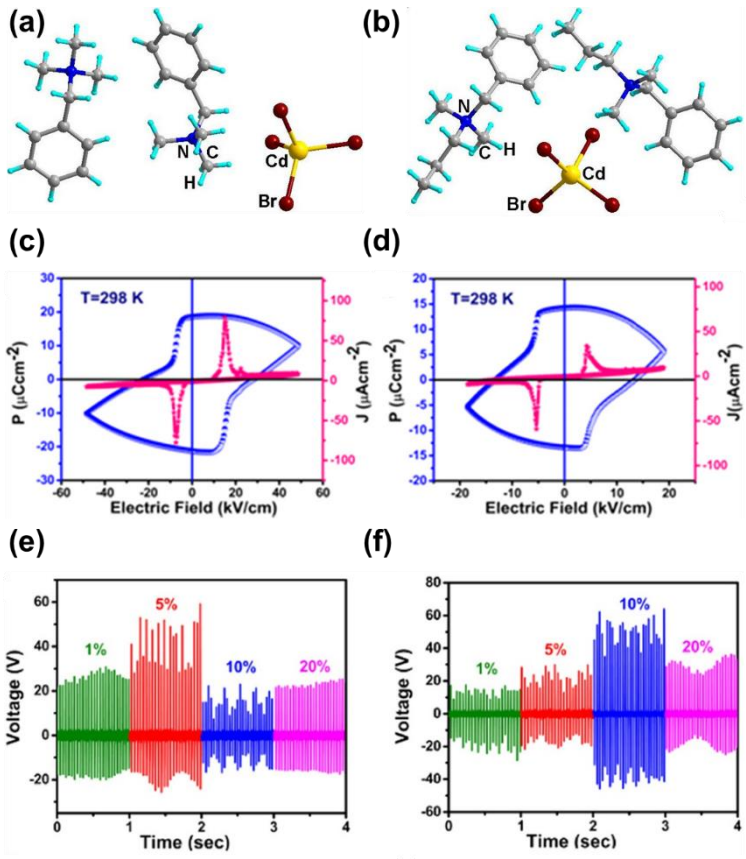

Figure 33. Asymmetric units of (a) $[BnNMe_3]_2CdBr_4$ and (b) $[BnNMe_2{}^nPr]_2CdBr_4$. *P*–*E* hysteresis loops of (c) $[BnNMe_3]_2CdBr_4$ and (d) $[BnNMe_2{}^nPr]_2CdBr_4$ along with their corresponding leakage current density plots measured on their thin films of ~ 20 μm thickness. (Concentration-dependent mechanical energy harvesting performance of (e) $[BnNMe_2Me]_2CdBr_4$–PDMS and (f) $[BnNMe_2{}^nPr]_2CdBr_4$–PDMS composite devices. Reproduced with permission from ref. 145. Copyright 2019 © American Chemical Society.

Later, the same research group established a PEH based on an unusual ABX_3 type organic-inorganic hybrid compound, $[Me_3NCH_2CH_2OH]CdCl_3$ (Figure 34).[146] Figure 34a shows the

molecular structure of $[Me_3NCH_2CH_2OH]CdCl_3$, which exhibits a 1D chain structure of edge-sharing $CdCl_5O$ octahedra that are coordinated with (2-hydroxyethyl)trimethylammonium (HETMA) cations. The two equatorial chloride ions act as a μ_2-bridging linker. The hydroxyl group of the HETMA cation is coordinated with the Cd metal center, further leading to form a zwitterionic structure. In addition, the metal-bound hydroxyl (O-H) groups are involved in the inter-molecular hydrogen-bonded interactions with the terminal Cl^- ions of the neighboring Cd atoms along the polar b-axis. Ferroelectric measurements performed on a single-crystal of this compound revealed a macroscopic polarization reversal with a remnant polarization value of P_r ~ 17.1 μC cm^{-2} (Figure 34b).

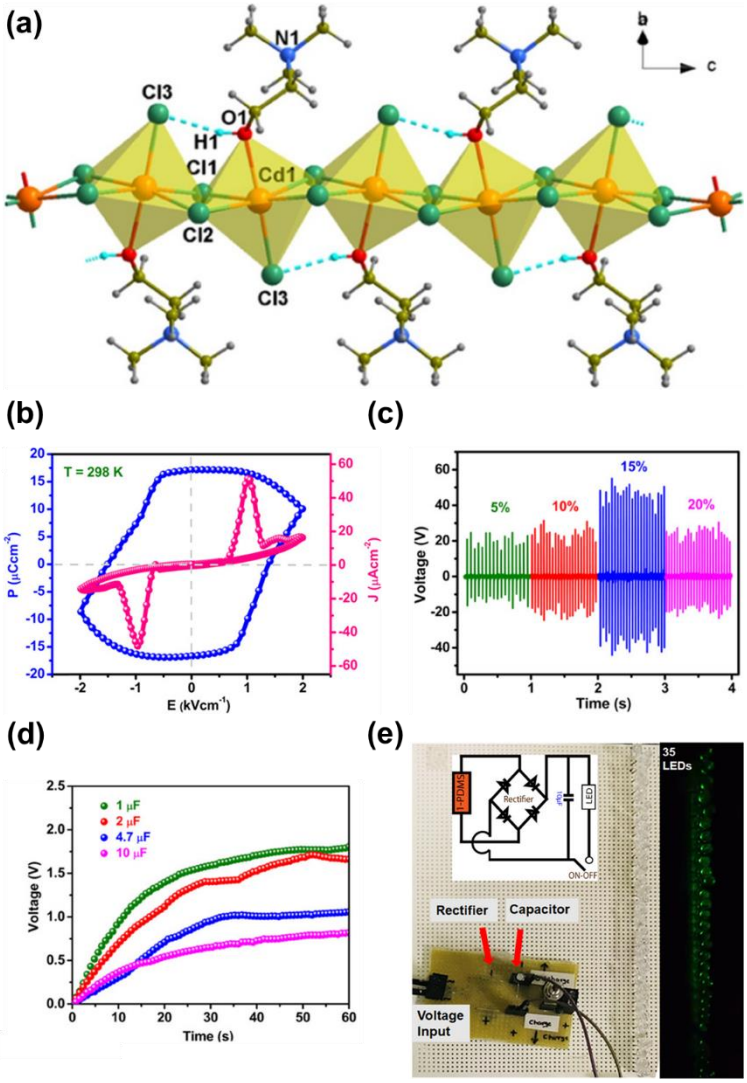

Figure 34. (a) Crystal structure of $[Me_3NCH_2CH_2OH]CdCl_3$ represented as the edge-sharing $CdCl_5O$ octahedra (shaded in yellow color). Hydrogen-bonded interactions between O-H and Cl ions are designated by dotted lines.

(b) *P*−*E* hysteresis loop of a single crystal of $[Me_3NCH_2CH_2OH]CdCl_3$. (c) Output voltage of all the wt % $[Me_3NCH_2CH_2OH]CdCl_3$–PDMS composite devices. (d) Capacitor charging experiments for optimal 15 wt % $[Me_3NCH_2CH_2OH]CdCl_3$–PDMS device with various capacitance of capacitors. (e) Schematic view of a full-wave bridge rectifier circuit diagram (top) and a photograph of the circuit utilized for the instant flash lighting of 35 LEDs (bottom). Reproduced with permission from ref. 146. Copyright © 2020 American Chemical Society.

Furthermore, piezoelectric composite films were prepared by mixing various weight percentages (5, 10, 15 and 20 wt %) of $[Me_3NCH_2CH_2OH]CdCl_3$ into a PDMS polymer. A simple PEH device was fabricated by placing $[Me_3NCH_2CH_2OH]CdCl_3$–PDMS composite between aluminium foil that was integrated on PET and an ITO-coated PET substrate, which acted as an upper and lower active electrode, respectively. A maximum output voltage and power density of 55.2 V and 70.9 μW cm^{-2}, respectively, were observed for the 15 wt % $[Me_3NCH_2CH_2OH]CdCl_3$–PDMS device, under an impact force of 40 N (Figure 34c). Furthermore, the optimal 15 wt % $[Me_3NCH_2CH_2OH]CdCl_3$–PDMS device was employed to charge various electrolytic capacitors and for flash lighting of LEDs by coupling it with a full-wave bridge rectifier circuit (Figure 34d and e).

Despite the advanced development in this field, several of these PEHs have limitations. For example, poor stability to both air and moisture, low levels of piezoelectric polarization, and most importantly, the need for toxic heavy metals, which further limits their use for medical and wearable electronic applications. One approach to tackle this problem is by introducing light-weight first-row transition metal ions combined with pseudo-halogenometallate counter-anions within the framework of organic-inorganic hybrid structures.

In 2020, Boomishankar and coworkers synthesized a ferroelectric 3d metal ion-containing A_4MX_6 type organic-inorganic hybrid compound $[Ph_3MeP]_4[Ni(NCS)_6]$, that crystallized in an acentric polar monoclinic space group *Cc* (Figure 35).[147] X-ray single-crystal diffraction analysis of $[Ph_3MeP]_4[Ni(NCS)_6]$ revealed an intriguing three-dimensional non-classical hydrogen-bonded structure (Figure 35a). These non-covalent interactions and their short

contacts were identified by performing Hirshfeld surface analysis. Furthermore, the polar nature of $[Ph_3MeP]_4[Ni(NCS)_6]$ was determined by performing ferroelectric measurements at room temperature, see Figure 35b. These results display excellent stable remnant polarization of P_r ~ 18.71 μC cm^{-2} and a low leakage current density value of 8.1 μA cm^{-2} (Figure 35b, blue peak).

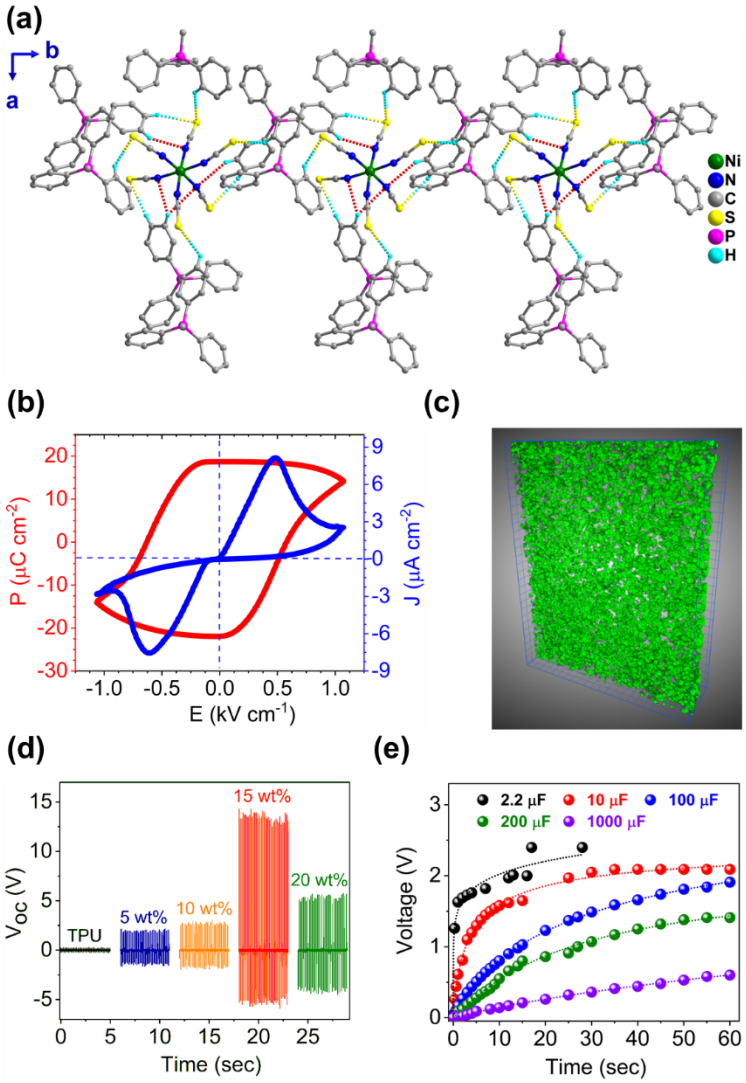

Figure 35. (a) Hydrogen-bonded structure of $[Ph_3MeP]_4[Ni(NCS)_6]$ along the b-axis facilitated via C-H···S and C-H···N interactions. (b) Ferroelectric hysteresis loop and leakage current-density plot on a single-crystal of $[Ph_3MeP]_4[Ni(NCS)_6]$. (c) X-ray 3D-microtomography image of the 15 wt % $[Ph_3MeP]_4[Ni(NCS)_6]$–TPU composite film (grid-scale: 100 μm). (d) Generated output voltage for all the wt % $[Ph_3MeP]_4[Ni(NCS)_6]$ –TPU hybrid composite devices. (e) Capacitor charging experiments for the selected best performing 15 wt % $[Ph_3MeP]_4[Ni(NCS)_6]$–TPU device. Reproduced with permission from ref. 147. Copyright © 2020, WILEY-VCH Verlag GmbH & Co. KGaA, Weinheim.

Due to the higher ferroelectric polarization of the $[Ph_3MeP]_4[Ni(NCS)_6]$ crystals, composite films with a range of weight percentages (5, 10, 15 and 20 wt %) were prepared with a non-piezoelectric thermoplastic polyurethane (TPU) polymer. Figure 35c shows a 3D-tomography image of a 15 wt % $[Ph_3MeP]_4[Ni(NCS)_6]$–TPU salt composite, which shows a uniform distribution of piezo- and ferro-electric crystallites within the composite film. Furthermore, the best performing 15 wt % $[Ph_3MeP]_4[Ni(NCS)_6]$–TPU device shows a high output voltage and power density of 19.29 V and 2.51 mW cm^{-3}, respectively (Figure 35d). The energy storage behavior of the 15 wt % $[Ph_3MeP]_4[Ni(NCS)_6]$–TPU composite device was evaluated by a capacitor charging experiment for a range of capacitance values (2.2, 10, 100, 200 and 1000 μF) (Figure 35e). The voltages accumulated in the capacitor were shown to attain threshold values within 60 seconds, indicating the effective energy storage capabilities of this device. Notably, the observed output performance of these composite devices is comparable, or even higher, than some of the best performing low molecular weight organic-inorganic hybrid-based piezoelectric energy harvesting systems.

Stimulated by the above work, ferroelectric A_2MX_4-type halogenometallate hybrid salts containing Cu(II) ions and heteroleptic phosphonium cations were explored by their group for piezoelectric energy harvesting (Figure 36).[148] These lead-free Cu(II) halides, $[Ph_3MeP]_2[CuCl_4]$ (**1**) and $[Ph_3MeP]_2[CuBr_4]$ (**2**) were synthesized as yellow and violet crystals from their respective copper and phosphonium halide precursors. Single-crystal X-ray diffraction analyses of hybrid Salt **1** and Salt **2** were described in polar orthorhombic space groups *Fdd2* and monoclinic *Cc*, respectively. Their molecular structure consists of $[PPh_3Me]^+$ cations and the isolated complex anions of $[CuCl_4]^{2-}$ and $[CuBr_4]^{2-}$, respectively (Figure 36a and b). The *P*-*E* hysteresis loops of Salt **1** and Salt **2** resulted in the P_r values of 17.16 and 26.02 μC cm^{-2} and the E_c of 1.67 and 2.00 kV cm^{-1}, respectively (Figure 36c and d). In addition, the temperature and frequency-dependent dielectric measurements of Salt **1** and Salt **2** show an absence of Curie points, which is rare in most well-known organic and organic-inorganic hybrid

ferroelectric materials. The direct piezoresponse of Salt **1** and Salt **2** (pellet samples) was recorded by a quasi-static method, leading to d_{33} values of d_{33} ~1.73 and d_{33} ~ 1.80 pC N^{-1} for Salt **1** and Salt **2**, at room temperature. Furthermore, composite piezoelectric harvesting devices based on Salt **1** were fabricated with a TPU matrix. The non-poled device of 15 wt % **1**-TPU showed a maximum voltage of 25 V, current density 1.0 μA cm^{-2} and the power density of 14.1 μW cm^{-2}, when measured at an optimized external load of 14.15 N and a frequency of 10 Hz (Figure 36e).

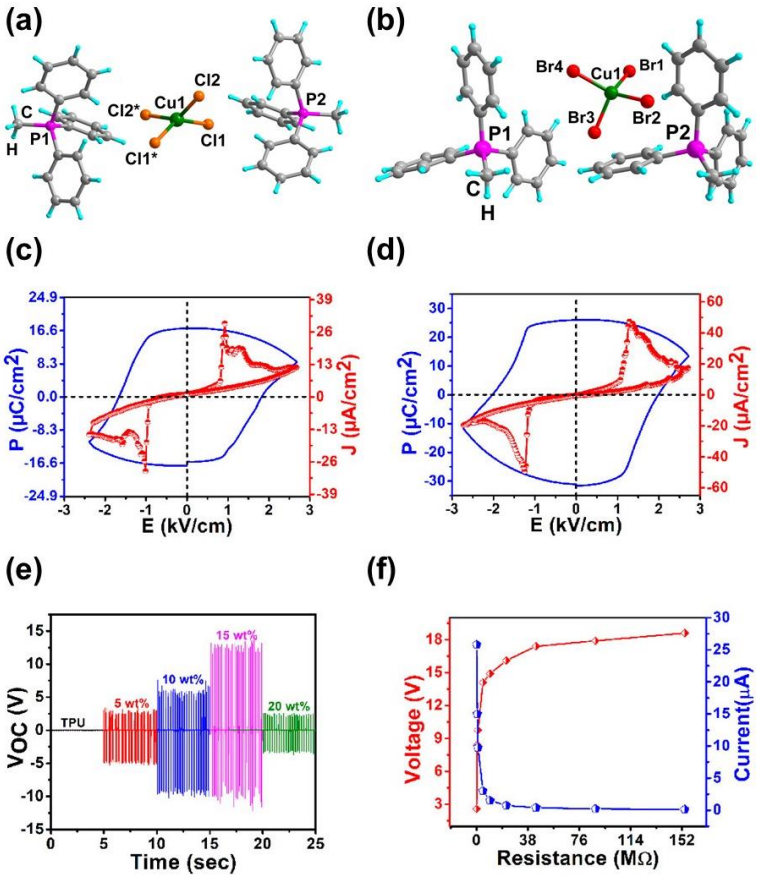

Figure 36. Molecular structures of (a) **1** and (b) **2**. Room temperature ferroelectric hysteresis loops and leakage current densities of (c) **1** and (d) **2**. (e) Piezoelectric output voltages of **1**-TPU composite devices. (f) Comparison of output voltage and calculated output current of the 15 wt % **1**-TPU composite devices function various load resistances. Reproduced with permission from ref. 148. Copyright © 2021 American Chemical Society.

Further, all the Salt **1**-TPU composite devices were tested under different external load resistances (0.1 to 157 MΩ). The detected output voltages and currents were shown to increase and decrease until the threshold level resistance of 157 MΩ, beyond which it saturates (Figure

36f). Furthermore, the best performing 15 wt% **1**-TPU offered excellent retention of piezoelectric voltages, even after three months (durability test), and cyclic stability over 10000 cycles. It is anticipated that the ease of fabrication, stability and piezoelectric performance of 3d metal-ion-based organic-inorganic hybrid PEHs could pave the way to create highly efficient piezoelectric nanogenerators for next-generation wearable electronics.

In this direction, recently, Bu and coworkers reported on a new hybrid organic-inorganic metal halide PEHs, $(BTMA)_2CoBr_4$ (BTMA = benzyltrimethylammonium) (Figure 37).[149] Single-crystal X-ray diffraction analysis of $(BTMA)_2CoBr_4$ showed that the molecule crystallized in a non-centrosymmetric space group $P2_1$ and adopted a discrete or zero-dimensional crystal packing structure (Figure 37a and b). The structural stabilization arise from the electrostatic interactions between organic $[BTMA]^+$ cation and the inorganic $[CoBr_4]^{2-}$ tetrahedron. These strong intermolecular interactions lead to the non-existence of any structural phase transition of $(BTMA)_2CoBr_4$ before its melting point. Moreover, DFT calculations of $(BTMA)_2CoBr_4$ showed the highest predicted elastic modulus, E_{max} and E_{min}, values of 17.56 and 4.11 GPa, respectively, along the <−101> and <101> directions. Such a difference in E could be realized in the arrangement of $[CoBr_4]^{2-}$ tetrahedron. In particular, the distance between the two nearest Co atoms are observed to be 8.898 and 12.071 Å along the <−101> direction, whereas these distances were found to be much higher (17.226 Å) along <101>, resulting in a lower Young's modulus in this direction. Furthermore, PFM analysis showed the existence of intrinsic piezo- and ferro-electric properties of $(BTMA)_2CoBr_4$. Figure 37c and d, shows the bias voltage-dependent phase hysteresis and amplitude butterfly curves, which confirms its polarization switching characteristics. PDMS composite films of $(BTMA)_2CoBr_4$ were prepared and evaluated for piezoelectric energy harvesting. The composite films were connected between two copper electrodes and encapsulated with PET tape, which formed a sandwich device architecture. Figure 37e and f, shows the presence of $(BTMA)_2CoBr_4$ particles in flexible PDMS composite films as observed from the scanning electron microscopy and mapping

images. Moreover, the 10 % $(BTMA)_2CoBr_4$/PDMS device exhibited the highest output open-circuit voltage and short-circuit current values of 19.70 V and 4.24 μA, respectively (Figure 37g). In addition, the device performance was performed with different external forces, which demonstrated the linear piezoresponse of the $(BTMA)_2CoBr_4$/PDMS device (Figure 37h). In addition, the $(BTMA)_2CoBr_4$/PDMS device was utilized to detect human motion (finger bending), demonstrating its potential for precise sensing of bio-mechanical movements.

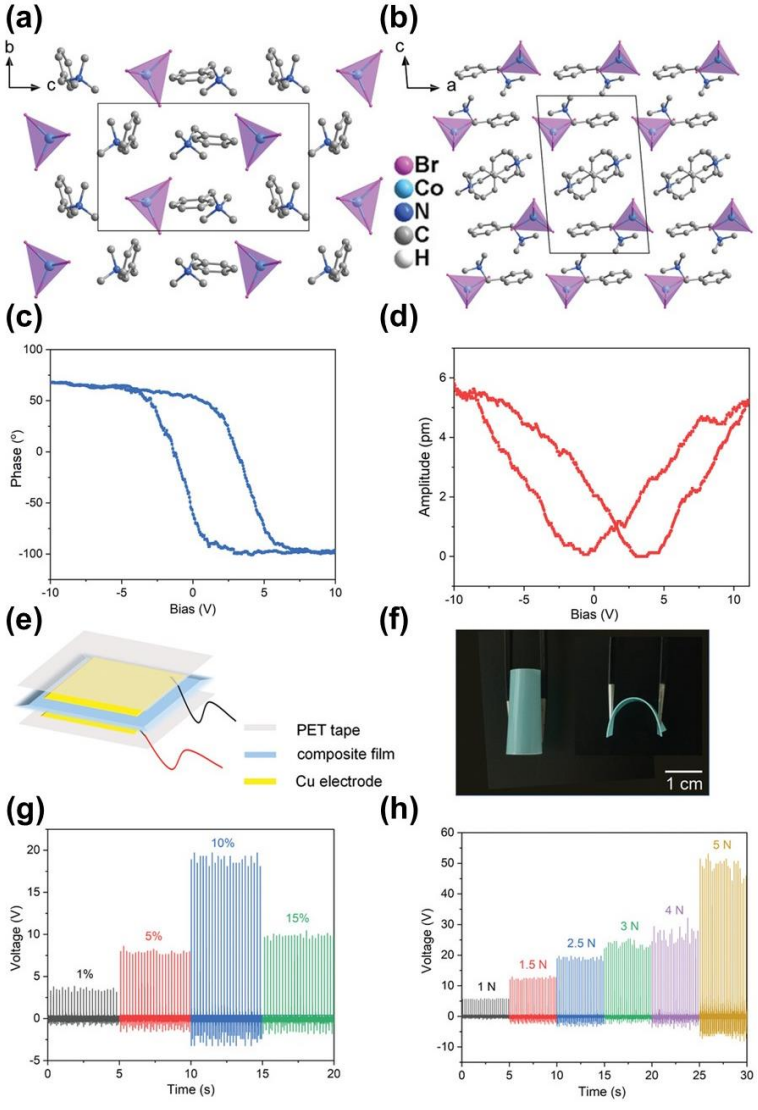

Figure 37. View of the crystal structure of $(BTMA)_2CoBr_4$ along the (a) a- and (b) b-axes, respectively. PFM measurements of thin-film sample of $(BTMA)_2CoBr_4$ (c) Phase–voltage hysteresis loop and (d) Amplitude–voltage butterfly curves with a direct current tip bias from −11 to 11 V. Schematic representation of (e) device fabrication process and (f) optical images. Piezoelectric energy harvesting performance of (g) output voltage of all the wt % composite $(BTMA)_2CoBr_4$/PDMS devices and (h) output voltage as a function of different load forces to 10 wt %

$(BTMA)_2CoBr_4$/PDMS device. Reproduced with permission from ref. 149. Copyright © 2021, WILEY-VCH Verlag GmbH & Co. KGaA, Weinheim.

Table 4 provides a summary of the output voltage, current and power of organic-inorganic hybrid composite energy harvesters in response to a mechanical input, where the voltage ranges from 0.22 V to 103 V and current from 4 nA to 35 μA.

Table 4. Summary of output performance of organic-inorganic hybrid composite energy harvesters discussed in section **6.**

Composite type	Voltage (Open circuit)	Current/current density	Power/power density	Application/Input	Area	Ref.
$FAPbBr_3$–PDMS	8.5 V	3.4 μA cm^{-2}	12 μW cm^{-2}	0.5 MPa	1 × 3 cm^2	121
$FAPbBr_3$ NPs@PVDF	30 V	6.2 μA cm^{-2}	27.4 μW cm^{-2}	0.5 MPa, 5 Hz	1.2 × 1.4 cm^2	122
$FAPbBr_2I$–PVDF	85 V	30 μA	10 μW cm^{-2}	1.35 N, 30 Hz	3.8 × 3.8 cm^2	123
$FAPbBr_3$/PVDF	26.2 V	2.1 μA	18.4 μW cm^{-2}	Finger tapping, 3 Hz	3 cm^2	124
$MAPbI_3$–PDMS	100 V	2.4 μA	0.3 mW cm^{-3}	Finger imparting	2.5 x 3.5 cm^2	125
$MAPbI_3$–PVDF (light-off)	33.6 V	3.54 μA cm^{-2}	-	300 kPa	1 x 1 cm^2	126
$MAPbI_3$–PVDF (light-on)	3.6 V	0.34 μA cm^{-2}	-	300 kPa	1 x 1 cm^2	126
$MAPbI_3$–PVDF	45.6 V	4.7 μA cm^{-2}	-	50 N, 5 Hz	1 x 1 cm^2	127
$MAPbBr_3$–PVDF	5 V	60 nA	0.28 μW cm^{-2}	9.8 kPa	2.4 x 1.5 cm^2	128
$MAPbI_3$–PVDF	1.8 V	37.5 nA	2.5 μW cm^{-2}	-	1 x 1 cm^2	129
$MAPbI_3$/PVDF	220 mV	4 nA	0.8 mW m^{-2}	7.5 N, 4 Hz	2.9 x 1.5 cm^2	130
$[(ATHP)_2PbBr_2Cl_2$@PDMS]	90 V	6.5 μA	1.7 μW cm^{-2}	4.2 N	-	131
$CsPbBr_3$– PVDF (PNG 5)	120 V	35 μA	4.24 mW	100 MPa	-	133
P(VDF−TrFE)/$CsPbBr_3$	2.4 V	0.17 μA	2.1 μW cm^{-2}	0.1 MPa	1 x 1 cm^2	134
P(VDF−TrFE)/$CsPbBr_3$	11.5 V	-	-	0.6 MPa	1 x 1 cm^2	134
$CsPbBr_3$@PVDF	103 V	170 μA cm^{-2}	14 μW cm^{-2}	10 m s^{-1}, 0.3 to 6 Hz	0.80 cm^2	135
$MASnI_3$–PVDF	12 V	4.0 μA cm^{-2}	21.6 μW cm^{-2}	0.5 MPa, 1 Hz	1 x 1 cm^2	138
$MASnBr_3$−PDMS (non-poled)	3.63 V	1.75 μA cm^{-2}	-	0.5 MPa, 5 Hz	3 x 3 cm^2	139
$MASnBr_3$−PDMS (poled)	18.8 V	13.76 μA cm^{-2}	74.52 μW cm^{-2}	0.5 MPa, 5 Hz	3 x 3 cm^2	139
$FASnI_3$:PVDF	23 V	6.15 μA cm^{-2}	35.05 mW cm^{-2}	0.1 MPa, 20 Hz	2 x 2 cm^2	143
$TMCM_2SnCl_6$@PDMS	81 V	2 μA	2.56 μW cm^{-2}	4.9 N, 40 Hz	-	144
$[BnNMe_3]_2CdBr_4$/PDMS	52.9 V	0.23 μA cm^{-2}	13.8 μW cm^{-2}	40 N, 25 Hz	3 x 3 cm^2	145
$[BnNMe_2{}^nPr]_2CdBr_4$/PDMS	63.8 V	0.59 μA cm^{-2}	37.1 μW cm^{-2}	40 N, 25 Hz	3 x 3 cm^2	145
$[Me_3NCH_2CH_2OH]CdCl_3$−PDMS	55.2 V	4.02 μAcm^{-2}	70.9 μW cm^{-2}	40 N, 25 Hz	2 x 2 cm^2	146
$[Ph_3MeP]_4[Ni(NCS)_6]$−TPU	19.29 V	3.59 μA cm^{-2}	2.51 mW cm^{-3}	17 N, 8 Hz	1.3 x 3 cm^2	147
$[Ph_3PMe]_4[CuCl_4]$	25 V	1.0 μA cm^{-2}	14.1 μW cm^{-2}	14.15 N, 10 Hz	360 mm^2	148

$(BTMA)_2CoBr_4$/PDMS	19.70 V	4.24 μA	11.72 μW cm^{-2}	2.5 N, 5 Hz	1.2 x 1.2 cm^2	149

7. Summary and Future Perspectives

This review discussed the key recent developments in the domain of organic and hybrid organic-inorganic materials and their composites for piezoelectric energy harvesting applications with a special emphasis on peptide and other biological and bio-inspired materials. In recent years, reports on organic and organic-inorganic energy harvesters have seen a steady growth, primarily due to their ease of fabrication by solution-phase synthesis, their low density and light-weight nature, their mechanical flexibility, high mechanical strength, and often non-toxic components, that are coupled with strong piezo- and ferroelectric properties. In the future, organic and organic-inorganic hybrid PEHs have significant potential in the field of molecular electronics, smart sensors, low-power portable electronics, wearable sensors and blue energy power systems. In addition, the development of such environmentally friendly piezoelectric energy and sensor materials are expected to facilitate their use in stretchable and bio-implanted skin applications. In this context, this review offers useful insights not only into the fabrication of device architectures for energy harvesting but also into the design of future organic and organic-inorganic hybrid systems and their crucial role in delivering enhanced performance. Nevertheless, we are at an early stage in the development of energy harvesting molecular systems, which require improvements in multiple aspects. Example areas include assessing and understanding device performance, long-term stability and durability (mechanical, thermal, environmental) and bio-compatibility and bio-degradability, in particular for medical and wearable applications. New directions for the development of such molecular energy harvesters may take into account, but are not limited to, the following considerations:

1. The majority of energy harvesting devices described herein are based on organic and organic-inorganic hybrid systems, and produce relatively small power output because of their relatively low piezoelectric coefficients. To enhance the output device

performance, fundamental understanding of piezoelectric materials, such as piezoelectric strain coefficient, ferroelectric hysteresis response, mechanical quality factor, and electromechanical response factor is necessary.

2. There is a potential to fabricate hybrid novel tribo-, piezo-, and thermo-electric energy harvesting devices comprised of one or more small molecules. The advantage of multiple energy harvesters lies not only in the enhancement of the output device performances but also in the simultaneous harvesting of energy types from a range of natural sources. This can lead to multi-functional systems.
3. Currently, most energy harvesters are based on the piezo- and tribo-electric effect. In contrast, pyroelectric energy harvesting and sensing (generation of electrical charges from a temperature fluctuation) properties of these organic and organic-inorganic energy harvesters are less well studied. The pyroelectric coefficients of organic and organic-inorganic hybrid compounds are less well understood compared to traditional ceramic materials. In the future, pyroelectric energy harvesters or sensors based on organic and hybrid organic-inorganic devices would be promising candidates to fulfil the energy requirements since thermal fluctuations are readily accessible.
4. Recently, new examples of transition-metal-based piezoelectric energy harvesters have led to improved power output due to the higher levels of ferroelectric polarization of these materials. Since the piezoelectric coefficient of materials is directly proportional to the ferroelectric polarization of the material, the development of materials with a higher ferroelectric polarization is expected to enhance device performance for these transition-metal-based harvesters.
5. Another essential factor influencing the output performance is the presence of interfacial polarization, in particular the interactions between the polymer matrix and the piezoelectric particles when used in composite form. Thus, exploring such composite

systems with a deeper understanding of interfacial chemistry in polymeric composite materials can improve output device performance.

6. Despite making significant strides in piezoelectric energy harvesting technologies, long-term stability and durability is an important issue for successful application of these new materials. The majority of organic and organic-inorganic hybrid perovskite materials are sensitive to oxygen, moisture, light, thermal fluctuations, electric fields, acids and bases, which lead to the degradation of these materials during service. In particular, a number of organic-inorganic hybrid compounds can easily decompose when exposed to oxygen and moisture due to the reactivity of the hygroscopic amine group and metal-halide bonds. Recent developments aimed at addressing these issues have focused on doping or element substitution, engineering the interface between the organic and organic-inorganic hybrid particles and the polymer matrices, or modification of A- or M- or X-site ions. The formation and stability of ABX_3-type perovskite structures are dictated by the Goldschmidt tolerance factor (t) as a common geometric guideline. Ideal perovskite compounds adopt a t value between 0.8 and 1.0, and a Goldschmidt tolerance factor of $t > 1$ or $t < 0.8$ results in non-perovskite systems that adopt diverse types of compositions such as A_2BX_4, A_3MX_6, and A_4BX_6 with different structures. Nevertheless, the first-principle calculations and experimental studies reveal the importance of ionization energy of organic-inorganic cations, encapsulation of active layer of perovskites, and the influence of valence band level on the formal structure and the stability of the organic-inorganic hybrid materials. In addition, the fabricated piezoelectric device must also exhibit long-term stability and durability for piezoelectric energy harvesting applications. Typically, the long-term stability of these devices is reduced over a period of time because of the lack of the regeneration of surface charge density between polymer matrix and piezoelectric particles. Future developments

should therefore explore the long-term stability and durability of these devices for real high-technology applications.[150-154]

7. Additional challenges in this area would be the biocompatibility and biodegradability of the molecular energy harvesters. In this regard, the existing limited reports[56,83,84,86,89-94] pertaining to amino acids and peptides are of great interest, but, more work is needed in terms of device performance, identifying the strong piezo- and ferro-electric materials, controlling the polarization directions and analyzing the accurate mechanism of piezo- and ferro-electric properties of these biomaterials.
8. While piezoelectric energy harvesting devices based on Pb(II), Sn(IV) and Cd(II) typically show the best device performance, these metals are toxic. In general, lead-based organic-inorganic piezoelectric energy harvesters have been explored due to their excellent electromechanical properties. However, toxic Pb(II) components lead to environmental issues, limiting their use in medical and wearable electronic-skin applications. Therefore, their replacement with less toxic and environmentally friendly materials is of interest. Indeed, in the search for new piezoelectric lead-free organic-inorganic hybrid energy harvesters, methylammonium tin iodide ($MASnI_3$) provides a range of advantages, such as reduced toxicity, decreased ecological damage, greater disposability and high piezoelectric coefficients (d_{33} ~ 100.9 pC N^{-1}). Despite these developments, a challenge is the long-term stability to both air and moisture and the presence of less toxic elements. One approaches to tackle this problem is the introduction of light-weight first-row transition metal ions, combined with pseudo-halogenometallate counter-anions within the framework of organic-inorganic hybrid structures. In particular, by employing first-row 3d metal-ion-based piezoelectric materials for mechanical energy harvesting applications. Such approaches have the potential to find a way to develop new high stability, heavy metal-free and non-toxic energy harvesters.

9. In addition, piezoelectric materials are excellent nonlinear-optical materials due to their lack of an inversion center. In the majority of these organic and organic-inorganic hybrid energy harvesting systems, a fundamental understanding of piezoelectric polarization is lacking. A thorough examination of several measurements and interpretations, including *P-E* hysteresis loop, SHG, PFM, electric field-dependent dielectric constant measurements and controlling the kinetics of piezo-electric domain orientation, would improve our understanding.
10. There is a significant potential for benefit in terms of materials design by computational modelling, ranging from density functional theory approaches to interfacial and composite modelling to facilitate our multi-scale understanding of these materials.
11. A series of high piezo- and ferro-electric organic and organic-inorganic hybrid materials are reported in the literature but are yet to be evaluated regarding their energy-harvesting behavior.[155-183] In the future, these materials can also be used to enhance the power generation competence of piezo-electric energy harvesting systems.
12. While materials are often evaluated for energy harvesting applications by charging storage capacitors and illuminating LEDs or LCD screens, there are fewer reports on complete harvesting systems based on organic and organic-inorganic hybrids. As a notable example of such potential, glycine crystals have recently been used as a piezoelectric sensor for structural health monitoring of pipe damage.[184]
13. Next-generation innovative microchip technology has seen robust attraction due to its multi-dimensional utilities in energy harvesting and flexible electronic applications. To date, the piezoelectrics used are low-dimensional (one to two-dimensional) materials, which hinders design of multiple-defined shapes such as discs, rods, rings, plates, tubes, cylinders, spheres and hemispheres. Recently, 3D-printed piezo-electric materials crossed this barrier and have been developed to convert mechanical movement, impact and stress from any direction into electrical energy.[185-190] This could be highly attractive

considering the high abundance of organic and organic-inorganic hybrid piezoelectric materials that are known today. The next step would be fabricating 3D-printed low-cost organic and organic-inorganic hybrid piezoelectric materials for flexible smart sensor devices for high-technology applications.

14. There is a need to provide performance data in a systematic fashion. At present, a direct comparison between piezoelectric energy harvesters can be hindered by data collected from different modes of operation, such as the applied mechanical force, frequency, layer thickness, device area, poled and unpoled device structure, structural morphologies and the weight ratio between polymer and piezoelectric filler. In order to provide valid benchmarking and comparison, consistency in data collection should be a consideration of future reports on piezoelectric harvesters.

We believe that this review will catalyse the development of piezoelectric energy harvesters based on molecular (organic and organic-inorganic hybrid) materials that will help to define the future of wearable electronics and biomedical devices.

Notes

The authors declare no competing financial interest.

Biographies

Thangavel Vijayakanth received an M.Sc. from the Bharathidasan University, India and a Ph.D. in Chemistry from the Indian Institute of Science Education and Research (IISER), Pune, India, in 2020 with Prof. Ramamoorthy Boomishankar. His Ph.D. dissertation was based on “Organo and amino phosphonium cation-derived ferro and piezoelectric materials and their utility in mechanical energy harvesting applications”. Then he joined Tel-Aviv University in 2021, Israel, for his post-doctoral studies and currently working with Prof. Ehud Gazit’s lab. His current research interests embrace bio-piezoelectric energy harvesting applications in wearable electronics, implantable electronics, piezo-robotics and self-powered sensors for the Internet of Things.

David Liptrot received his MChem (Hons) in Chemistry with Industrial Training from the University of Bath in 2011 and remained there to undertake a PhD on group 2 catalysis in the laboratory of Professor Mike Hill. After completing this in 2015 he took up a Lindemann Postdoctoral Fellowship with Professor Philip Power FRS (University of California, Davis, USA). In 2017 he returned to the University of Bath and in 2019 was awarded a Royal Society University Research Fellowship. His interests concern new synthetic methodologies to introduce main group elements into functional materials.

Ehud Gazit is a Professor and Endowed Chair at the Shmunis School of Biomedicine and Cancer Research, Faculty of Life Sciences and the Department of Materials Science and Engineering, Faculty of Engineering at Tel Aviv University. He received his BSc (summa cum laude) after completing his studies at the Special University Program for Outstanding Students at Tel Aviv University and his PhD (with highest distinction) from the Weizmann Institute of Science. He has been a faculty member at Tel Aviv University since 2000, following the completion of his postdoctoral studies at Massachusetts Institute of Technology (MIT). He was funded by ERC for the project of bio-inspired self-assembled supramolecular organic nanostructures in 2016. Prof. Gazit's research interests involve exploring the biological and bio-inspired molecular self-assembly, and using the minimalistic approach to define the smallest molecular recognition and assembly modules.

Ramamoorthy Boomishankar obtained his Ph.D. from the Indian Institute of Technology, Kanpur, India in the year 2004. He then took-up two postdoctoral stints at the University of Illinois Urbana-Champaign, USA and the University of Liverpool, UK. In April 2008, he joined the Indian Institute of Technology, Guwahati, India as an Assistant Professor in Chemistry. In December 2010, he moved to the Indian Institute of Science Education and Research (IISER) Pune, India where he is currently working as an Professor in the Department of Chemistry and Centre of Energy Sciences. The research focus of his group falls in the broad interface of

inorganic and materials chemistry with emphasis to synthesis, structure, physical properties and energy applications.

Christopher Rhys Bowen has a B.Sc. degree in Materials Science from the University of Bath (1986–1990) and a DPhil in Ceramics from the University of Oxford (1990–1993). Post-doctoral work has been undertaken at Technische Universität Harburg-Hamburg and University of Leeds (1994–1996). He was a Senior Scientist at the Defence Evaluation and Research Agency from 1996 to 1998. He joined the University of Bath as a Lecturer in 1998 and is now professor of Materials and former ERC Advanced Investigator. Research areas include energy harvesting, piezoelectric materials and functional ceramics.

Acknowledgments

T.V. thanks Tel Aviv University for the post-doctoral fellowship. R.B. thanks SERB, India, via Grant Nos. CRG/2019/004615 and EMR/2016/000614. E. G. thanks funding from ERC under the European Union Horizon 2020 Research, innovation program (grant agreement number BISON-694426). DJL thanks the Royal Society for a University Research Fellowship. We thank Dr. Sigal Rencus-Lazar for her help in scientific and language editing.

Conflict of Interest

The authors declare no conflict of interest.

Received: ((will be filled in by the editorial staff))
Revised: ((will be filled in by the editorial staff))
Published online: ((will be filled in by the editorial staff))

References

1) W. Zhang, R. G. Xiong, *Chem. Rev.* 2012, **112**, 1163.

2) E. S. Hosseini, S. Dervin, P. Ganguly, R. Dahiya. *ACS Appl. Bio Mater.* **2021,** 4, 163.

3) P. P. Shi, Y. Y. Tang, P.F. Li, W. Q. Liao, Z. X. Wang, Q. Ye, R. G. Xiong. *Chem. Soc. Rev.* **2016,** *45,* 3811.

4) C. A. P. De Araujo, J. D. Cuchiaro, D. L. Mc Millan, M. C. Scott, J. F. Scott. *Nature* **1995,** *374,* 627.

5) L. W. Martin, A. M. Rappe. *Nat. Rev. Mater.* **2016,** *2,* 16087.

6) Q. Dou, N. Wu, H. Yuan, K. H. Shin, Y. Tang, D. Mitlin, H. S. Park. *Chem. Soc. Rev.* **2021,** *50,* 6734.

7) M. Su, Y. Song. *Chem. Rev.* **2021,** doi.org/10.1021/acs.chemrev.1c00303.

8) W. P. Mason. *J. Acoust. Soc. Am.* **1981,** *70,* 1561.

9) S. Katzir. *Arch. Hist. Exact Sci.* **2003,** *57,* 61.

10) H. Y. Zhang, X. G. Chen, Y. Y. Tang, W. Q. Liao, F. F. Di, X. Mu, H. Peng, R. G. Xiong. *Chem. Soc. Rev.* **2021,** *50,* 8248.

11) A. S. Tayi, A. Kaeser, M. Matsumoto, T. Aida, S. I. Stupp. *Nature Chem.* **2015,** *7,* 281.

12) I. Bergenti. *J. Phys. D: Appl. Phys.* **2022,** *55,* 033001.

13) Q. Pan, Y. A. Xiong, T. T. Sha, Y. M. You. *Mater. Chem. Front.* **2021,** *5,* 44.

14) C. Paillard, X. Bai, I. C. Infante, M. Guennou, G. Geneste, M. Alexe, J. Kreisel, B. Dkhil. *Adv. Mater.* **2016,** *28,* 5153.

15) H. Yu, C. C. Chung, N. Shewmon, S. Ho, J. H. Carpenter, R. Larrabee, T. Sun, J. L. Jones, H. Ade, B. T. O'Connor, F. So. *Adv. Funct. Mater.* **2017,** *27,* 1700461.

16) S. Priya, D. J. Inman, *Energy Harvesting Technologies,* Springer, **2009**.

17) S. Chu, A. Majumdar. *Nature* **2012,** *488,* 294.

18) S. Chu, Y. Cui, N. Liu. *Nat. Mater.* **2017,** *16,* 16.

19) O. Ellabban, H. A. Rub, F. Blaabjerg. *Renewable Sustainable Energy Rev.* **2014,** *39,* 748.

20) P. Tao, G. Ni, C. Song, W. Shang, J. Wu, J. Zhu, G. Chen, T. Deng. *Nat. Energy* **2018,** *3*, 1031.

21) J. Chen, Y. Huang, N. Zhang, H. Zou, R. Liu, C. Tao, X. Fan, Z. L. Wang. *Nat. Energy* **2016**, *1*, 16138.

22) F. Invernizzi, S. Dulio, M. Petrini, G. Guizzetti, P. Mustarelli. *Chem. Soc. Rev.* **2016,** *45*, 5455.

23) Y. Tu, R. Wang, Y. Zhang, J. Wang. *Joule* **2018**, *2*, 1452.

24) H. Ryu, H. J. Yoon, S. W. Kim. *Adv. Mater.* **2019**, *31*, 1802898.

25) T. Cheng, Q. Gao, Z. L. Wang. *Adv. Mater. Technol.* **2019,** *4*, 1800588.

26) X. Huang, L. Wang, H. Wang, B. Zhang, X. Wang, R. Y. Z. Stening, X. Sheng, L. Yin. *Small* **2019**, 1902827.

27) Y. Zhang, P. Phuong, E. Roake, H. Khanbareh, Y. Wang, S. Dunn, C. Bowen. *Joule,* **2020,** *4*, 301.

28) C. R. Bowen, H. A. Kim, P. M. Weaver, S. Dunn. *Energy Environ. Sci.* **2014,** *7*, 25.

29) Z. L. Wang, J. Chen, L. Lin. *Energy Environ. Sci.* **2015**, *8*, 2250.

30) F. Hu, Q. Cai, F. Liao, M. Shao, S. T. Lee. *Small* **2015,** *11*, 5611.

31) Y. Zhang, M. Xie, V. Adamaki, H. Khanbareh, C. R. Bowen. *Chem. Soc. Rev.* **2017,** *46*, 7757.

32) B. Ates, S. Koytepe, A. Ulu, C. Gurses, V. K. Thakur. *Chem. Rev.*, **2020,** *120*, 9304.

33) R. Tian, Y. Liu, K. Koumoto, J. Chen. *Joule* **2019**, *3*, 1399.

34) P. Maharjan, H. Cho, M. S. Rasel, M. Salauddin, J. Y. Park. *Nano Energy* **2018**, *53*, 213.

35) C. Dagdeviren, P. Joe, O. L. Tuzman, K. Park, K. J. Lee, Y. Shi, Y. Huang, J. A. Rogers. *Extreme. Mech. Lett.* **2016,** *9*, 269–281.

36) M. E. Lines, A. M. Glass. Principles and Applications of Ferroelectrics and Related Materials; Oxford University Press: New York, **1977**.

37) J. F. Scott. *Science* **2007,** *315,* 954.

38) S. Y. Yang, J. Seidel, S. J. Byrnes, P. Shafer, C. H. Yang, M. D. Rossell, P. Yu, Y. H. Chu, J. F Scott, J. W. Ager, L. W. Martin, R. Ramesh. *Nat. Nanotechnol.* **2010,** *5,* 143.

39) H. Jin, J. Li, J. Iocozzia, X. Zeng, P. C. Wei, C. Yang, N. Li, Z. Liu, J. H. He, T. Zhu, J. Wang, Z. Lin, S. Wang. *Angew. Chem. Int. Ed.* **2019**, *58,* 15206.

40) V. Jella, S. Ippili, J. H. Eom, S. V. N. Pammi, J. S. Jung, V. D. Tran, V. H. Nguyen, A. Kirakosyan, S. Yun, D. Kim, M. R. Sihn, J. Choi, Y. J. Kim, H. J. Kim, S. G. Yoon. *Nano Energy* **2019**, *57,* 74.

41) J. Valasek. *Phys. Rev.* **1921**, *17,* 475.

42) G. Busch, P. Scherrer. *Naturwissenschaften* **1935**, *23,* 737.

43) Y. Y. Tang, P.F. Li, W. Q. Liao, P. P. Shi, Y. M. You, R. G. Xiong. *J. Am. Chem. Soc.* **2018,** *140,* 8051.

44) T. Hang, W. Zhang, H. Y. Ye, R. G. Xiong. *Chem. Soc. Rev.* **2011,** *40,* 3577.

45) H. A. Sodano, D. J. Inman, G. Park. *Shock Vib. Dig.* **2004,** *36,* 197.

46) S. R. Anton, H. A. Sodano. *Smart Mater. Struct.* **2007,** *16,* 1.

47) H. S. Kim, J. H. Kim, J. Kim. *Int. J. Precis. Eng. Manuf.* **2011,** *12,* 1129.

48) K. I. Park, C. K. Jeong, N. K. Kim, K. J. Lee. *Nano Convergence.* **2016,** *3,* 12.

49) Y. Bai, H. Jantunen, J. Juuti. *Adv. Mater.* **2018**, *30,* 1707271.

50) C. Wan, C. R. Bowen. *J. Mater. Chem. A* **2017,** *5,* 3091.

51) Y. Zhang, C. R. Bowen, S. K. Ghosh, D. Mandal, H. Khanbareh, M. Arafa, C. Wan. F. *Nano Energy* **2019,** *57,* 118.

52) J. Li, X. Wang. *APL Mater.* **2017,** *5,* 073801.

53) G. Chen, Y. Li, M. Bick, J. Chen. *Chem. Rev.* **2020,** *120,* 3668.

54) H. Y. Liu, H. Y. Zhang, X. G. Chen, R. G. Xiong. *J. Am. Chem. Soc.* **2020,** *142,* 15205.

55) K. Asadi, M. A. van der Veen. *Eur. J. Inorg. Chem.* **2016,** *27,* 4332.

56) D. Kim, S. A. Han, J. H. Kim, J. H. Lee, S. W. Kim, S. W. Lee. *Adv. Mater.* **2020,** *32,* 1906989.

57) R. Ding, M. C. Wong, J. Hao. *EcoMat.* **2020,** *2,* e12057.

58) H. Park, C. Ha, J. H. Lee. *J. Mater. Chem. A* **2020,** *8,* 24353.

59) Y. M. Mei, Q. F. Zeng, L. He, P. Yin, Y. Sun, W. Hu, R. Yang. *iScience* **2021,** *24,* 102274.

60) J. Harada. *APL Mater.* **2021,** *9,* 020901.

61) Z. L. Wang, J. Song. *Science* **2006,** *312,* 242.

62) Z. Yang, S. Zhou, J. Zu, I. Daniel. *Joule* **2018**, *2,* 642.

63) D. Hu, M. Yao, Y. Fan, C. Ma, M. Fan, M. Liu. *Nano Energy* **2019**, *55,* 288.

64) J. Li, X. Wang. *APL Mater.* **2017,** *5,* 073801.

65) W. Heywang, K. Lubitz, W. Wersing. *Piezoelectricity: Evolution and Future of a Technology,* Springer, **2008**.

66) F. Li, L. Jin, Z. Xu, S. Zhang. *Appl. Phys. Rev.* **2014,** *1*, 011103.

67) J. Briscoe, S. Dunn. *Nano Energy* **2015,** *14,* 15.

68) N. A. Shepelin, A. M. Glushenkov, V. C. Lussini, P.J. Fox, G. W. Dicinoski, J. G. Shapter, A. V. Ellis. *Energy Environ. Sci.* **2019**, *12,* 1143.

69) F. R. Fan, W. Tang, Z. L. Wang. *Adv. Mater.* **2016,** *28,* 4283.

70) M. Xie, K. Hisano, M. Zhu, T. Toyoshi, M. Pan, S. Okada, O. Tsutsumi, S. Kawamura, C. Bowen. *Adv. Mater. Technol.,* **2019,** *4,* 1800626.

71) P. Costa, J. Nunes-Pereira, N. Pereira, N. Castro, S. Gonçalves and S. Lanceros-Mendez. *Energy Technol.,* **2019,** *7,* 1800852.

72) A. Proto, M. Penhaker, S. Conforto and M. Schmid. *Trends Biotechnol.* **2017,** *35,* 610.

73) S. Horiuchi, Y. Tokura. *Nat. Mater.* **2008,** *7,* 357.

74) T. Shimizu, W. Ding, N. Kameta. *Chem. Rev.* **2020,** *120,* 2347.

75) S. I. Stupp, L. C. Palmer. *Chem. Mater.* **2014,** *26,* 507.

76) Y. Zhang, M. A. Hopkins, D. J. Liptrot, H. Khanbareh, P. Groen, X. Zhou, D. Zhang, Y. Bao, K. Zhou, C. R. Bowen and D. R. Carbery. *Angew. Chem., Int. Ed.* 2020, **59,** 7808.

77) S. Guerin, S. A. M. Tofail, D. Thompson. *NPG Asia Mater.* **2019,** *11,* 10.

78) J. O'Donnell, S. Guerin, P. Makam, P. A. Cazade, E. U. Haq, K. Tao, E. Gazit, C. Silien, T. Soulimane, D. Thompson, S. A. M. Tofail. *Appl. Mater. Today.* **2020,** *21,* 100818.

79) I. Chae, C. K. Jeong, Z. Ounaies, S. H. Kim. *ACS Appl. Bio Mater.* **2018,** *1,* 936.

80) P. K. Annamalai, A. K. Nanjundan, D. P. Dubal, J. B. Baek. *Adv. Mater. Technol.* **2021,** *6,* 2001164.

81) D. M. Shin, S. W. Hong, Y. H. Hwang. *Nanomaterials,* **2020,** *10,* 123.

82) K. Kapat, Q. T. H. Shubhra, M. Zhou, S. Leeuwenburgh. *Adv. Funct. Mater.* **2020,** *30,* 1909045.

83) S. Guerin, A. Stapleton, D. Chovan, R. Mouras, M. Gleeson, C. McKeown, M. R. Noor, C. Silien, F. M. F. Rhen, A. L. Kholkin, N. Liu, T. Soulimane, S. A. M. Tofail, D. Thompson. *Nat. Mater.* **2017,** *17,* 180.

84) W. Ji, B. Xue, Z. A. Arnon, H. Yuan, S. Bera, Q. Li, D. Zaguri, N. P. Reynolds, H. Li, Y. Chen, S. Gilead, S. Rencus-Lazar, J. Li, R. Yang, Y. Cao, E. Gazit. *ACS Nano* **2019,** *13,* 14477.

85) Z. Li, Y. Yin. *Adv. Mater.* **2019,** *31,* 1807061.

86) W. Ji, B. Xue, S. Bera, S. Guerin, Y. Liu, H. Yuan, Q. Li, C. Yuan, L. J. W. Shimon, Q. Ma, E. Kiely, S. A. M. Tofail, M. Si, X. Yan, Y. Cao, W. Wang, R. Yang, D. Thompson, J. Li, E. Gazit. *ACS Nano* **2020,** *14,* 10704.

87) A. Kholkin, N. Amdursky, I. Bdikin, E. Gazit, G. Rosenman. *ACS Nano* **2010,** *4,* 610.

88) K. Jenkins, S. Kelly, V. Nguyen, Y. Wu, R. Yang. *Nano Energy* **2018,** *51,* 317.

89) V. Nguyen, R. Zhu, K. Jenkins, R. Yang. *Nat. Commun.* **2016,** *7,* 13566.

90) J. H. Lee, K. Heo, K. S. Schonbagen, J. H. Lee, M. S. Desai, H. E. Jin, S. W. Lee. *ACS Nano* **2018,** *12,* 8138.

91) K. Tao, W. Hu, B. Xue, D. Chovan, N. Brown, L. J. W. Shimon, O. Maraba, Y. Cao, S. A. M. Tofail, D. Thompson, J. Li, R. Yang, E. Gazit, *Adv. Mater.* **2019,** *31,* 1807481.

92) K. Tao, B. Xue, Q. Li, W. Hu, L. J. W. Shimon, P. Makam, M. Si, X. Yan, M. Zhang, Y. Cao, R. S. Yang, J. B. Li, E. Gazit. *Mater. Today* **2019,** *30,* 10.

93) V. Basavalingappa, S. Bera, B. Xue, J. O'Donnell, S. Guerin, P. A. Cazade, H. Yuan, E. U. Haq, C. Silien, K. Tao, L. J. W. Shimon, S. A. M. Tofail, D. Thompson, S. Kolusheva, R. Yang, Y. Cao, E. Gazit. *ACS Nano* **2020,** *14,* 7025.

94) S. Bera, S. Guerin, H. Yuan, J. O. Donnell, N. P. Reynolds, O. Maraba, W. Ji, L. J. W. Shimon, P. A. Cazade, S. A. M. Tofail, D. Thompson, R. Yang, E. Gazit. *Nat. Commun.* **2021,** *12,* 2634.

95) W. Ma, Y. Zhang, S. Pan, Y. Cheng, Z. Shao, H. Xiang, G. Chen, L. Zhu, W. Weng, H. Bai, M. Zhu. *Chem. Soc. Rev.* **2021,** *50,* 7009.

96) T. Vijayakanth, A. K. Srivastava, F. Ram, P. Kulkarni, K. Shanmuganathan, B. Praveenkumar, R. Boomishankar. *Angew. Chem. Int. Ed.* **2018,** *57,* 9054.

97) T. Vijayakanth, F. Ram, B. Praveenkumar, K. Shanmuganathan, R. Boomishankar. *Chem. Mater.* **2019,** *31,* 5964.

98) R. Gupta, S. Sahoo, S. Deswal, P. Kothavade, P. Dixit, J. K. Zaręba, K. Shanmuganathan, R. Boomishankar. *Chem Asian J.* **2021,** doi.org/10.1002/asia.202101128.

99) C. R. Bernardo, R. M. F. Baptista, E. M. Gomes, P. E. Lopes, M. M. M. Raposo, S. P. G. Costa, M. S. Belsley. *Nanoscale Adv.* **2020,** *2,* 1206.

100) R. M. F. Baptista, E. de Matos Gomes, M. M. M. Raposo, S. P. G. Costa, P. E. Lopes, B. Almeida, M. S. Belsley. *Nanoscale Adv.* **2019,** *1,* 4339.

101) K. Liu, Y. Jiang, Y. Jiang, Y. Guo, Y. Liu, E. Nakamura. *J. Am. Chem. Soc.* **2019,** *141,* 1406.

102) A. K. Jena, A. Kulkarni, T. Miyasaka. *Chem. Rev.* **2019,** *119,* 3036.

103) M. Faustini, L. Nicole, E. Ruiz-Hitzky, C. Sanchez. *Adv. Funct. Mater.* **2018,** *28,* 1704158.

104) W. J. Hu, S. Kopyl, A. Kholkin, J. Rocha. *Coord. Chem. Rev.* **2019,** *387,* 398.

105) J. S. Manser, J. A. Christians, P. V. Kamat. *Chem. Rev.* **2016,** *116,* 12956.

106) S. D. Stranks, H. J. Snaith. *Nat. Nanotechnol.* **2015,** *10,* 391.

107) Y. Fu, H. Zhu, J. Chen, M. P. Hautzinger, X. Y. Zhu, S. Jin. *Nat. Rev. Mater.* **2019,** *4,* 169.

108) P. Schulz, D. Cahen, A. Kahn. *Chem. Rev.* **2019,** *119,* 3349.

109) B. R. Sutherland, E. H. Sargent. *Nat. Photonics* **2016,** *10,* 295.

110) F. Narita, M. Fox. *Adv. Eng. Mater.* **2018,** *20,* 1700743.

111) N. Wang, W. Liu, Q. Zhang. *Small Methods.* **2018,** *2,* 1700380.

112) M. Coll, A. Gomez, E. Mas-Marza, O. Almora, G. Garcia Belmonte, M. Campoy-Quiles, J. Bisquert. *J. Phys. Chem. Lett.* **2015,** *6,* 1408.

113) Y. J. Kim, T. V. Dang, H. J. Choi, B. J. Park, J. H. Eom, H. A. Song, D. Seol, Y. Kim, S. H. Shin, J. Nah, S. G. Yoon. *J. Mater. Chem. A* **2016,** *4,* 756.

114) S. Ippili, V. Jella, J. Kim, S. Hong, S. G. Yoon. *Nano Energy,* **2018,** *49,* 247.

115) R. Tusiime, F. Zabihi, M. Tebyetekerwa, Y. M. Yousry, Y. Wu, M. Eslamian, S. Yang, S. Ramakrishna, M. Yu, H. Zhang. *J. Mater. Chem. C* **2020,** *8,* 2643.

116) V. Jella, S. Ippili, S. G. Yoon. *ACS Appl. Electron. Mater.* **2020,** *2,* 2579.

117) Z. X. Zhang, H. Y. Zhang, W. Zhang, X. G. Chen, H. Wang, R. G. Xiong. *J. Am. Chem. Soc.* **2020,** *142,* 17787.

118) Y. Zhang, X. J. Song, Z. X. Zhang, D. W. Fu, R. G. Xiong, *Matter* **2020,** *2,* 697.

119) L. He, Y. Liu, P. Shi, H. Cai, D. Fu, Q. Ye. *ACS Appl. Mater. Interfaces* **2020,** *12,* 53799.

120) D. B. Kim, K. H. Park, Y. S. Cho. *Energy Environ. Sci.* **2020,** *13,* 2077.

121) R. Ding, H. Liu, X. Zhang, J. Xiao, R. Kishor, H. Sun, B. Zhu, G. Chen, F. Gao, X. Feng, J. Chen, X. Chen, X. Sun, Y. Zheng. *Adv. Funct. Mater.* **2016,** *26,* 7708.

122) R. Ding, X. Zhang, G. Chen, H. Wang, R. Kishor, J. Xiao, F. Gao, K. Zeng, X. Chen, X.W. Sun, Y. Zheng. *Nano Energy,* **2017,** *37,* 126.

123) A. A. Khan, M. M. Rana, G. Huang, N. Mei, R. Saritas, B. Wen, S. Zhang, P. Voss, E. A. Rahman, Z. Leonenko, S. Islam, D. Ban. *J. Mater. Chem. A* **2020,** *8,* 13619.

124) S. K. Si, S. Paria, S. K. Karan, S. Ojha, A. K. Das, A. Maitra, A. Bera, L. Halder, A. De, B. B. Khatua. *Nanoscale,* **2020,** *12,* 7214.

125) J. Dhar, S. Sil, N. A. Hoque, A. Dey, S. Das, P. P. Ray, D. Sanyal. *ChemistrySelect,* **2018,** *3,* 5304.

126) S. Ippili, V. Jella, S. Eom, S. Hong, S. G. Yoon. *ACS Appl. Mater. Interfaces.* **2020,** *12,* 50472.

127) V. Jella, S. Ippili, J. H. Eom, J. Choi, S. G. Yoon. *Nano Energy,* **2018,** *53,* 46.

128) A. Sultana, M. M. Alam, P. Sadhukhan, U. K. Ghorai, S. Das, T. R. Middya, D. Mandal. *Nano Energy* **2018,** *49,* 380.

129) A. Sultana, P. Sadhukhan, M. M. Alam, S. Das, T. R. Middya, D. Mandal. *ACS Appl. Mater. Interfaces* **2018,** *10,* 4121.

130) A. Sultana, S. K. Ghosh, M. M. Alam, P. Sadhukhan, K. Roy, M. Xie, C. R. Bowen, S. Sarkar, S. Das, T. R. Middya, D. Mandal, D. *ACS Appl. Mater. Interfaces* **2019,** *11,* 27279.

131) A. A. Khan, G. Huang, M. M Rana, N. Mei, M. Biondi, S. Rassel, N. Tanguy, B. Sun, Z. Leonenko, N. Yan, C. Wang, S. Xu, D. Ban. *Nano Energy* **2021,** *86,* 106039.

132) Y. Q. Zhao, Q. R. Ma, B. Liu, Z. L. Yu, M. Q. Cai. *Phys. Chem. Chem. Phys.* **2018,** *20,* 14718.

133) S. Mondal, T. Paul, S. Maiti, B. K. Das, K. K. Chattopadhyay. *Nano Energy* **2020,** *74,* 104870.

134) J. Nie, L. Zhu, W. Zhai, A. Berbille, L. Li, Z. L. Wang. *ACS Appl. Electron. Mater.* **2021,** *3,* 2136.

135) H. Chen, L. Zhou, Z. Fang, S. Wang, T. Yang, L. Zhu, X. Hou, H. Wang, Z. L. Wang. *Adv. Funct. Mater.* **2021,** *31,* 2011073.

136) R. Ding, X. Zhang, X. W. Sun. *Adv. Funct. Mater.* **2017,** *27,* 1702207.

137) S. Liu, F. Zheng, I. Grinberg, A. M. Rappe. *J. Phys. Chem. Lett.* **2016,** *7,* 1460.

138) S. Ippili, V. Jella, J. H. Eom, J. Kim, S. Hong, J. S. Choi, V. D. Tran, N. Van Hieu, Y. J. Kim, H. J. Kim, S. G. Yoon. *Nano Energy* **2019,** *57,* 911.

139) S. Ippili, V. Jella, J. Kim, S. Hong, S. G. Yoon. *ACS Appl. Mater. Interfaces.* **2020,** *12,* 16469.

140) A. Amat, E. Mosconi, E. Ronca, C. Quarti, P. Umari, Md. K. Nazeeruddin, M. Gratzel, F. D. Angelis. *Nano Lett.* **2014,** *14,* 3608.

141) H. Dong, C. Zhang, X. Liu, J. Yao, Y. S. Zhao. *Chem. Soc. Rev.* **2020,** *49,* 951.

142) Y. Fu, H. Zhu, A. W. Schrader, D. Liang, Q. Ding, P. Joshi, L. Hwang, X. Y. Zhu and S. Jin. *Nano Lett.* **2016,** *16,* 1000.

143) R. Pandey, S. B. Gangadhar, S. Grover, S. K. Singh, A. Kadam, S. Ogale, U. V. Waghmare, V. R. Rao, D. Kabra. *ACS Energy Lett.* **2019,** *4,* 1004.

144) G. Huang, A. A. Khan, M. M. Rana, C. Xu, S. Xu, R. Saritas, S. Zhang, E. A. Rahmand, P. Turban, S. A. Girard, C. Wang, D. Ban. *ACS Energy Lett.* **2021,** *6,* 16.

145) S. Deswal, S. K. Singh, P. Rambabu, P. Kulkarni, G. Vaitheeswaran, B. Praveenkumar, S. Ogale, R. Boomishankar. *Chem. Mater.* **2019,** *31,* 4545.

146) S. Deswal, S. K. Singh, R. Pandey, P. Nasa, D. Kabra, B. Praveenkumar, S. Ogale, R. Boomishankar. *Chem. Mater.* **2020,** *32,* 8333.

147) T. Vijayakanth, F. Ram, B. Praveenkumar, K. Shanmuganathan, R. Boomishankar. *Angew. Chem. Int. Ed.* **2020,** *59,* 10368.

148) S. Sahoo, T. Vijayakanth, P. Kothavade, P. Dixit, J. K. Zaręba, K. Shanmuganathan, R. Boomishankar. *ACS Mater. Au.* **2021.** doi:10.1021/acsmaterialsau.1c00046.

149) T. M. Guo, Y. J. Gong, Z. G. Li, Y. M. Liu, W. Li, Z. Y. Li, X. H. Bu. *Small* **2021**, 2103829.

150) X. Li, J. M. Hoffman, M. G. Kanatzidis. *Chem. Rev.* **2021,** *121,* 2230.

151) B. Saparov, D. B. Mitzi. *Chem. Rev.* **2016,** *116,* 4558.

152) J. Y. Kim, J. W. Lee, H. S. Jung, H. Shin, N. G. Park. *Chem. Rev.* **2020*, 120,*** 7867.

153) J. Burschka, N. Pellet, S. J. Moon, R. H. Baker, P. Gao, M. K. Nazeeruddin, M. Grätzel, *Nature*. **2013**, *499*, 316.

154) L. Ma, R. Wu, A. Patil, J. Yi, D. Liu, X. Fan, F. Sheng, Y. Zhang, S. Liu, S. Shen, J. Wang, Z. L. Wang. *Adv. Funct. Mater.* **2021**, *31,* 2102963.

155) Y. M. You, W. Q. Liao, D. Zhao, H. Y. Ye, Y. Zhang, Q. Zhou, X. Niu, J. Wang, P. F. Li, D. W. Fu, Z. Wang, S. Gao, K. Yang, J. M. Liu, J. Li, Y. Yan, R. G. Xiong. *Science.* **2017,** *357,* 306.

156) W. Q. Liao, Y. Y. Tang, P. F. Li, Y. M. You, R. G. Xiong. *J. Am. Chem. Soc.* **2017,** *139,* 18071.

157) J. Harada, N. Yoneyama, S. Yokokura, Y. Takahashi, A. Miura, N. Kitamura, T. Inabe. *J. Am. Chem. Soc.* **2018,** *140,* 346.

158) D. Li, X. M. Zhao, H. X. Zhao, X. W. Dong, L. S. Long, L. S. Zheng. *Adv. Mater.* **2018,** *30,* 1803716.

159) W. Q. Liao, Y. Y. Tang, P. F. Li, Y. M. You, R. G. Xiong. *J. Am. Chem. Soc.* **2018,** *140,* 3975.

160) J. Harada, Y. Kawamura, Y. Takahashi, Y. Uemura, T. Hasegawa, H. Taniguchi, K. Maruyama. *J. Am. Chem. Soc.* **2019,** *141,* 9349.

161) D. Zhao, Y. Y. Tang, Y. Zhang, P. F. Li, P. P. Shi, X. G. Chen, Y. M. You, R. G. Xiong. *Science* **2019**, *363*, 1206.

162) Z. X. Wang, H. Zhang, F. Wang, H. Cheng, W. H. He, Y. H. Liu, X. Q. Huang, P. F. Li. *J. Am. Chem. Soc.* **2020,** *142*, 12857.

163) C. Shi, J. J. Ma, J. Y. Jiang, M. M. Hua, Q. Xu, H. Yu, Y. Zhang, H. Y. Ye. *J. Am. Chem. Soc.* **2020,** *142*, 9634.

164) Q. Pan, Y. A. Xiong, T. T. Sha, Y. M. You. *Mater. Chem. Front.* **2021,** *5*, 44.

165) Y. Hu, L. You, B. Xu, T. Li, S. A. Morris, Y. Li, Y. Zhang, X. Wang, P. S. Lee, H. J. Fan, J. Wang. *Nat. Mater.* **2021,** *20,* 612.

166) C. R. Huang, Y. Li, Y. Xie, Y. Du, H. Peng, Y. L. Zeng, J. C. Liu, R. G. Xiong. *Angew. Chem. Int. Ed.* **2021,** DOI: 10.1002/anie.202105744.

167) Y. Ai, Y. L. Zeng, W. H. He, X. Q. Huang, Y. Y. Tang. *J. Am. Chem. Soc.* **2020,** *142,* 13989.

168) S. Furukawa, J. Wu, M. Koyama, K. Hayashi, N. Hoshino, T. Takeda, Y. Suzuki, J. Kawamata, M. Saito, T. Akutagawa. *Nat. Commun.* **2021,** *12*, 768.

169) W. Q. Liao, B. B. Deng, Z. X. Wang, T. T. Cheng, Y. T. Hu, S. P. Cheng, R. G. Xiong, *Adv. Sci.* **2021**, 2102614.

170) W. Li, G. Tang, G. Zhang, H. M. Jafri, J. Zhou, D. Liu, Y. Liu, J. Wang, K. Jin, Y. Hu, H. Gu, Z. Wang, J. Hong, H. Huang, L. Q. Chen, S. Jiang, Q. Wang. *Sci. Adv.* **2021**, *7*, eabe3068.

171) X. J. Song, T. Zhang, Z. X. Gu, Z. X. Zhang, D. W. Fu, X. G. Chen, H. Y. Zhang, R. G. Xiong. *J. Am. Chem. Soc.* **2021,** *143*, 5091.

172) T. Akutagawa, T. Takeda, N. Hoshino. *Chem. Commun.* **2021,** *57*, 8378.

173) P. Szklarz, V. Kinzhybalo, G. Bator. *CrystEngComm.* **2021,** *23*, 4005.

174) Y. Hu, L. You, B. Xu, T. Li, S. A. Morris, Y. Li, Y. Zhang, X. Wang, P. S. Lee, H. J. Fan, J. Wang. *Nat. Mater.* **2021,** *20*, 612.

175) W. J. Xu, K. Romanyuk, J. M. G. Martinho, Y. Zeng, X. W. Zhang, A. Ushakov, V. Shur, W. X. Zhang, X. M. Chen, A. Kholkin, Joao Rocha. *J. Am. Chem. Soc.* **2020,** *142*, 16990.

176) Y. Y. Tang, Y. Xie, Y. L. Zeng, J. C. Liu, W. H. He, X. Q. Huang, R. G. Xiong. *Adv. Mater.* **2020**, *32*, 2003530.

177) H. Y. Zhang, Z. X. Zhang, X. G. Chen, X. J. Song, Y. Zhang, R. G. Xiong. *J. Am. Chem. Soc.* **2021,** *143*, 1664.

178) M. Rok, B. Zarychta, A. Bil, J. T. Piegza, W. Medycki, A. Miniewicz, A. P. Bisiorek, A. Cizman, R. Jakubas. *J. Mater. Chem. C*, **2021,** *9*, 7665.

179) Y. K. Li, Y. Y. Lai, T. T. Ying, D. C. Han, Y. H. Tan, Y. Z. Tang, P. K. Du, H. Zhang. *Chem. Sci.*, **2021,** *12*, 13061.

180) X. Liu, Z. Wu, T. Guan, H. Jiang, P. Long, X. Li, C. Ji, S. Chen, Z. Sun, J. Luo. *Nat. Commun.* **2021,** *12*, 5502.

181) Y. Ai, R. Sun, Y. L. Zeng, J. C. Liu, Y. Y. Tang, B. W. Wang, Z. M. Wang, S. Gao, R. G. Xiong. *Chem. Sci.* **2021,** *12*, 9742.

182) J. C. Liu, W. Q. Liao, P. F. Li, Y. Y. Tang, X. G. Chen, X. J. Song, H. Y. Zhang, Y. Zhang, Y. M. You, R. G. Xiong. *Angew. Chem. Int. Ed.* **2020,** *59*, 3495.

183) X. G. Chen, X. J. Song, Z. X. Zhang, P. F. Li, J. Z. Ge, Y. Y. Tang, J. X. Gao, W. Y. Zhang, D. W. Fu, Y. M. You, R. G. Xiong. *J. Am. Chem. Soc.* **2020,** *142*, 1077.

184) F. Okosun, S. Guerin, M. Celikin, V. Pakrashi. *Cell Rep. Phys. Sci.* **2021,** *2,* 100434.

185) H. Cui, R. Hensleigh, D. Yao, D. Maurya, P. Kumar, M. G. Kang, S. Priya, X. R. Zheng. *Nat. Mater.* **2019,** *18,* 234.

186) C. Chen, X. Wang, Y. Wang, D. Yang, F. Yao, W. Zhang, B. Wang, G. A. Sewvandi, D. Yang, D. Hu, *Adv. Funct. Mater.* **2020,** *30,* 2005141.

187) Y. Hu, Z. Guo, A. Ragonese, T. Zhu, S. Khuje, C. Li, J. C. Grossman, C. Zhou, M. Nouh, S. Ren. *PNAS,* **2020,** *117,* 27204.

188) X. Gao, J. Yang, J. Wu, X. Xin, Z. Li, X. Yuan, X. Shen, S. Dong. *Adv. Mater. Technol.* **2020,** *5,* 1900716.

189) X. Zhou, P. S. Lee. *Eco. Mat.* **2021,** DOI: 10.1002/eom2.12098.

190) W. Wang, J. Li, H. Liu, S. Ge. *Adv. Sci.* **2021,** *8,* 2003074.

Piezo and Ferroelectric Energy Harvesters: The review overviews piezoelectric and ferroelectric materials based on organic molecules and organic-inorganic hybrids for energy harvesting applications. These materials exhibit advantages of simple synthesis in solution-phase, light-weight nature, thermal stability, mechanical flexibility, high Curie temperature and high polarization that offers excellent platform for them to serve as efficient generators. These aspects are discussed in detail, and future directions indicated.

Keyword piezoelectricity, ferroelectricity, energy harvesting, organic composites, organic-inorganic hybrids, flexible electronics

Thangavel Vijayakanth,* David J. Liptrot,* Ehud Gazit,* Ramamoorthy Boomishankar,* and Chris R. Bowen*

Title Recent Advances in Organic and Organic-Inorganic Hybrid Materials for Piezoelectric Mechanical Energy Harvesting